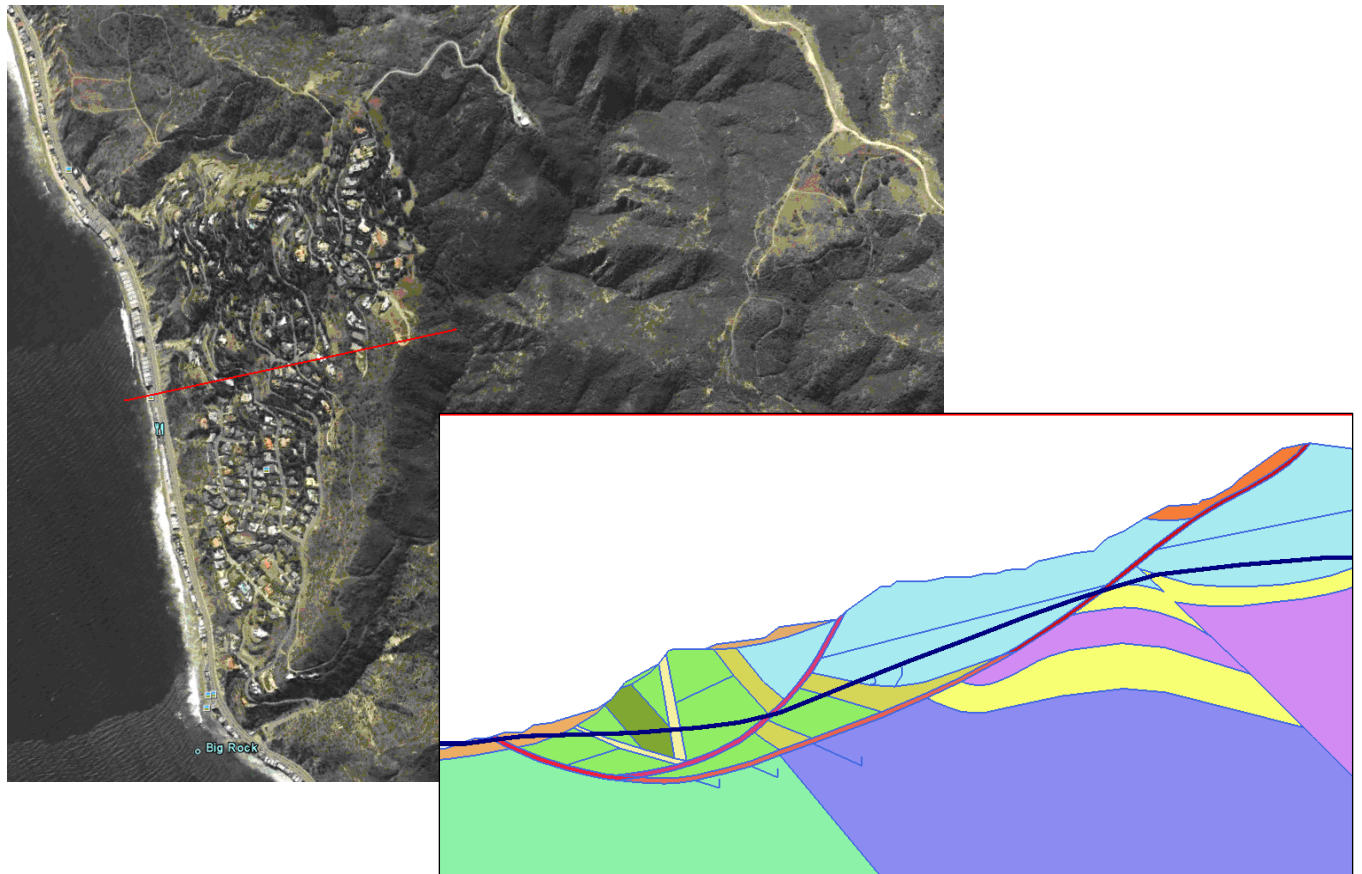



Process and stability of slow moving landslides



Eva Johanna Sloof

Copyright © E.J. Sloof
All rights reserved

Master Thesis	<i>Process and stability of slow moving landslides</i>	
	<i>June 2010</i>	
Author	<i>E.J. Sloof</i>	1328514
Master	<i>Geo-mechanics</i>	
Members graduation comity:		
Prof.dr. M.A. Hicks		
Prof.dr.ir. F. Molenkamp		
Dr.ir. R.B.J. Brinkgreve		
Dr.ir. N. Kringos		

Abstract

The stability of the slow moving Big Rock Mesa (BRM) landslide located in California (USA) was analysed. A detailed description of its geometry and soil structure is presented. For the stability vital shear zone and unsaturated zone were identified. The strength and permeability of the different layers that exist in the BRM were determined using computational methods and from literature data.

The stability of landslides is susceptible to rainfall and changes to the groundwater level. The corresponding pressure changes cause slopes to become unstable. In dry periods the landslide is stable and in wet periods displacements by deformations occur. For the BRM landslide the rainfall data and displacements recorded with inclinometers were analysed. A water balance was made for a critical and stable period to evaluate the hydraulic flow. Besides rainwater it is likely that also water from adjacent areas flows into the BRM mass. Most of the rainwater is stored in the unsaturated zone of the BRM, which has an average thickness of about 42.5 m. Only a part of this water disappears by run-off and dewatering. The water pulse in the unsaturated zone is slowly drained by the evapotranspiration. The groundwater level profile of BRM was determined from measurements and computed with a statistical program called Surfer.

The infiltration of water into the unsaturated zone reduces the suction. This suction is smallest over the vertical infiltration length of the water pulse. The water pulse propagates deeper into the unsaturated zone when rainfall increases. The reduction suction weakens the soil. Consequently, the stability of a slide increases with evapotranspiration and decreases with water infiltration.

The stability of the BRM and the flow through the unsaturated zone was analysed with the finite element program Plaxis. However, due to the size of the BRM a full coupled analysis of deformations and hydraulic flow was not possible. Instead steady state calculations were performed. The flow through the unsaturated zone was compared with results from the one-dimensional flow program called SWAP. For the conditions of steady state calculation with suction the BRM is stable with a safety factor of 1.17. The safety factor of the BRM decreases slightly with increasing head on the hill side of the geometry. Suction in the unsaturated zone increases the safety factor by only 0.01. This suction decreases when water infiltrates. The calculated small influence of increasing groundwater table corresponds with inclinometer readings.

Index

1. Introduction	11
2. Slow moving landslides	12
2.1. General aspects of landslides	13
2.1.1. Phenomena affecting the stability of landslides	13
2.1.2. Shear zone	15
2.2. Movement of landslides caused by, rainfall, evapotranspiration and earthquakes	18
2.2.1. Landslide movement caused by rainfall	18
2.2.2. Influence of evapotranspiration on landslide movement	22
2.2.3. Earthquake caused landslides	24
2.3. Monitoring of landslides	29
2.4. Dewatering systems	32
3. Data evaluation Big Rock Mesa Landslide	35
3.1. Geological evaluation	36
3.1.1. General aspects	36
3.1.2. Rock formations	37
3.1.3. Ancient movement of the BRM landslide	39
3.1.4. Current movement of the BRM landslide	41
3.2. Hydraulics	44
3.2.1. Rainfall data	44
3.2.2. Groundwater levels	47
3.2.3. Dewatering	47
3.3. Earthquake	49
4. Unsaturated soil behaviour	51
4.1. Defining the unsaturated zone	52
4.1.1. water content	52
4.2. Soil suction	56
4.2.1. calculation method for soil suction	58
4.2.2. Matric suction profile	59
4.2.3. Interparticle forces	60
4.3. Wetting and drying cycles	61
4.3.1. Drying cycle (air intake)	61
4.3.2. Wetting cycle	62
4.4. Effect of suction on deformation	63
4.5. Unsaturated zone in rocks	68

5. Finite Element (FE) Modelling	70
5.1. Material models	71
5.1.1. Mohr Coulomb (MC)	71
5.1.2. Barcelona Basic (BB)I	75
5.2. Constitutive relations	80
5.2.1. Flow	80
5.2.2. Deformation	82
5.3. Finite Element modelling	84
5.3.1. Coupled analysis	84
5.4. Unsaturated zone mechanics	86
6. Motivation of parameters used in modelling of the BRM slide	88
6.1. Suppositions for modelling	89
6.2. Selection of the period for modelling	90
6.3. Selection of the cross-section	91
6.4. Hydraulic system	94
6.4.1. Groundwater surface	94
6.4.2. Upper and lower boundary groundwater level	96
6.4.3. Water balance reference period	98
6.4.4. Water balance analyses period	100
6.5. Soil/Rock properties	106
6.5.1. Permeability	106
6.5.2. Strength	113
6.5.3. Model geometry	122
7. Sensitivity study	123
7.1. Water flow through the unsaturated zone	124
7.1.1. Mesh selection Plaxis	126
7.1.2. Rainwater flow in the unsaturated zone	128
7.1.3. Pressure	133
7.2. Retention curve parameters	137
7.3. BRM coupled analysis	143
7.4. Remedial measures	145
8. Conclusions and recommendations	146
8.1. Conclusions	147
8.2. Recommendations	149
Acknowledgements	150
References	151

Appendices

Appendix 1	Geological map
Appendix 2	Physiographic regions of the Big Rock Mesa area
Appendix 3	Instrumentation and dewatering system location map
Appendix 4	Geotechnical cross section A-A'
Appendix 5	Geotechnical cross section B-B'
Appendix 6	Geotechnical cross section C-C'
Appendix 7	Geotechnical cross section D-D'
Appendix 8	Geotechnical cross section E-E'
Appendix 9	Geotechnical cross section F-F'
Appendix 10	Geotechnical cross section G-G'
Appendix 11	Geotechnical cross section H-H'
Appendix 12	Geotechnical cross section I-I'
Appendix 13	Slope inclinometer data overview
Appendix 14	Groundwater elevation and dewatering main slide
Appendix 15	Description rock formations
Appendix 16	Porosity table
Appendix 17	Graphs Hoek-Brown and Mohr Coulomb
Appendix 18	SWAP input file
Appendix 19	Effective rainfall data

Symbol list

Greek

α	slope angle (°)
γ_p	psychrometric constant (kPa/°C)
ε	strain (^e)-elastic (^p)-plastic (-)
ε_s	shear strain(-)
ε_v	volumetric strain (-)
η_0	intrinsic viscosity (kPa s)
θ_s	saturated volumetric water content (-)
θ_r	residual water content (-)
ι	Lode's angle (°)
κ^*	modified swelling index (-)
κ_s	elastic stiffness changes for suction (-)
Λ	dimensionless suction (-)
λ_o^*	modified compression index (-)
λ_p	plastic multiplier (-)
ν	poisons ratio (-)
ζ	parameter controlling the rate of increase of soil stiffness with suction (kPa)
ρ_w	density water (kg/m ³)
σ'	effective stress (kPa)
σ	total stress (kPa)
σ_c	uniaxial compressive strength with suction (MPa)
$\sigma_{c,sat}$	uniaxial compressive strength for saturated conditions (MPa)
τ	shear stress (kPa)
φ	friction angle (°)
ϕ	pressure head (m)
ϕ_{atm}	soil water pressure in equilibrium with air relative humidity (m)
ϕ_c	capillary height (m)
χ	suction coefficient (-)
ψ	dilatancy (°)
ω	latent heat vapouration (MJ/kg)

Latin

a_c	critical acceleration (m/s ²)
a_r	empirical parameter Fabre and Gustkiewics (-)
b	Biot coefficient (-)
C_d	bulk surface resistance and aerodynamic resistance coefficient (-)
c_r, a_r, m_i	material constants (Hoek and Brown) (-)
c	cohesion (kPa)

c_c	effective capacity
D	displacement (m)
D_d	disturbance factor (-)
d_m	thickness slip surface (m)
d_s	grain size (m)
E	Youns modules (MPa)
EH	element height (m)
ET_0	Evapotranspiration, with grass as reference crop (mm/h)
E_i	intact rock stiffness (MPa)
E_{rm}	rock mass stiffness (MPa)
E_{max}	maximum evaporation (mm/s)
e	void ratio (-)
e_o	initial void ratio (-)
F	dimensionless interparticle force (-)
FS	Safety factor (-)
f	interparticle force (N)
f_{1to6}	yield surfaces (kPa)
GSI	Geological Strength Index (-)
g	gravitational acceleration (9.81 m/s ²)
g_{1to6}	plastic potentials (kPa)
g_a	van Genuchten empirical parameter (m ⁻¹)
g_l	van Genuchten empirical parameter (-)
g_m	van Genuchten empirical parameter (-)
g_n	van Genuchten empirical parameter (-)
H	Modulus of elasticity for soil structure with respect to change in matric suction
I_a	Arias Intensity (m/s)
J	second stress invariant of deviatoric stress tensor (kPa)
K_m	mineral compressibility (kPa)
K_s	macroscopic compressibility (kPa)
k	permeability (m/s)
k^*	average permeability (m/s)
k_{rel}	relative permeability (-)
l	slope of saturated vapour pressure curve (kPa/°C)
M	tangent of yield surface (kPa)
M_e	magnitude earthquake
MR	modulus reduction factor (-)
m	variation of the viscosity with the applicable excess shear stress (kPa s)
n	porosity (-)
o_a	actual vapour pressure (kPa)
o_s	saturated vapour pressure (kPa)

p	mean net stress (kPa)
p'	mean effective stress (kPa)
p'_c	pre consolidation stress (kPa)
p_c^*	pre consolidation stress for saturated conditions (kPa)
p'_r	reference stress (kPa)
p'_s	increase in cohesion with suction (kPa)
Q	discharge (m ³ /s)
q	Darcy flux (m/s)
R	radius particle (mm)
R_e	distance to the epic centre (m)
R_n	net radiation (MJ/m ² h)
R_s	radius curved water surface (°)
RF	rainfall factor (-)
r	parameter max soil stiffness (-)
S	degree of saturation (-)
S_a	extraction rate by plant roots (cm/cm ³ s)
S_d	extraction rate by drain discharge in saturated zone (1/s)
S_e	effective saturation (-)
S_m	extraction rate with macro pores (1/s)
S_r	residual saturation (-)
S_s	saturated saturation (-)
s	matric suction (kPa)
s^*	modified suction (kPa)
T_a	mean hourly ait temperature (°C)
T_s	surface tension (N/m)
t	time (s)
U_2	wind speed at 2 meter (m/s)
u_a	air pressure (kPa)
u_w	pore water pressure (kPa)
$V_a^{\text{'}}$	air volume (m ³)
$V_o^{\text{'}}$	initial volume (m ³)
$V_s^{\text{'}}$	specific volume (m ³)
$V_v^{\text{'}}$	void volume (m ³)
$V_w^{\text{'}}$	water volume (m ³)
w	half space separation (mm)

Matrices

$\underline{\underline{C}}$	damping
$\underline{\underline{D}}^e$	elastic stress-strain
$\underline{\underline{H}}$	permeability
$\underline{\underline{K}}$	stiffness
$\underline{\underline{L}}$	differential operator
$\underline{\underline{M}}$	material stress-strain
$\underline{\underline{N}}$	shape functions
$\underline{\underline{Q}}$	coupling
$\underline{\underline{S}}$	compressibility
$\underline{\underline{Y}}$	mass

Vectors

$\underline{\varepsilon}$	strain
$\underline{\sigma}$	stress
$\Delta \underline{f}_u$	incremental load
\underline{G}	vector for the effect of gravity on flow in vertical direction
\underline{n}	outward pointing normal vector
\underline{p}	body forces
\underline{q}_p	flux on boundaries
\underline{r}	nodal displacement
\underline{v}	discrete nodal values

1. Introduction

Following the news, reports on landslides, mudslides and dike failures are frequent. Such failures happen all over the globe and occur mainly during raining seasons. In populated areas these failures are often catastrophic and cause the loss of lives. Due to the climate change it is anticipated that more and heavier rainfall will happen in the future. Thus there is a great need for preventing slopes and dikes to become instable. Appropriate measures will be necessary to encounter this problem. A tool that can predict the stability of slopes in relation to rainfall is pivotal in this effort. Moreover, such a tool will enable to study the effectiveness of methods to control the slope stability. In this research, the relation between rainfall and groundwater level will be addressed. Also the related effect of pore pressures on the soil mechanical behaviour is dealt with. In particular, the coupling between groundwater changes and the unsaturated zone mechanics is studied in view of slope stability. Finally, a specific case has been implemented in a recently developed Finite Element (FE) code that includes aforementioned soil mechanical aspects to model the stability of slow moving landslides.

The case studied here is the Big Rock Mesa (BRM) that covers an area of 55 ha. This slow moving slide is located along the Pacific coast line near the city of Malibu (California). Currently, there are 145 houses built on the BRM and 57 houses are located along the beach at the bottom of the slope. Past monitoring has shown that slide movement occurs after heavy rainfall periods. Evapotranspiration reduces the infiltration of the rain water into the soil. The evapotranspiration is dependent on the temperature and the type of vegetation. In the summer temperatures are highest and thus also the evapotranspiration. In the winter months, when rainfall is dominant, the evapotranspiration is however diminutive. Besides the rainfall, also earthquakes are a threat for the stability of the slide. There are some smaller faults near the BRM that cause quakes, but the large and infamous San Andreas Fault is located about 100 km from the BRM. These faults may cause strong quakes and thereby initiate movement of the BRM.

Changes in the groundwater level go hand in hand with changes in the pore pressure distribution. Above the groundwater table suction is active, below the groundwater table pore water pressures are active. Reduction of the suction and thus introduction of pore water pressure due to rising of groundwater table leads to strength reduction of the soil. However, when the suction increases, either by lowering of the groundwater table or by evapotranspiration at the surface, the soil strengthens. This phenomenon is described in the unsaturated zone mechanics.

The coupling of groundwater changes with soil displacement and unsaturated zone mechanics is newly introduced in the Finite Element (FE) modelling by Plaxis. A Beta version of Plaxis 10 has been used to model the effect of rainfall on the stability of the BRM landslide. To this end, actual rainfall data and groundwater level measurements in the period 2003 to 2005 have been analyzed and applied.

First a general overview of the processes involved in slope failure is presented in Chapter 2. Next, the geological, hydrological and seismic data of the BRM landslide are discussed in Chapter 3. Then, the unsaturated zone mechanics is dealt with in Chapter 4. In Chapter 5, the FE modelling and the material models used in Plaxis are elaborated. In Chapter 6, a justification is given for the material parameters used in the modelling of the BRM slide. The results of a sensitivity study on the BRM are presented in Chapter 7. Finally, the conclusions from this study and the recommendations can be found in Chapter 8.

2. Slow moving landslides

Slow moving landslides are generally stable, but can be influenced to move due to different phenomena. These types of landslides occur all over the world and under different conditions. In this chapter the phenomena that can initiate the movement of landslides will be discussed briefly. The shear zone along which the slide may occur will be addressed. The effect of precipitation on slow moving landslides is the main focus of this study. Promotion of evapotranspiration is considered as a remedial measure in the parametric study. Further, the effects of earthquakes will be included in this study, because the case slope, Big Rock Mesa that will be analyzed is located in an earthquake prone area. To that end, the focus of this literature survey will also be on those phenomena and certain example slides will be evaluated. Also monitoring and dewatering methods are discussed.

2.1. General aspects of landslides

Landslides occur under the influence of several phenomena. When the shear zone of a slide is known, which is often the case for slowly moving slides, the material properties are of vital importance. Slides that are slow moving are often triggered by external continuous changes of conditions.

2.1.1. Phenomena affecting the stability of the slope

There are several phenomena that play a role in the stability of landslides, such as: seepage, weathering of rock, river and coastal erosion, change in evapotranspiration, the intervention of humans, earthquakes and precipitation.

In this Section, all the phenomena mentioned that affect the stability of a slope are briefly addressed. In the following Sections precipitation, evapotranspiration and earthquake influences on landslides are elaborated.

Seepage

In case of permeable soil, such as sand and gravel overlying less permeable soils, groundwater builds-up. The groundwater elevation is therefore higher in the permeable soils than the less permeable layers underneath. When rainfall seeps into the ground until it reaches the impermeable layer, it builds up and flows along that layer to the slope face. There the slope will be eroded. At the slope face a spring is created which undercuts the slope. The erosion and undercutting leads to loss of resistance force of the slope.

Weathering of rock

The weathering process involves two main types of weathering: Physical and Chemical weathering.

Physical weathering is the breakdown of rock into small fragments by physical processes without a change in chemical composition (Hamblin, Christiansen, 2001). A type of physical weathering is ice wedging where water seeps into fractures of the rock. When it freezes the water turns into ice and expands (about 9%) and exerts a great pressure on the rock. Another form of physical weathering is sheeting, which involves pressure relief instead of adding pressure. In this process a deep layer experiences pressure relief when the load of overlying layer disappears.

Chemical weathering is the breakdown of minerals by chemical reactions with the atmosphere or hydrosphere (Hamblin, Christiansen, 2001). These processes include dissolution of minerals into solution, hydrolysis and oxidation.

In nature physical and chemical weathering of rock occur simultaneously. The weathering process is influenced by various factors: mineral composition, porosity and climate.

Rock strata consist out of different types of rocks when these rocks weather overtime the rate of this process is different for each rock type.

Weathering of rock reduces the strength and therefore the stability of the slope. Cracks and faults in unfavourable directions may lead to the collapse of a whole section of a rock.

River and coastal erosion

River currents are involved in three main processes in shaping of land, namely: erosion, transportation and deposition. Which of these processes are active, depends on the velocity of the water and the particle size. Erosion occurs at fairly high water velocities (>10 cm/s). With higher water velocities larger particles are eroded.

Coastal erosion is caused by heavy storms lashing against the coastline and lateral drift by sandy beaches. The rate at which wave action cuts away at the shore line is extremely variable. It depends on the configuration of the coast, the size and strength of the waves and the physical properties of the soil or rock. In the case of loose material, such as deposits or glacial moraines the erosion rate can be up to 30 m/y. However, the erosion rate along most coasts is lower.

Both processes lead to the undercutting of the slope, which results in loss of resistance force of the slope. Ultimately, this loss of stability of the slope may lead to failure.

Human intervention

Roads, houses and other constructions build on slopes by people bring about changes in their equilibrium state. These constructions cutting into the slope can result in failure of the upper slope. Another consequence of building on a slope is that it changes the hydraulic system of the area. This could cause water to build up and form a spring, which undercuts the slope.

The bursting of water pipes, privately installed waste disposal systems and other forms of underground water structures can all add to the groundwater level.

Earthquakes

Earthquakes are caused by tectonically behaviour of the earths crust. Quakes are seismic waves which apply a dynamic loading and displacement on the soil and rock they travel through. This phenomenon causes high peak stress in the subsurface. High peak stress cause rocks to fracture and strata to deform. In cohesion-less soil, excess pore pressures are generated when water cannot efficiently drain away. Excess pore pressure results in loss of the shear strength. The loss of shear strength due to seismic loading is called earthquake induced liquefaction.

Precipitation

Precipitation or rainfall, especially during heavy storms, cause a temporarily rise of the groundwater level. Elevation of the groundwater levels co-insides with an increase in pore water pressure and thus a decrease of the effective stress. This can result in movement along a shear zone of an existing slope or complete failure of a slope.

The time it takes for the rainwater to reach the groundwater level depends on the properties of the unsaturated zone and the thickness of this zone. Due to low permeabilities and long unsaturated zone thickness it may take about a month before rainfall water reaches the groundwater level. In Chapters 4 and 6 this aspect is further elaborated.

Change in evapotranspiration

The water that effectively reaches the groundwater during rainfall is the precipitation minus the evapotranspiration. So, when the evapotranspiration decreases, more water will reach the groundwater, which will lead to higher groundwater levels. Evapotranspiration of water is evaporation into the atmosphere and transpiration by vegetation. Both processes are mainly influenced by temperature. At high temperatures the evapotranspiration is higher than at lower temperatures. Thus, changes in the evapotranspirations occur with temperature changes and changes in the vegetation.

2.1.2. Shear zone

A landslide is slope that failed along a shear plane. This plane can be planar or circular. The shear zone of a slide is the surface along which the slide displaces. This zone can be a few centimetres in soft soils to a few meters in harder soils and rock. In this section the standard Bishop slope stability method is briefly addressed. An important test used for determining the properties of a shear zone is the ring shear test, which is also discussed in this section.

Slope stability analyse; Bishop Method

A slope is stable when the passive resisting forces are greater than the active forces. An equilibrium of forces results in a stable slide, which has no displacement. Changes in this equilibrium can result in minor displacement to complete failure of the slope.

In the analysis of circular arced slopes, the slide is subdivided into vertical slices. The most commonly accepted method for this analysis is the Bishop method. In this method the inconsistency of the friction angle (ϕ) and the angle α along the surface is incorporated. In Figure 2.1 the forces operating on a slice are shown.

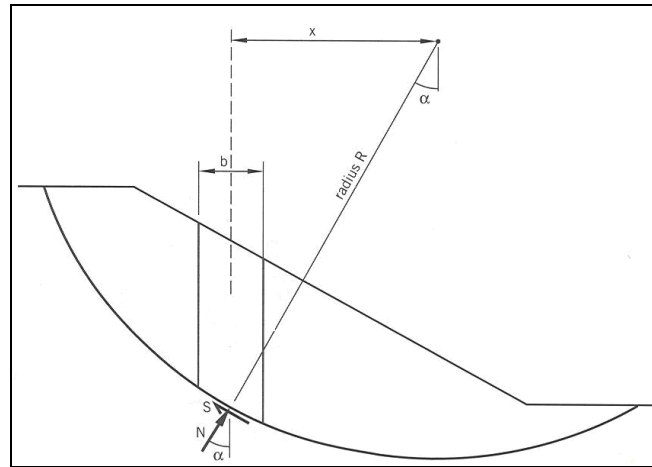


Figure 2.1 Forces operation on the slide (Cornforth,2005)

The factor of safety of the slide is given by:

$$F = \frac{\text{total available shear (or moment) resistance}}{\text{shear force (or moment) needed for static equilibrium}}$$

The Bishop's solution for the factor of safety is defined by (see Cornforth, 2005):

$$FS = \frac{\sum(c' + (W - u_w) \tan \phi') \frac{\sec \alpha}{1 + \frac{1}{F} (\tan \phi' \tan \alpha)}}{\sum W \sin \alpha} \quad [2.1]$$

where, W is the weight of the soil, ϕ is the internal angle of friction, c is the cohesion and u_w is the pore water pressure. The other symbols are defined in Figure 2.1.

To determine the parameters for each slide, ideally a sample of the soil at the shear zone should be tested in one of the laboratory tests listed in this Chapter. Unfortunately, this is not always possible; instead a soil representing the soil in the shear zone is tested and interpreted. Also educated estimations of these parameters are made, when it is not possible at all to retrieve a sample.

Slow moving slides

Slow moving slides are slides that already failed and thus a shear zone has been established. Movement occurs under certain circumstance and is usually small. In most slow moving slides, the movement is related to the groundwater fluctuations. This is further evaluated in Section 2.2. This study revolves around the case of the Big Rock Mesa landslide in California. This landslide is a slow moving landslide where the location of the shear zone is known. Past research has shown that there is a correlation between movement and rainfall (Fugro West Inc.). The slide consists mainly of sandstone with intrusive basalt layers. In Chapter 3 the Big Rock Mesa is presented in more detail and the monitoring data are evaluated.

Ring shear test

The ring test has the same concept as the shear box test. However, the ring shear test consists out of circular upper and lower boxes which rotate in opposite direction, as displayed in Figure 2.2. The advantage of this test, compared with the shear box test, is that it is continuous. As with the shear box test, the shear plane is imposed on the sample by the apparatus. The ring shear test is used to determine the residual shear strength, friction angle and cohesion of the soil sample.

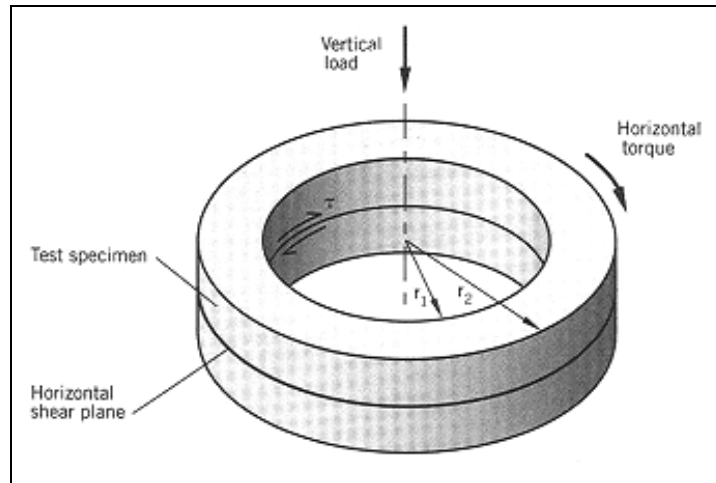


Figure 2.2 Ring shear apparatus (Cornforth, 2005)

Viscosity of the shear band

The thickness of the shear zone is dependent on the soil type and can vary from a few centimetres to a meter thick. During movement the displacement in the shear zone is plastic. The viscosity of the shear band of the landslide stands in relation with the velocity of that slide. In Equation 2.2 (for derivation see: van Asch et al., 2007), the relationship between the velocity, viscosity and shear strength for a landslide is shown.

$$v_s = \frac{d_m}{\eta_0} (\tau - \tau_0)^m \quad [2.2]$$

where:

v_s = velocity (m/s)

d_m = thickness slip surface (m)

η_0 = intrinsic viscosity of material (kPa s)

τ = shear stress (kPa)

m = variation of the viscosity with the applied excess shear stress

The lower its viscosity is the higher the speed of the slide. The material in the shear band forms thus a kind of lubricant for the slide. When displacement of the landslide occurs, excess pore pressures can build up and contribute to the lowering of the viscosity in the shear zone. When the displacements stop, consolidation in the shear zone can lead to strength regain (van Asch et al. 2007).

The viscosity in the shear band depends on the pore pressure. Since the pore pressure increases when the groundwater levels rises, and the effective stress decreases, the viscosity also decreases.

Research by van Asch et al. (2007) on three landslides in the French pre-Alps showed that in slow-moving landslides the intrinsic viscosities is lower when groundwater levels rises. Also the dependency on excess shear stress is lower when the groundwater levels rise. In this study, a ring shear test on soil samples of the three landslides was performed. From these tests it followed that the viscosity parameters were 10 to 1000 times lower than in back calculation of field observations. In Table 2.1 the viscosities of the three slides determined with ring shear tests and with back analysis from field velocities are listed. Viscosities derived from shear test can diver largely from reality.

Slide	Texture	η_0 from ring shear test (kPa s)	η_0 from back analysis from field velocities (kPa s)
La Valette	Sandy Silt	7.1E4	1.23E7
La Mure	Clay/Silt	5.1E3	1.3E7
Hau	Sandy clay	9.2E3	1.2E5

Table 2.1 Viscosities from ring shear test and from back analyses for three landslides (van Asch, 2007)

2.2. Movement of landslides caused by rainfall, evapotranspiration and earthquakes

A further analysis of the effect of precipitation, evapotranspiration and earthquakes on slow moving landslides is given in this Section. The analysis is supported by a few examples of landslides under different conditions.

2.2.1. Landslide movement caused by rainfall

During periods of rainfall the groundwater level rises and during the dry periods the groundwater level lowers. These groundwater fluctuations influence the pore water stress, the effective stress and consequently the stability of the shear zone.

The groundwater situation can be divided into the following zones: the dry zone, the unsaturated zone and the saturated zone. In the dry zone no ground water is present. In the saturated zone the pore space is completely saturated with water. The unsaturated zone is the transition zone between the saturated and dry zone. The unsaturated zone is the most complex zone, because there is an interaction between three different phases: liquid (water), gas (air) and solid (soil particles). Whereas in the dry and saturated zone only interaction between two phases is occur: solid and gas phase interaction and solid and liquid phase interaction, respectively.

The saturated zone determines the fluctuations in the groundwater level due to increase or decrease of infiltration water. In this study those fluctuation play a crucial role. Hereto, a more elaborate literature survey is necessary which is conducted in Chapter 4.

In this Chapter the effect of groundwater fluctuation is evaluated for two different landslides under different conditions. The following case studies will be presented: Predicting the variation of stability with time for a slope in Switzerland (Thielen, Springman, 2008) and the Villerville-Cricqueboeuf landslides in Normandy (Lissak, Maquare, Malet, 2009). These case studies serve as a reference for the case study discussed in Chapter 3 and 6.

Predicting the variations of stability with time for a slope in Switzerland

After a great number of slopes that failed in an area where heavy rainfall events occurred, an investigation was conducted to study the slope stability with time due to suction changes. The slide consists of organic soil on top of, a layer of clayey sand layer of 1.5m thick with a silty sand layer beneath. These layers are on top of a sandstone base. Field experiments over a period of two years were performed on a test slope. From laboratory tests the water retention curve, saturated and unsaturated permeability and the saturated and unsaturated shear strength was determined. Two software programs were used to analyse the behaviour of the slide. The Finite element (FE) program Vadose/W calculated the time dependent pore pressure distribution from water, vapour and heat flow in the saturated and unsaturated zone. The factor of safety was calculated from the pore water pressure distribution using an equilibrium method that is included in the program Slope/W. In the calculation with the FE program Vadose/W the influence of suction was taken into account.

In Figure 2.3 the pore water pressure (PWP) change with time over 2005 is illustrated at different depths as obtained from calculations and measurements. Around day 151 an increase in suction (negative pore water pressure) is observed. In Figure 2.4 the Factor of Safety starts to increase also around day 151. Hence, there is a strong correlation between increasing suction and slope stability.

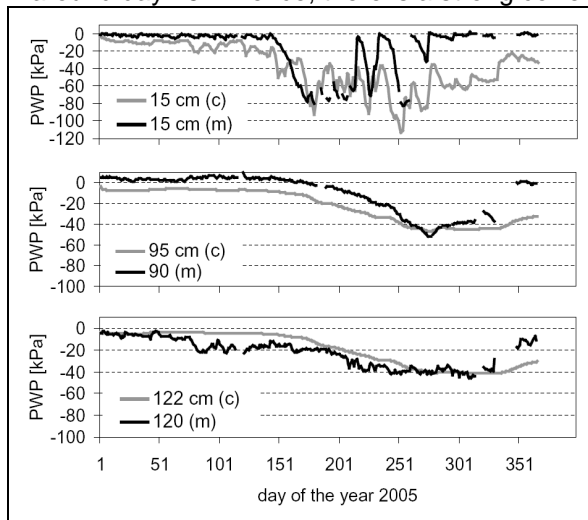


Figure 2.3 Comparison of the calculated (c) and measured (m) soil suction at different depths for 2005.

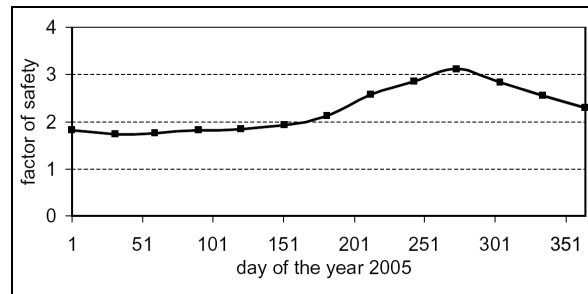


Figure 2.4 Development of the factor of safety during 2005.

The correlation between suction in the unsaturated zone and the factor of safety is demonstrated in this research. Suction strengthens the soil by 'bonding' the particles of the soil skeleton. This phenomenon is called suction induced cohesion and will be further discussed In Chapter 4.

Villerville-Cricqueboeuf landslides in Normandy (Lissak, Maquare, Malet, 2009)

In Normandy (France) the Calvados coastal slopes are periodically affected by landslides. A map of the location of these slopes are shown in Figure 2.5. The two landslides indicated in Figure 2.5, Cirque des Graves and Fosse du Marce, are slow moving landslides.

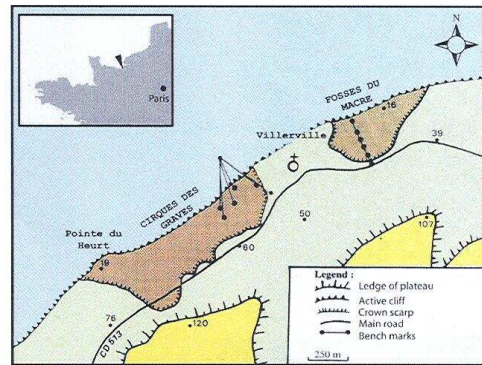


Figure 2.5 Map of the Calvados coastal slopes

The Cirque des Graves landslide first failed in January 1982. After this first failure three other crises happened in February 1988, January 1995 and March 2001. All these crises occurred during wintertime after freezing and heavy rainfall. The geological profile of the slope is displayed in Figure 2.6 and shows the soil profile. This profile consists of Kimmeridgian marl, Genomanian chalk, glauconite, Albian sand and slope deposits. Besides climate influences the slopes were also affected by coastal erosion. In the research done by Lissak, Maquare and Malet, 2009, the influence of erosion was excluded.

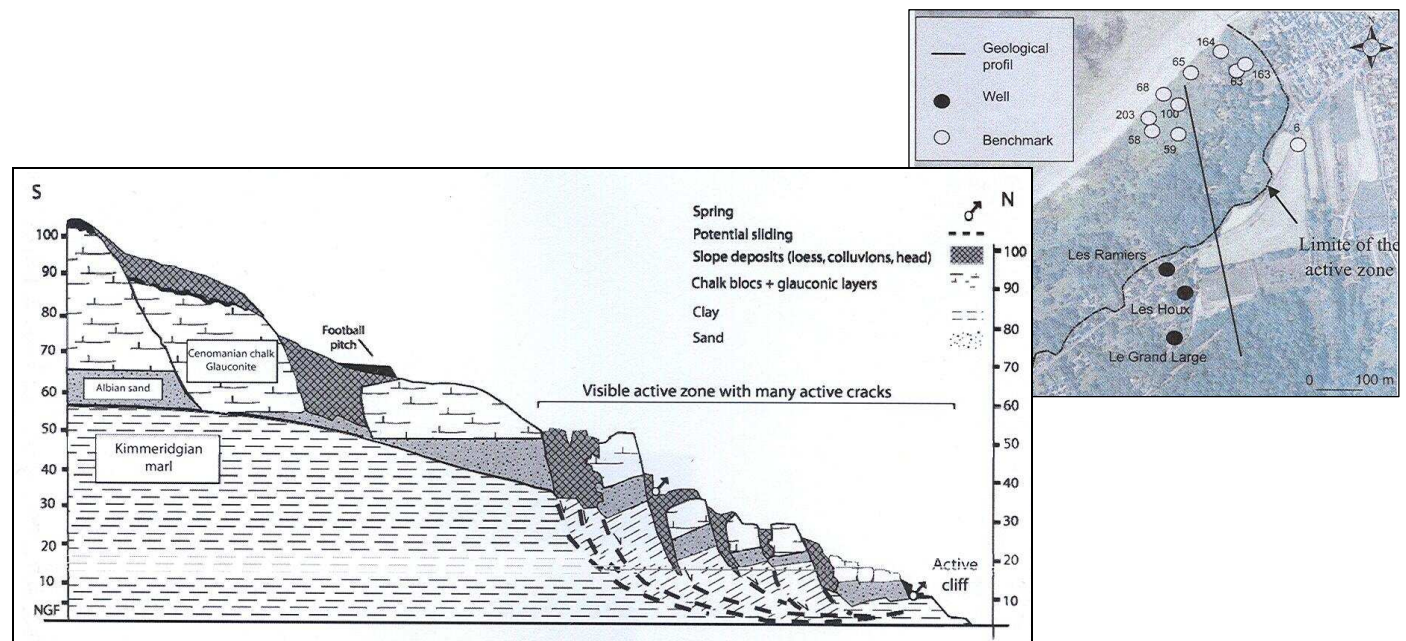


Figure 2.6 Geological profile of Cirque des Graves landslide

In 1984 the field monitoring of the area started. The groundwater fluctuations are correlated with high effective rainfall (i.e. precipitation minus evapotranspiration). The annual groundwater level is generally around 12 m below the surface. During the failure of 1982, the groundwater level was raised by 4 m. The groundwater level during the reactivations of the slide in 1988, 1995 and 2001 was raised with 3 m. The relation of effective rainfall, groundwater elevation and slope displacement is presented in Figure 2.7.

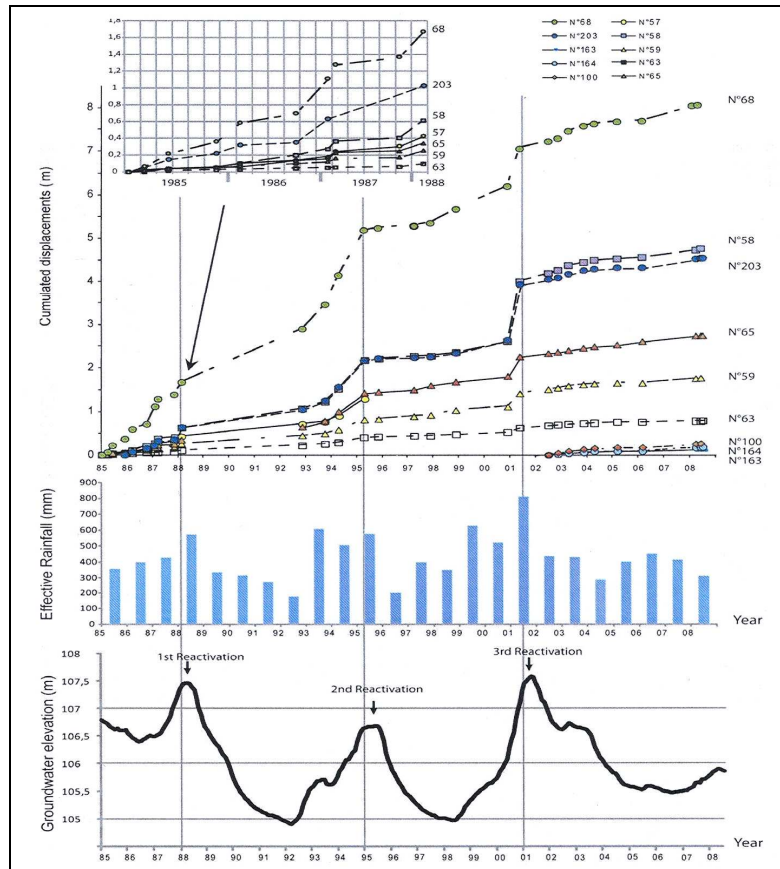


Figure 2.7 Effective rainfall, groundwater elevation, slope displacement

From this study the relation between rising groundwater table due to rainfall infiltration and slope movement is apparent. In the years where the effective rainfall was high, movement occurred. The amount of movement correlates with the amount of groundwater elevation.

Anomalies in the correlation, such as the relative large displacement registered at N° 86 in 1995, is possibly due to coastal erosion.

2.2.2. Influence of evapotranspiration on landslide movement

The effective rainfall that contributes to the elevation of the groundwater level is the actual rainfall minus the evapotranspiration. The evapotranspiration consists of evaporation into the atmosphere and the consumption by vegetation. The evaporation mainly depends on the temperature in the area. The water consumption by the vegetation in the area depends on its type of vegetation.

Changes in the evapotranspiration can be caused by a number of reasons:

- Fire, which destroys the vegetation.
- Development of infrastructure in the area (which limits the vegetation growth).
- Natural season changes.

To estimate the evapotranspiration in an area the following Penman-Monteith equation can be used (www.cimis.water.ca.gov):

$$ET_0 = \frac{l(R_n - G)}{\omega[l + \gamma_p(1 + C_d U_2)]} + \frac{\omega \frac{37}{T_a + 273.16} U_2 (o_s - o_a)}{l + \gamma(1 + C_d U_2)} \quad [2.3]$$

where:

- ET_0 = Evapotranspiration, with grass as reference crop (mm/h)
 l = slope of saturated vapour pressure curve (kPa/°C)
 R_n = net radiation (MJ/m²h)
 γ_p = psychrometric constant (kPa/°C)
 T_a = mean hourly air temperature (°C)
 U_2 = wind speed at 2 meters (m/s)
 o_s = saturated vapour pressure (kPa)
 o_a = actual vapour pressure (kPa)
 ω = latent heat vaporation (MJ/kg)
 C_d = bulk surface resistance and aerodynamic resistance coefficient

To give an indication of the evaporation, next the case study of the Beline landslide near Salins-les-Bains (Jura France). (Bogaard, van Asch, 2002) is presented. From this case study, it can be concluded that evapotranspiration has a significant impact on the velocity of landslide movement.

Beline landslide near Salins-les-Bains (Jura France). (Bogaard, van Asch, 2002)

The role of moisture balance in the unsaturated zone was investigated with respect to the movement and stability of this slide. Especially the effect of precipitation and evapotranspiration (in the form of vegetation) was analyzed. The unsaturated zone was modelled using 1D and 2D hydraulic models (details of these models can be found in van Bogaard, van Asch, 2002). The measured displacements could best be described with the visco-plastic creep model of Yen, 1969.

The groundwater model was capable of modelling the average groundwater level and amplitude of the groundwater level, but failed to model the dynamics and the precise timing of the fluctuations. However, the water balance of the Beline slope is well represented.

In this study, the influence of evapotranspiration was analyzed. In the calculation 10 and 20 percent increases and decreases were evaluated. The influence of a change in evapotranspiration was significant, especially for a decrease in evapotranspiration, which was explained with the non-linear behaviour of the unsaturated zone.

With the hydraulic models, the peak groundwater level was calculated and was used to calculate the maximum movement velocity of the landslide. From the simulations it was concluded that a decrease of 20% in evapotranspiration results in a 20-fold increase of the maximum velocity.

Evapotranspiration is an important factor in the water balance of the hydraulic system of the slide. Increase or reduction of the evapotranspiration has therefore a large influence of the movement of the slide. Reduction of the evapotranspiration due to for example, deforestation, cutting of plants or the lowering of temperature due to climate changes can lead to more effective rainfall and thus more movement of the slide. However, an increase in evapotranspiration may lead to reduction of the effective rainfall and less movement of the slide. Another advantage of increased evapotranspiration is that it will increase the suction and thereby enhances the cohesive strength of the soil in the unsaturated zone. In Chapter 4 this will be further elaborated.

In the study of the Beline-slide, an increase of evapotranspiration was considered as the main remedial measure to reduce the movement of a landslide.

2.2.3. Earthquake caused landslides

When an earthquake occurs, vibrations are travelling through the ground. These vibrations can be recorded with seismological measurement equipment. The ground accelerations in time are the most commonly used recording presentation.

As stated before, the vibration in the ground result in cyclic loading in the form of high peak stresses and pore pressures. To determine whether a landslide will displace due to these vibrations, calculation can be performed using Newmark's method as a first indication. In this method a critical acceleration factor is defined. If the accelerations generated by an earthquake surpass this critical acceleration factor, the slide will move. The displacement is calculated by double integrating the peak acceleration. The critical acceleration value can be calculated with:

$$a_c = (FS - 1) \sin \alpha \quad [2.4]$$

where

a_c = critical acceleration (percentage of the gravitation acceleration)

FS = static factor of safety

α = slope angle

This method has the following limitations (Ingles, Darrozes, Soula, 2006):

- The sliding mass is assumed to be a rigid-plastic body.
- No permanent displacements are allowed for accelerations below critical acceleration.
- Plastic deformation on the sliding surface is allowed when the critical acceleration is exceeded.
- The critical acceleration is not strain dependent and thus remains constant throughout the analysis.
- The static and dynamic shear resistance of the material are considered to be the same and constant.
- The effects of dynamic pore pressure are neglected.
- Only the horizontal component is taken into account.

Due to these limitations the Newmark method can only be used to obtain an indication for the displacement and critical failure point of landslides.

Predicting the earthquake induced slide displacements are based on empirical regression equations. These equations are often related to an area. For the Los Angeles area the displacement is expressed as a function of Arias Intensity I_a . The Arias Intensity is a single numerical measure of an acceleration-time record calculated by integrating the squared acceleration values over the entire duration (Chowdhury, 2010). Thus the displacement D is not limited to the high peak values of acceleration. The empirical regression equation for the Los Angeles area is given as (Chowdhury, 2010):

$$\log D = 1.52 \log I_a - 1.993 \log a_c - 1.546 \quad [2.5]$$

The Arias Intensity equals:

$$I_a = M_e - 2 \log R_e - 4.1 \quad [2.6]$$

where:

M_e = magnitude

R_e = distance to the earthquake source (m)

Alternatively dynamic analysis methods may be used, which reflect reality in more detail. These methods include time stress history, natural frequencies, effect of damping and the non-linear behaviour of the soil or rock. For dynamic Finite Element (FE) analysis the basic features are as

follows. The slope is subjected to inertia forces due to base acceleration for all nodal points (Chowdhury, 2010). The equation for motion is given by:

$$\underline{\underline{Y}}\ddot{r} + \underline{\underline{C}}\dot{r} + \underline{\underline{K}}r = R(t) \quad [2.7]$$

in which $\underline{\underline{Y}}$ the mass matrix, $\underline{\underline{C}}$ is the damping coefficient and $\underline{\underline{K}}$ the stiffness matrix, $R(t)$ external force with time and r is the nodal displacement.

Although the dynamic analysis gives a better representation of reality, it is a very complex analysis. More simple empirical equations give usually a good indication for slope displacement.

The influence of pore water pressures on stability of a landslide is further analyzed in the case study of Tsukidate landslide, Japan, (Wang, Sassa, Kukuoka, 2005). From this case study, it can be concluded that pore water pressure rises when the shear stress changes which in turn initiates shear displacement. The increase in pore water pressure is caused by the shear stress that alters the soil skeleton and decreases the pore space.

Tsukidate landslide, Japan, (Wang, Sassa, Kukuoka, 2005)

In Japan earthquakes occur frequently, therefore many landslides in that part of the world are a direct result of seismic loading. To analyze this phenomenon the seismic loading of the Tsukidate landslide was simulated for a series of tests on samples taken in the area.

To investigate the trigger and movement mechanisms caused by an earthquake, the seismic loading was synthesized using the seismic records of an earthquake.

In Figure 2.8 the contour map and cross-section of the Tsukidate landslide are presented. The following parameters of this slope have been determined: the angle of the slope was 13.5 degrees, the total mass movement was 5000 m³ and the average friction angle during failure was 7.3 degrees.

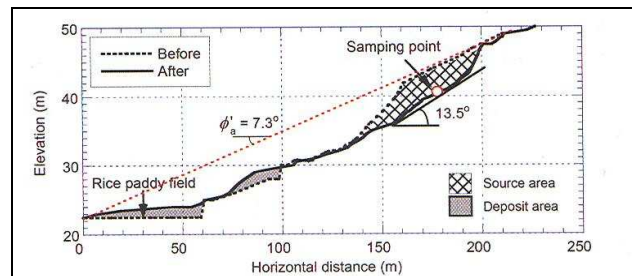


Figure 2.8 Cross-section of the Tsukidate landslide (Wang, Sassa, Kukuoka, 2005)

The soil sample used for testing mainly consisted of volcanic deposits because the liquefaction failure was mainly triggered in those deposits. Gravels greater than 4.75 mm were removed from the soil sample; assuming that the undrained shear behaviour of these samples will be mainly controlled by the matrix material when the gravel content is less than a certain percentage, say 40% (Wang, Sassa, Kukuoka, 2005).

In this research, a ring-shear apparatus (DPRI-7) was used. (Max shear speed 3.0 m/s, 270 mm inner diameter, 350 mm outer diameter). The initial normal stress in the field was approximately 75.1 kPa, and the shear stress 18.0 kPa. All tests were originated from this initial state.

To analyze the triggered shear failure due to seismic loading, a series of seismic simulation shear tests were performed using the recorded seismic waves during an earthquake. These tests were performed with undrained and partly drained soil samples. The results are presented in Figures 2.9 a, b, c and d.

Partly drained soil samples were introduced, because the slopes in natural conditions cannot be undrained fully, especially in the post-failure process where pore water can be dissipated with progress of shear displacement.

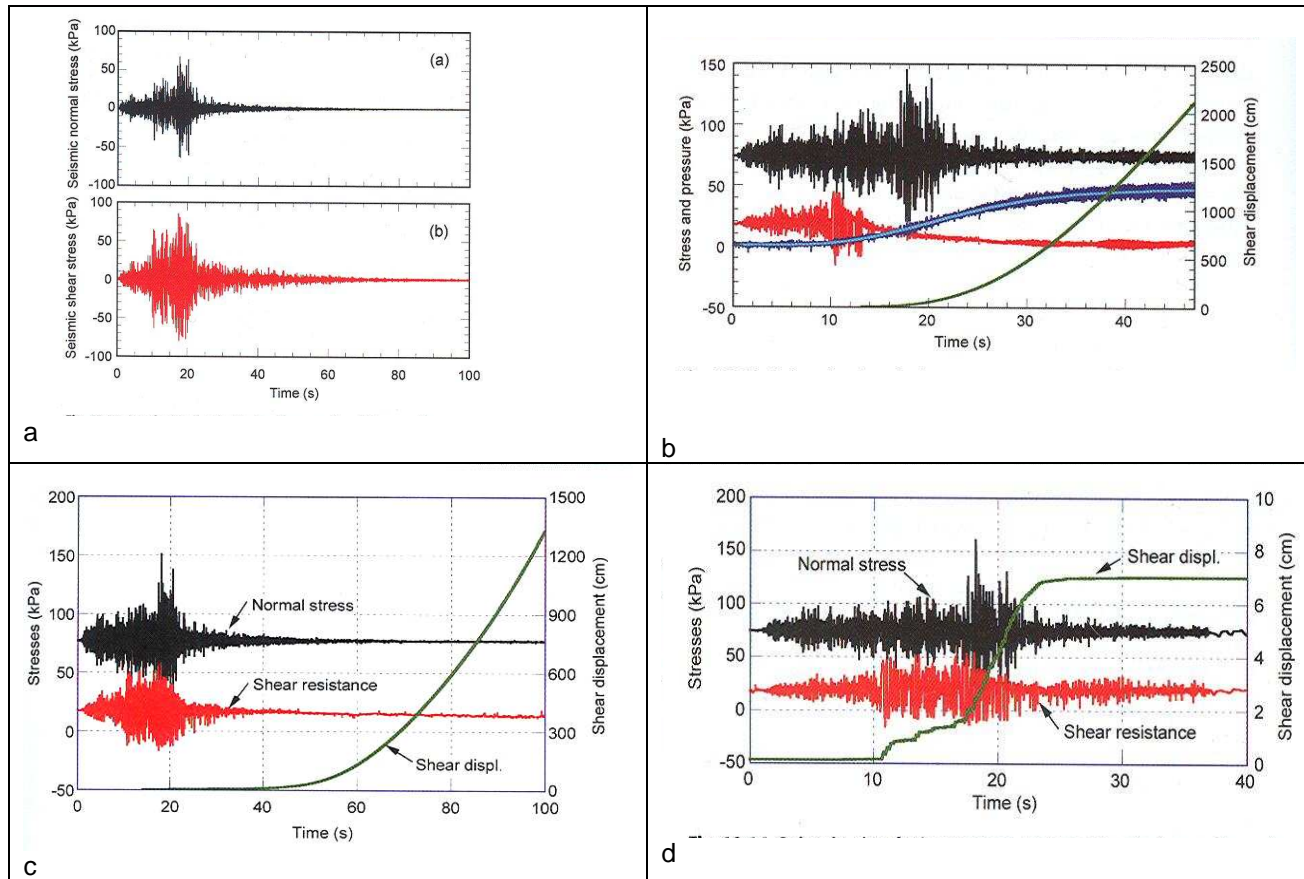


Figure 2.9 Ring shear test with cyclic loading, earthquake simulation (Wang, Sassa, Kukuoka, 2005)
 (a), synthesized seismic loading, (b) saturated sample under undrained conditions, (c) 5 meter thick soil cover simulation under partially drained conditions, (d) water saturated sample under partially drained conditions.

From Figure 2.9 b it can be concluded that in undrained conditions the pore pressure increases during seismic loading and levels out when the loading ceases. The shear displacement accelerated after the seismic loading ceased and the pore pressure tended to a constant value.

To simulate the 5 m thick soil cover on the shear plane, a fluid with 25 times the viscosity of water was used in the partly drained test, see Figure 2.9 c. From this observation it can be concluded that the shear failure was initiated during the seismic loading. After the main shock, although the shear resistance did not show significant reduction, the shear displacement increased continuously, showing an accelerating failure process. The dissipation of pore water pressure from the shear zone is key to the after-main-shock movement of displaced landslide mass (Wang, Sassa, Kukuoka, 2005).

To examine the role of possible dissipation of pore-water pressure, seismic simulation was performed on water-saturated soil samples under partly drained conditions. The result of this test is presented in Figure 2.9 d. From this test it is clear that shear failure was triggered due to seismic loading. When the seismic loading ceased, the shear displacement also ceased indicating that no 'long run' landslide was initiated.

From Figures 2.9 b and d, it is inferred that long run-out landsliding could be triggered in the case that the saturated soil layer above the sliding surface is thick enough, say 1 m (Wang, Sassa, Kukuoka, 2005). This also indicates that long run-out landslide can be prevented by effective drainage. In the event of an earthquake the behaviour of the material in the shear zone is significant. Seismic loading can increase the pore water pressure and initiate continuously increasing displacement. Drainage of the shear zone can limit the displacement significantly. The BRM consists mainly of sandstone and the shear zone of disintegrated sandstone, which means that the material is partly or more drained. Displacement of the slide could however still be dependent largely on the amount of seismic loading and therefore of the magnitude of the earthquake.

2.3. Monitoring of landslides

Various tools are available to monitor the behaviour of landslides. In this Section an overview of the available equipment is given.

Inclinometer

Inclinometers are the most commonly used monitoring tool to observe the movement of landslide. A casing is installed to a certain depth. The depth of the casing has to be lower than the shear zone of the slide. In the casing two sets of grooves are made in order to guide the inclinometer into the ground. One set of grooves is usually in the direction of the landslide movement. The other set is perpendicular to the first set. The inclinometer, as displayed in Figure 2.10 a, measures the tilt of the probe and of the casing in the plane aligned with the wheels. By taking successive readings an in-situ profile of the casing is obtained. A typical inclinometer data graph is shown in Figure 2.10 b. Here deviation of the casing is measured at a depth of 36 feet (12 m).

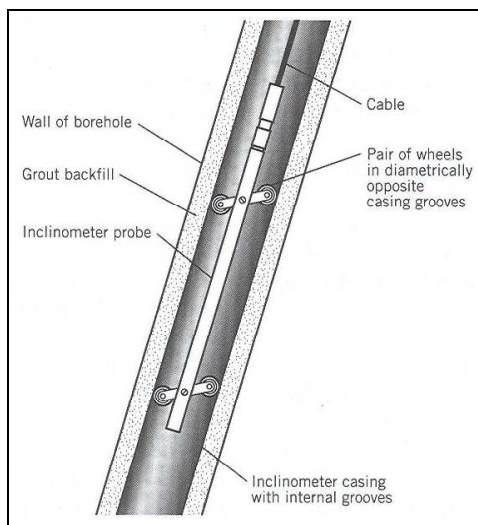


Figure 2.10 a Inclinometer (Cornforth,2005)

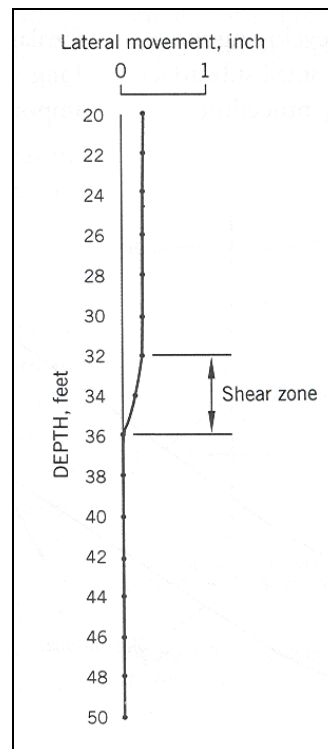


Figure 2.10 b Typical data graph (Cornforth,2005)

Piezometers

Piezometers are used to determine groundwater pressure. There are various types of piezometers. The most common are; standpipe, pneumatic and vibrating wire piezometers. The vibrating wire and pneumatic piezometers each use diaphragms that undergo very small changes (movement of pore water) to register pressure changes (Cornforth, 2005). The standpipe, however, has a water column that moves up and down. Because the water column needs time to stabilize, peak groundwater levels cannot be registered.

The standpipe, pneumatic and vibration wire are all installed in a similar manner; a sand intake sealed with bentonite and cement-bentonite grout as illustrated in Figure 2.11. The best results are obtained with piezometers that are installed close to the shear zone of the landslide. If the equipment is installed too deep, the shear movement might destroy the pipe. If the sensor is too shallow, the measured groundwater pressure may be incorrect (Cornforth, 2005).

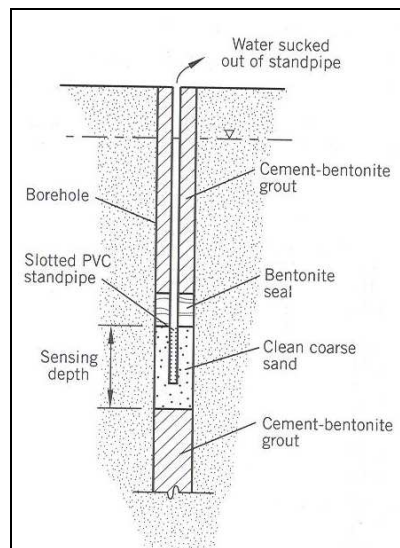


Figure 2.11 Standpipe piezometer (Cornforth, 2005)

Optical fiber

A new development in landslide movement detecting systems is the optic fiber (cable) that is made immune to electromagnetic interference and moisture and can be installed along a conventional casing. A fibre optic receiver converts the light intensity from the optical fiber into an electrical signal. If a portion of fiber is deformed by movement of landmass, the fiber exhibits excess light loss (Aulakh, 2008). When the fiber bends more sharply, light will be lost correspondingly. If the attenuation of light reaches a threshold value, a warning signal can be sent. The change in the rate of movement can be determined by plotting the light attenuation with time (Aulakh, 2008). In figure 2.12 sketches of installation locations of optical fiber wires. The advantage of installing this wire laterally is that the extent of the slide movement is incorporated.

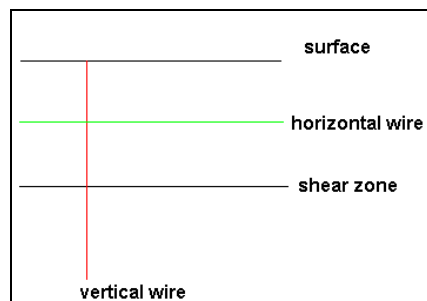


Figure 2.12 Sketch of the location of the wire in the soil profile

Earthquake monitoring

The magnitude of an earthquake is often indicated on the Richter scale. The Richter scale was introduced in 1935 by seismologist Charles Richter and is based on the magnitude of the vibrations. These vibrations can be detected with a seismograph. Basically a seismograph is an instrument which moves like the environment where it is located. A pendulum registers this movement see Figure 2.13.

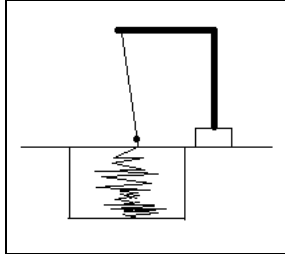


Figure 2.13 Principle of a seismograph

2.4. Dewatering methods

Dewatering systems are installed to drain the excess water in order to prevent landslide displacement due to elevating groundwater levels.

Horizontal drains

Horizontal drains are small-diameter slotted plastic pipes that are installed in holes drilled into soil or rock, usually at angles above horizontal (Cornforth, 2005). By placing these drains at an angle, water is drained by gravity to the outer surface; see Figure 2.14. Horizontal drains are used to lower the groundwater levels generally within the slope, and to tap into aquifers. In order to optimise the effectiveness of horizontal drains, a large number of drains ought to be installed. To uphold the effectiveness of drains regular inspection is necessary to detect clogging. Cleaning of horizontal drains can be done with the use of high-pressure water jets. Horizontal drains can be ineffective in clays and fine-grained soils.

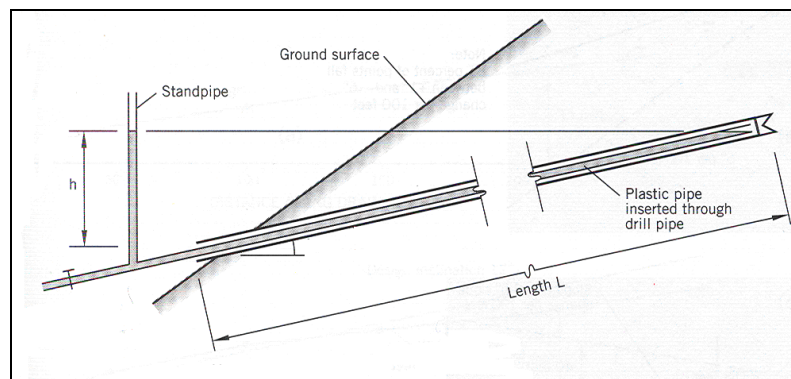


Figure 2.14 Typical horizontal drains (Cornforth,2005)

Wells

A well is installed in order to lower the groundwater level. In Figure 2.15 a typical well installation is displayed. From Figure 2.15 it is visual that a dewatering well is constructed with a casing connected to a well screen. Outside the well screen a filter pack from highly permeable soil is present. In the casing a pump is used for draining the water out. Thus a well is a vertical drain connected with a pumping mechanism.

For maintenance of the wells regular inspection is necessary to provide the required drawdown of the groundwater level. The screens can become clogged or dissolved by bacteria and chemicals. Replacement of screens, cleaning with water jets or chemicals can restore the well. Besides lowering the groundwater level vertical drains can be used to relief the artesian pressure in aquifers and as a gravity drain. A Gravity drain connects a permeable upper layer with a lower permeable layer. Thereby, the water is drained from the upper layer to the lower layer.

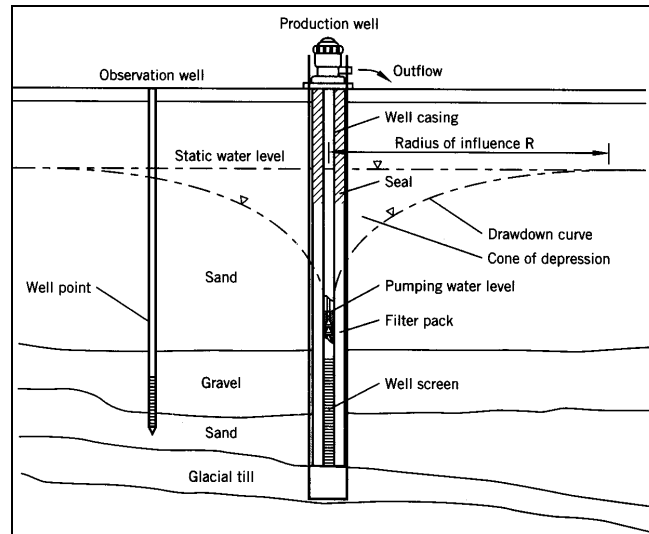


Figure 2.15 Typical well installation (Cornforth, 2005)

Trench drains

Trench drains generally are built of free-draining rockfill separated from the native fine-grained soils by a geotextile filter fabric (Cornforth, 2005). At the base of the trench a draining pipe is usually installed. This draining system is of moderate depth (maximum 6 m) and is most efficient when the groundwater level is close to the surface. Trench drains are installed parallel to each other as shown in Figure 2.17.

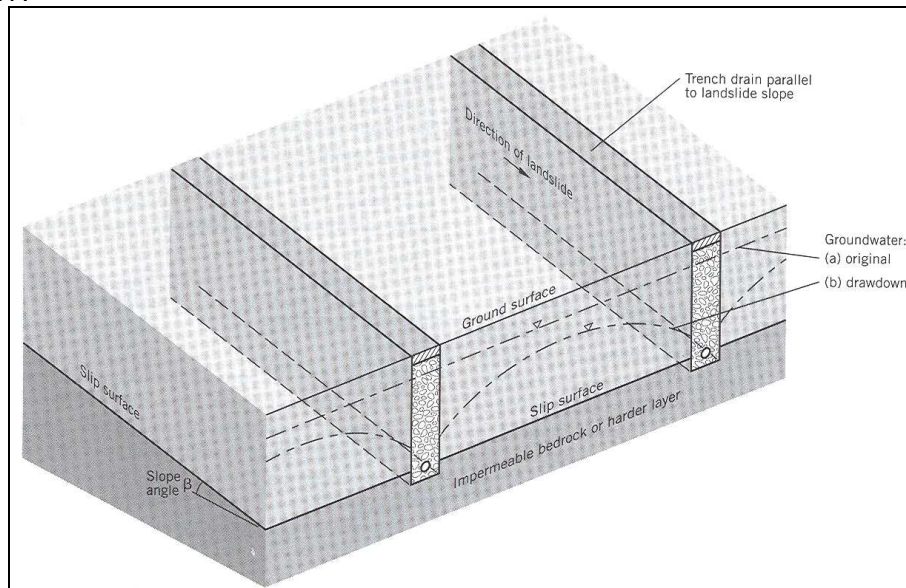


Figure 2.17 Parallel trench drains (Cornforth, 2005)

Filter system

Filter systems cover the outer slope in order to dissipate seepage pressures before reaching the surface. Another function of this filter system is protection of the slope surface against erosion by rainfall. A filter system can be graded filters or a single backed filter by geotextile, see Figure 2.18 (Cornforth, 2005).

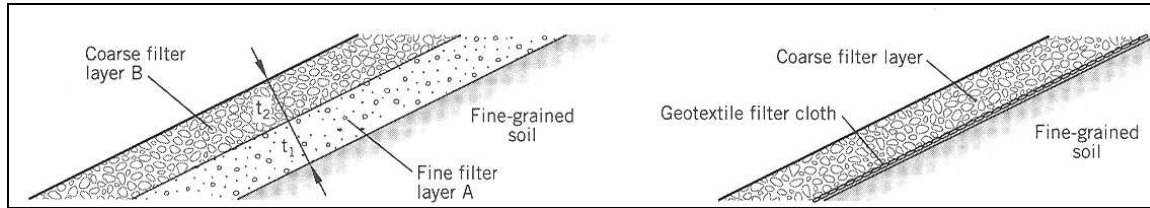


Figure 2.18 A graded filter and a single filter with geotextile (Cornforth, 2005)

3. Data evaluation for Big Rock Mesa Landslide

The Big Rock Mesa landslide is located in Malibu in LA County California. A map of the location of the landslide is displayed in Figure 3.1.

Most landslides consist of clays and loose soils. The Big Rock Mesa landslide, however, consists mainly of sandstone and basalt. Since California is highly prone to earthquakes it can be assumed that an earthquake initiated the Big Rock Mesa landslide. Also coastal erosion may have played an important role in the failure of the slope. The Big Rock Mesa landslide is monitored since 1989 following the displacement in 1983. The County of Los Angeles founded the assessment district Big Rock Mesa until the City of Malibu was incorporated and took over. The assessment district provides permanent funding to maintain and monitor dewatering facilities in order to reduce landslide movement (Report Fugro West Inc. 2006).

In this Chapter the geological and hydrological monitoring data of the landslide will be presented and analyzed.

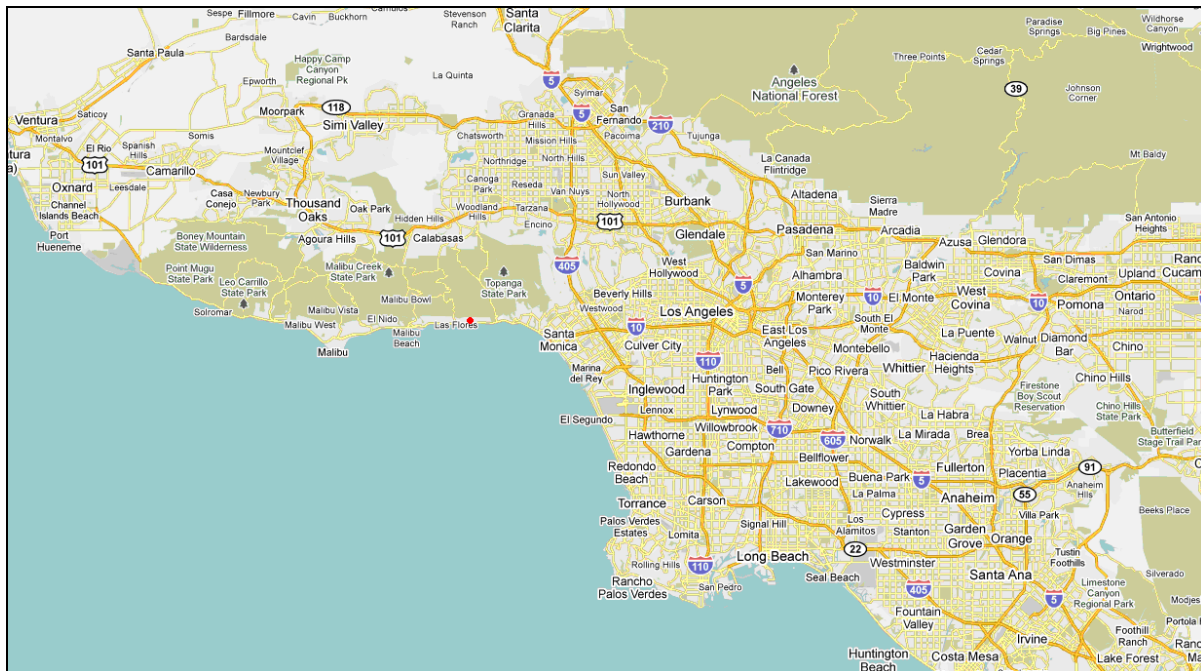


Figure 3.1 Los Angeles areas, the BRM is located at the red dot. (Google maps)

3.1. Geological evaluation

The geological evaluation presented in this Section includes general aspects, rock formation, ancient movement and current movement.

3.1.1. General aspects

The Big Rock Mesa landslide is located along the Pacific coastline in Malibu city and is moving towards the ocean. The Pacific coast highway cuts right through the landslide. Also 145 houses are built on the landslide and 57 houses are built along the coast line. The size measurements of the Big Rock Mesa landslide are:

- ♦ widest point (cross-section H-H' appendix 11) 3050 ft 930 m
- ♦ widest point (cross-section D-D' appendix 7) 2500 ft 762 m
- ♦ highest point (cross-section D-D' appendix 7) 1050 ft 320 m
- ♦ estimated surface area equals 55 hectare

See Figure 3.2 for an overview of the BRM and the location of the cross sections.

The Big Rock Mesa landslide is divided into several regions: Pacific coast highway (PCH), Bluff, Headscarp, Central mesa, Western extension and Eastern mesa. These regions are marked on the map in Appendix 2.

The Western region is not part of the main slide and will be excluded from this study. The boundaries of the Western region are marked green and the boundaries of the main slide are marked red in the map displayed in Figure 3.2. Besides the large main Big Rock Mesa (BRM) landslide, smaller 'sub' slides are active. This is clear particularly in cross-section D-D' in Appendix 7. The BRM is also displayed in Figure 3.2.

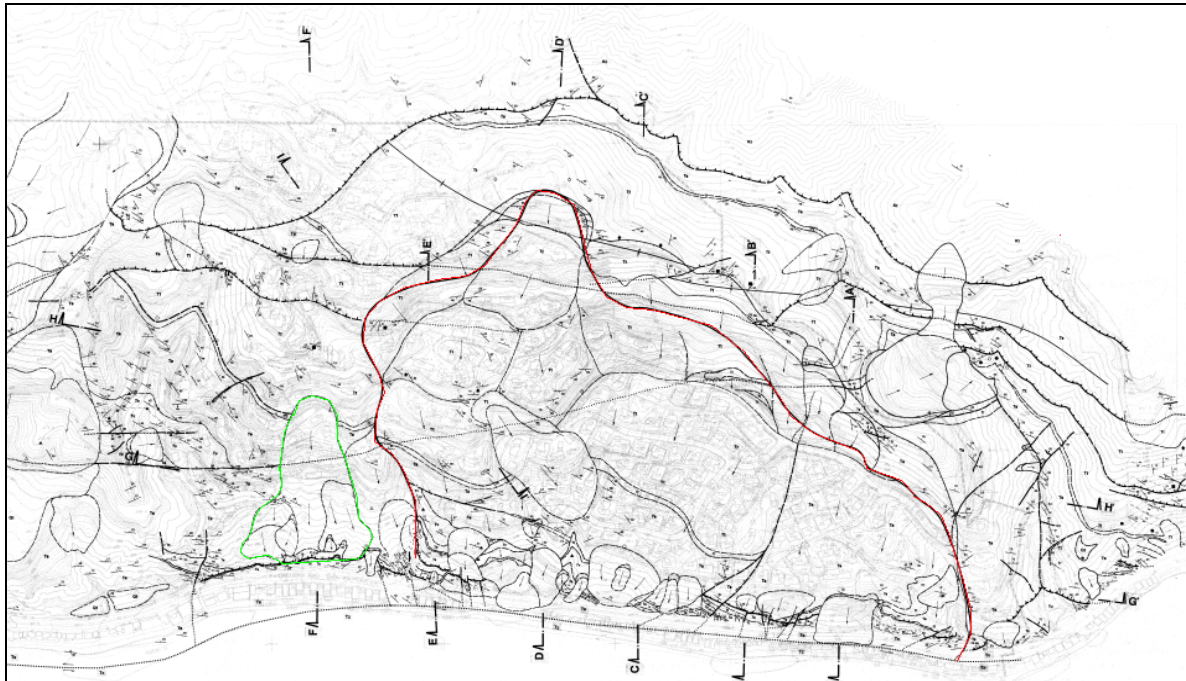


Figure 3.2 Big Rock Mesa boundary map, indicating the cross-sections (Bing Yen & associates)

3.1.2. Rock formations

From Geological investigations of the Big Rock Mesa, which were used to make the geological maps and cross-sections in Appendices 1 to 12, the following rock formations are found:

- ♦ **Tt_Topanga canyon formation (middle Miocene) Sedimentary rock (Appendices 1-12)**
Marine sandstone; pebbly sandstone, siltstone and shale(saddle peak member).
- ♦ **Ts_Sespe formation (upper Eocene to lower Miocene) Sedimentary rock (Appendices 1-12)**
Terrestrial redbed sequence of sandstone, pebbly sandstone, conglomerate and siltstone.
- ♦ **Tv_Vaqueros formation (lower Miocene) Sedimentary rock (Appendices 1-12)**
Marine siltstone, sandstone and shale.
- ♦ **Tz_Zuma volcalics (lower to middle Miocene) Igneous rock (Appendices 1-12)**
Basaltic and andestic breccia flows, tuff and volcanoclastic sediment.
- ♦ **Ti_Conejo volcanics-intrusive rocks (middle Miocene) Igneous rock (Appendices 1-12)**
Diabase, basalt and porphyritic basalt; dikes and sills of a few meters thick cutting all other units.
- ♦ **Tc_Coal canyon formation (lower Paleocene and Eocene) Sedimentary rock (Appendices 1-12)**
Marine shale, conglomerate and sandstone.
- ♦ **Kt_Tuna canyon formation (upper Cretaceous) Sedimentary rock (Appendices 1-12)**
Marine shale, sandstone and cobble conglomerate.

In Figure 3.3 a diagrammatic representation of geological time is presented which is used to place the rock formations in the geological time frame. The Topanga, Zuma, Conejo and Vaqueros formations were formed in the middle and lower Miocene. The Miocene period lasted from 5.3 till 23.8 million years ago.

The Sespe formation was formed in the upper Eocene to lower Miocene. The lower Miocene period to Eocene period was around 23.8 until 54.8 million years ago. The Coal canyon formation was formed in lower Paleocene and Eocene period. The Paleocene period was from 54.8 until 65 million years ago and the Eocene period was from 23.8 until 54.8 million years ago. The Tuna canyon formation was formed in the upper Cretaceous. The Cretaceous period was from 65 until 144 million years ago.

Era	Period	Epoch	Duration in millions of years	Millions of years ago
CENOZOIC	Quaternary	Holocene	0.01	0.01
		Pleistocene	1.8	1.8
	Tertiary	Pliocene	3.5	5.3
		Miocene	18.5	23.8
		Oligocene	9.9	33.7
		Eocene	21.1	54.8
		Paleocene	10.2	65
MESOZOIC	Cretaceous		79	144
	Jurassic		62	206
	Triassic		42	248
PALEOZOIC	Permian		42	290
	Carboniferous	Pennsylvanian	33	323
		Mississippian	31	354
	Devonian		63	417
	Silurian		26	443
	Ordovician		47	490
	Cambrian		53	543
PRECAMBRIAN				

Figure 3.3 The standard geological column. (Hamblin, W.K., Christiansen, E.H)

Sedimentary rock

Sandstone and siltstone are sedimentary stones. The formations of these rocks begin with the deposit of sediments. The chemical, physical and biological change of sediment after deposition is called diagenesis. Lithification takes place under rising pressure due to continuous depositing which builds up an over burden. This causes the underlying sediments to compact. Minerals in the groundwater can precipitated and reduce the pore space by cementation.

Igneous rock

Basalt is an igneous rock and is formed from magma. Magma is molten rock and consists of liquid, gas and crystals. Basalt is an aphanitic textured rock. Aphanitic texture results from relative rapid cooling of the magma. The crystals are very small in this type of rock because they need a much slower cooling process to grow. Basalt is very-fine grained and usually dark coloured. However, voids in the basalt can occur due to trapped gas bubbles.

3.1.3. Ancient movement of the BRM landslide

The most part of the BRM Landslide consists of the Topanga canyon and Sespe formation. Conejo volcanics-intrusive rocks at several levels intruded these formations. At the lower part of the BRM slide, where the slide ends at the ocean, Zuma volcanic rock is present. Those volcanic intrusive rocks layers are an indicator for the amount of movement of the slide; see Figure 3.4.

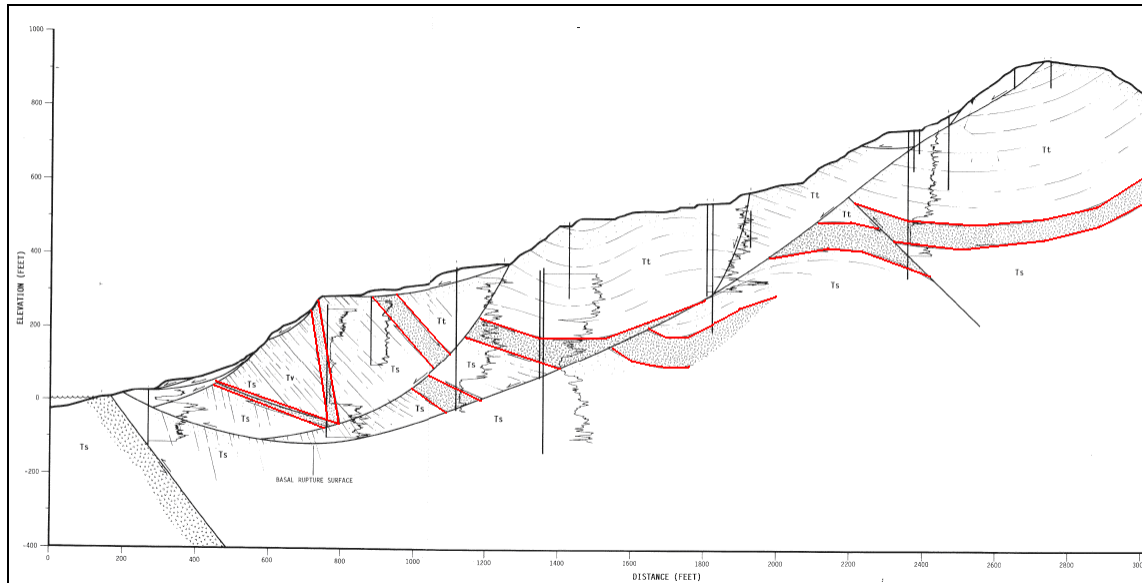


Figure 3.4 Volcanic layers, shaded layers (Bing Yen & associates, 1991) (The vertical lines indicate wells and inclinometer casings)

In 1984 the measurement of slope movement started. From those measurements it can be concluded that the BRM slide only moved a few centimetres in total since the first measurements. Compared to the volcanic rock layers it can be assumed that the movement has been going on long before the measurements started. From geological studies it has been estimated that movement started about 4000 years ago.

From the Geological map in Appendix 1 and the cross sections A to I in Appendices 4 to 12 the following can be observed:

- There are several smaller slides within the large slide.
- There is also upward movement of about 640 m (2100 ft) from the ocean in the upper region of the slide. This is visible in cross section D-D' and cross section E-E'
- At the lower part of the BRM slide, where the Zuma formation begins, upward movement is active over the entire length of the slide. This is visible in cross sections A, B, C, D and F.

As mentioned earlier, earthquakes probably initiated the landslide. Tectonic movement causes rock bodies to move along a fault line, which results in earthquakes. An overview of the faults in the Los Angeles area is presented in Figure 3.5. The green and red lines indicate the thrusts and faults. Each fault has been given a name, which corresponds with a number. The names of the faults are listed below Figure 3.5. In this figure, the green point indicates the location of the Big Rock Mesa. In the BRM area the Malibu coast fault is present. The large San Andreas fault is located about 100 km from Malibu. These faults, caused by tectonic movement, make the Big Rock Mesa area prone to earthquakes. In Chapter 3.3 the earthquake activity in this area is further evaluated.

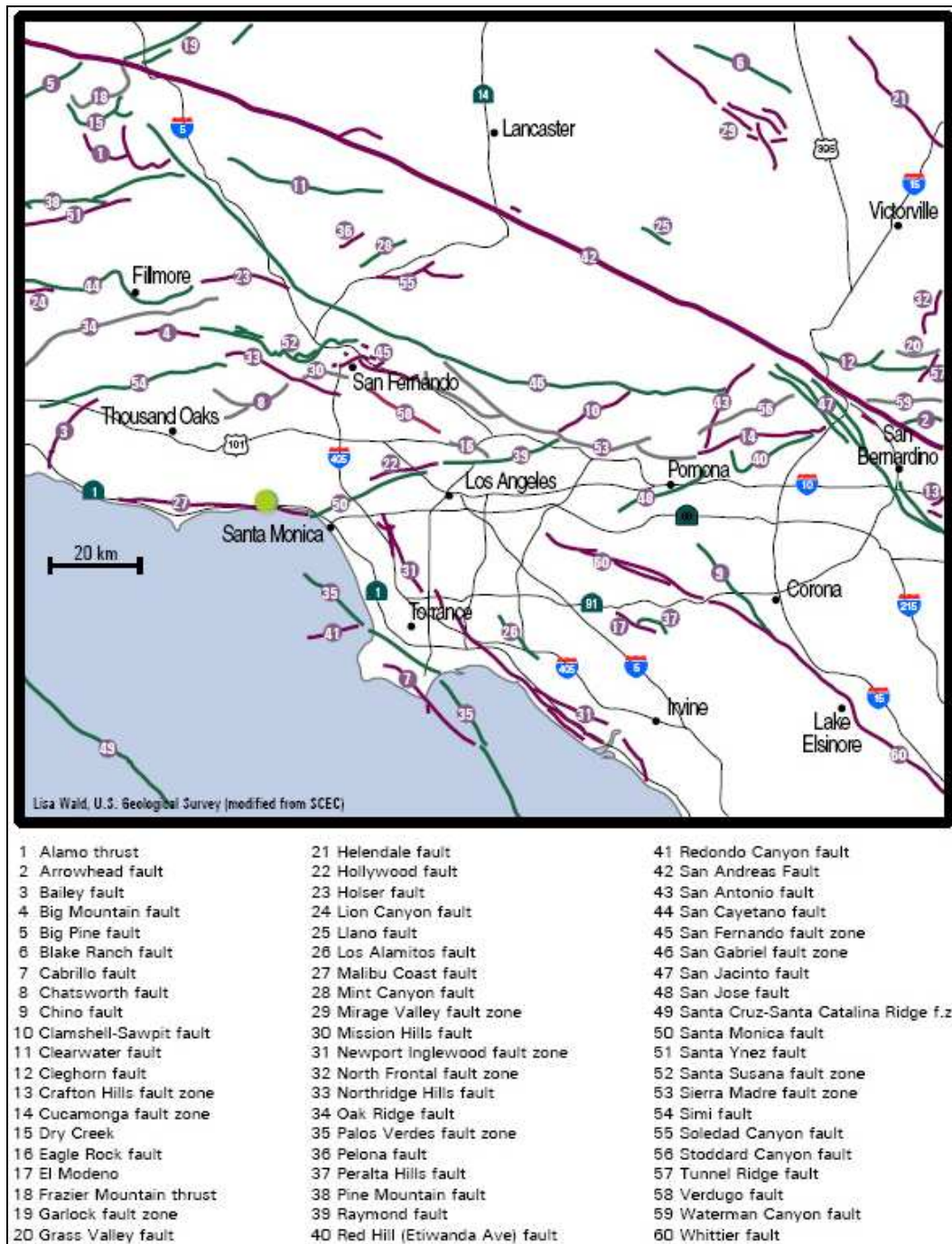


Figure 3.5 Los Angeles county fault map (Lisa Wald, U.S. Geological Survey, modified from SCEC, USGS)

3.1.4. Current movement of the BRM landslide

After significant movement of the BRM landslide in the period of 1978-1984, the assessment of its movement was started in 1984. Bulges in roads and other visual signs of movement were noticed in the period 1978-1984.

The movement of the landslide in that period coincided with heavy “El Nino” storms, successive wet years, lack of maintenance of the dewatering systems, building of new houses (with onsite waste disposal units) and the dismantling of a large production well. When the problem became evident, the installation of new wells and hydraugers (horizontal drains) was started. An overview of the inclinometer data from 1983 until 2009 (in monitoring years from July to June) is presented in Appendix 13. In the period 1983-1984 the largest displacement was registered (up to 21 cm). After that year, with a more advanced dewatering system installed, the annual displacement slowed down.

From the data in Appendix 13 it follows that, besides 1983-1984, within the periods 1992-1993, 1994 to 1998, and 2004-2005 the average displacement was large compared with the other periods. In the period 2004-2005 the movement of the landslide was massive, because many of the inclinometers (15 out of 24) registered a displacement; see Figure 3.8. The movement in the Headscarp region is the largest. The only inclinometer reading in this area (SP26) suggests that the smaller sub-slide within the larger slide is moving.

The annual total rainfall is plotted along with the annual average displacement in Figure 3.6. The daily rainfall was recorded by a station in Santa Monica, which is located at about 10 km from the Big Rock mesa (University of California; Agriculture and natural resources.); see Figure 3.9. The annual average displacement was determined from a series of inclinometer measurements. The maximum annual displacement measured is presented in Figure 3.7. Since this displacement originates from a single inclinometer recording it relates to a local displacement. For example, the difference between the average displacement and the maximum displacement is in the range of a factor of 10 to 20. These local displacements hint at smaller sub-slides.

In the periods 1993-1994, 1999-2000, 2000 to 2004 and 2006-2007 no movement has been registered. These periods correspond with relatively dryer years. The annual rainfall was exceptionally high in the periods 1992-1993 and 2004-2005, and daily rainfall peaks were registered in the periods 1994-1995 and 1997-1998 as displayed in Figure 3.6 and 3.9. In each of those periods displacements were measured. The displacement in 2000-2001 corresponds with relatively high rainfall for that period.

However, in the periods 1995-1996, 1996-1997 and 1998-1999 neither high annual rainfall nor exceptionally high daily rainfall peaks were measured. At the places where movement was measured, changes in the hydraulic system may have occurred. Unfortunately, this is very difficult to determine due to the complexity of the hydraulic system.

Thus significant local and overall displacement occurred during years with either high annual rainfall or high daily rainfall peaks. However, the influence of the rainfall on the movement of the landslide is complex due to the large scale of the landslide and dewatering system. In Chapter 3.2 the hydraulic system, which include the rainfall, groundwater elevation and dewatering system, will be discussed.

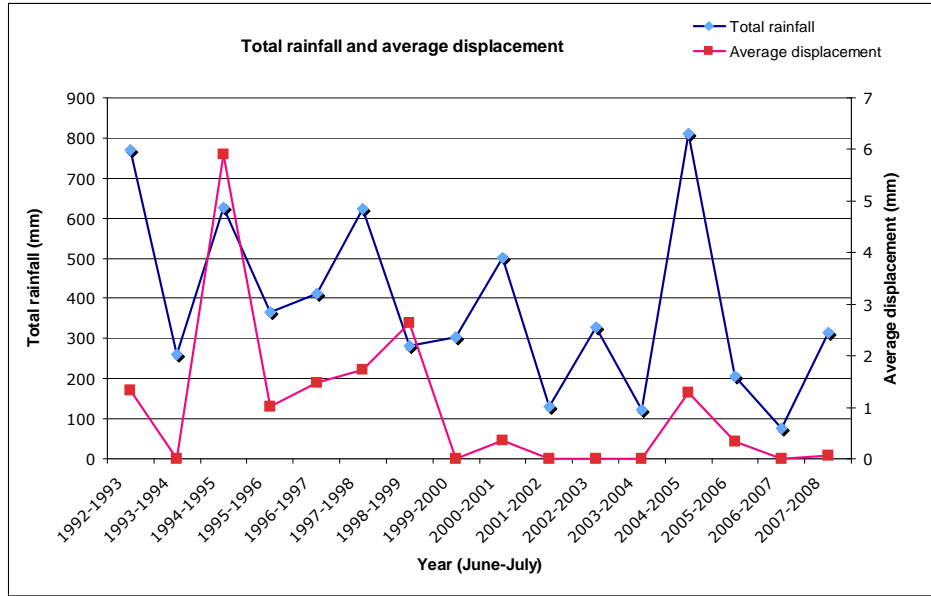


Figure 3.6 Total rainfall and average displacement

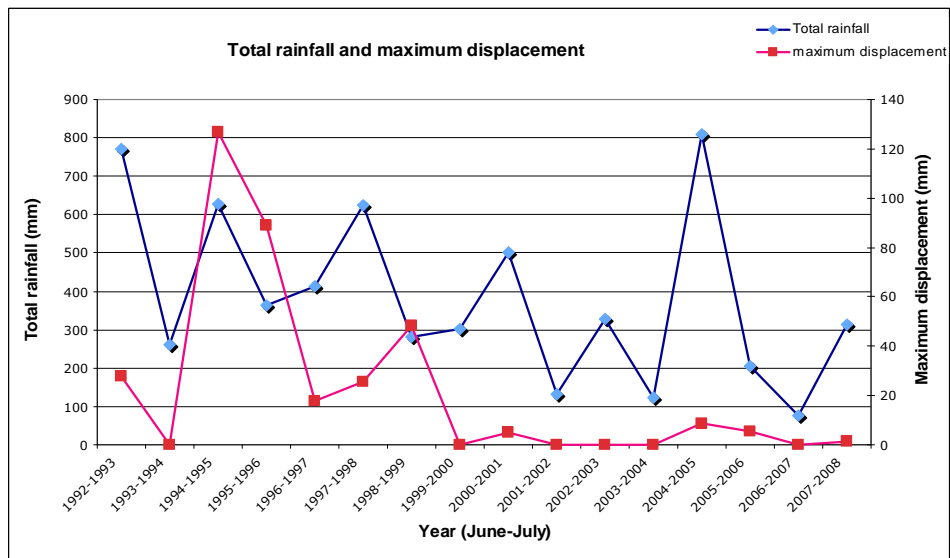


Figure 3.7 Total rainfall and maximum displacement

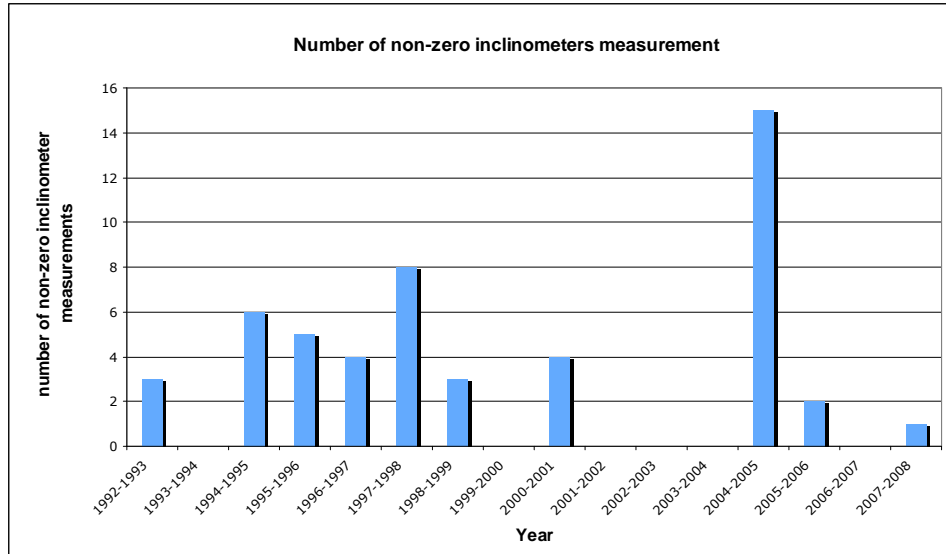


Figure 3.8 Number of non-zero inclinometer measurements (from the 24 inclinometers)

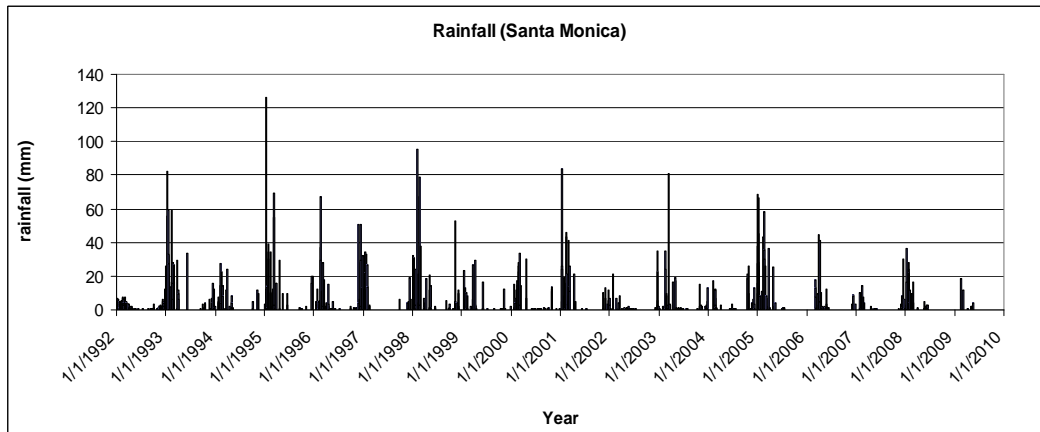


Figure 3.9 Daily rainfall records (University of California; Agriculture and natural resources.)

3.2. Hydraulics

The evaluation of hydraulic data presented in this Section includes precipitation data, groundwater levels and dewatering rates.

3.2.1. Rainfall data

During a year, the amount of rainfall changes with the seasons. The most rainfall happens in the winter, especially in the months, January, February and March. In the summer rainfall is very rare. The amount of rainfall also strongly differs per year, which can be derived from Figure 3.10 a, where the annual rainfall at Santa Monica (10 km from BRM) is displayed from 1992 to 2009.

The rainfall that actually contributes to the groundwater elevation is the effective rainfall, which consists of the factual rainfall minus the evapotranspiration. The evapotranspiration is mainly dependent on temperature. When the temperature is high the evapotranspiration is equally high, which means that the evapotranspiration is highest in the summer and lowest in the winter. In Figure 3.10 b the evapotranspiration at Santa Monica is determined by: The California Irrigation Management Information System (CIMIS). The values have been determined with the method described in Chapter 2. Note that this method uses an irrigated grass surface as reference, i.e. in case the actual surface is not irrigated the estimated evapotranspiration will be too high. This is usually applied to the surface of slides considered in this work. The effective rainfall in Santa Monica is shown in Figure 3.10 c. From this graph it can be concluded that the evapotranspiration has little influence during the winter months when the rainfall dominates. The accumulated rainfall is illustrated in Figure 3.10 d.

Other influences on the hydraulic system are human constructions and fires. Of the houses that have been constructed on the BRM most have on-site waste disposal tanks. These tanks treat the waste water from the household and pump it into the groundwater. Thus these tanks contribute to the water infiltrating the Landslide.

Fire on the other hand destroys the vegetation, which causes a decrease in evapotranspiration. However, when in 1993 a fire destroyed most of the properties on the BRM, the amount of water infiltrating the landslide decreased because of the lower number of active waste disposal tanks.

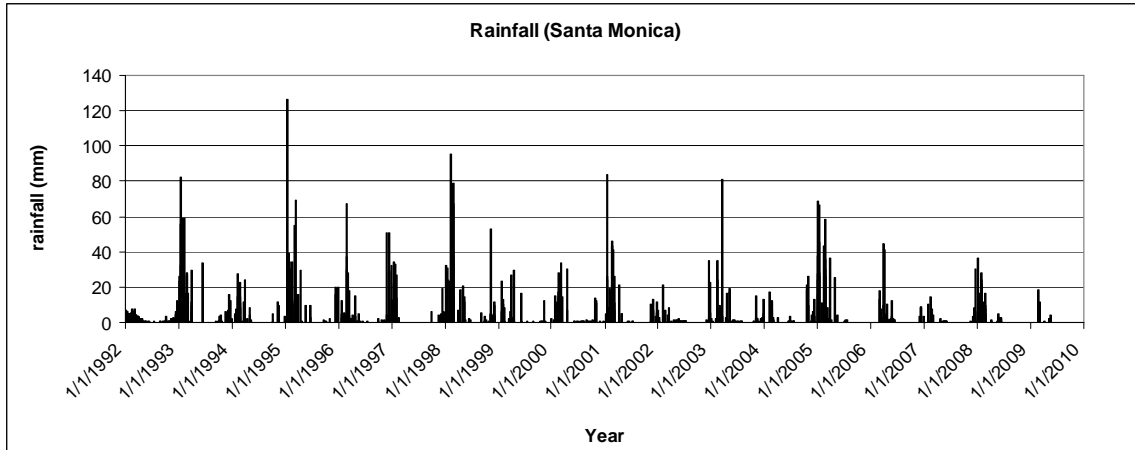


Figure 3.10 a Daily rainfall records (University of California; Agriculture and natural resources.)

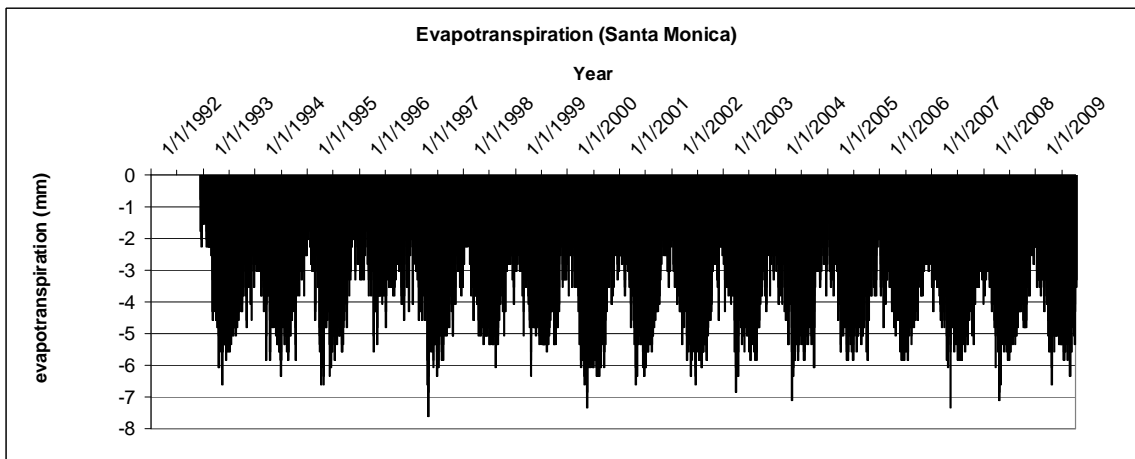


Figure 3.10 b Daily evapotranspiration records (University of California; Agriculture and natural resources.)

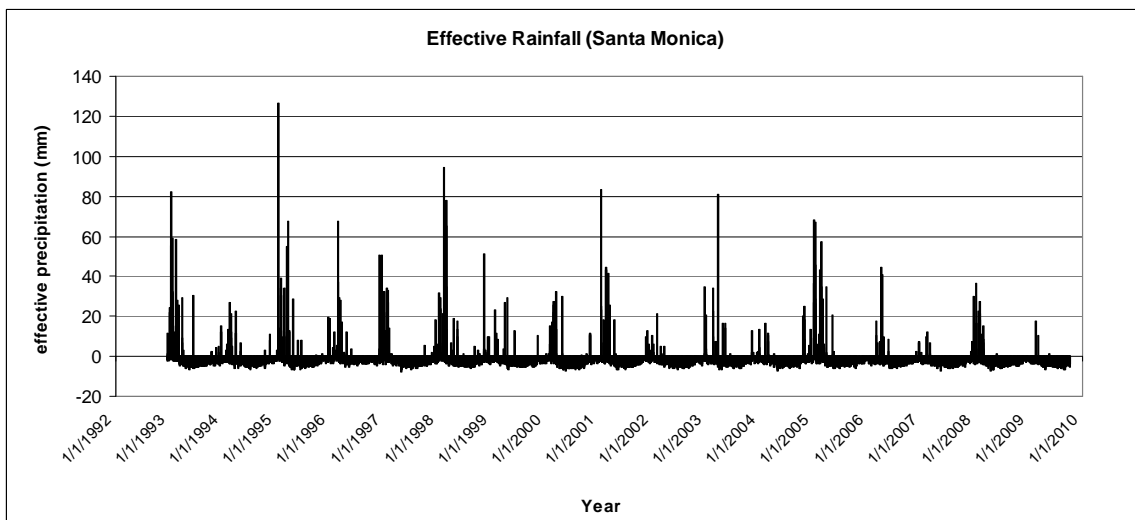


Figure 3.10 c Daily effective rainfall records

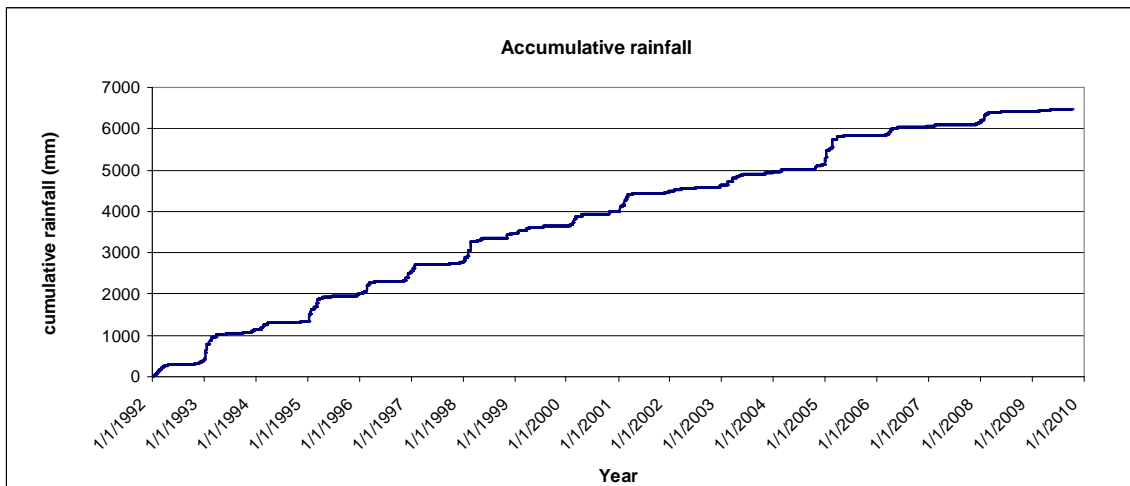


Figure 3.10 d Cumulated rainfall

3.2.2. Groundwater levels

The groundwater elevation varies due to water infiltrating and exiting the hydraulic system. The Normalized groundwater elevation is displayed in Figure 3.11. From this graph the following can be observed:

- Before 1995-1996 large variations were measured in especially the Central and Eastern section. Apparently, a more elaborate dewatering system contributed to stabilizing the groundwater levels.
- The distinguishing peak in 2004-2005 corresponds with the exceptional rainfall in that year.

The groundwater elevation data in Figure 3.11 is based on monthly readings. For the months with dominating rainfall it could be that monthly readings are not sufficient to establish the varying elevations. This is because of the dissipation of groundwater in time after storms.

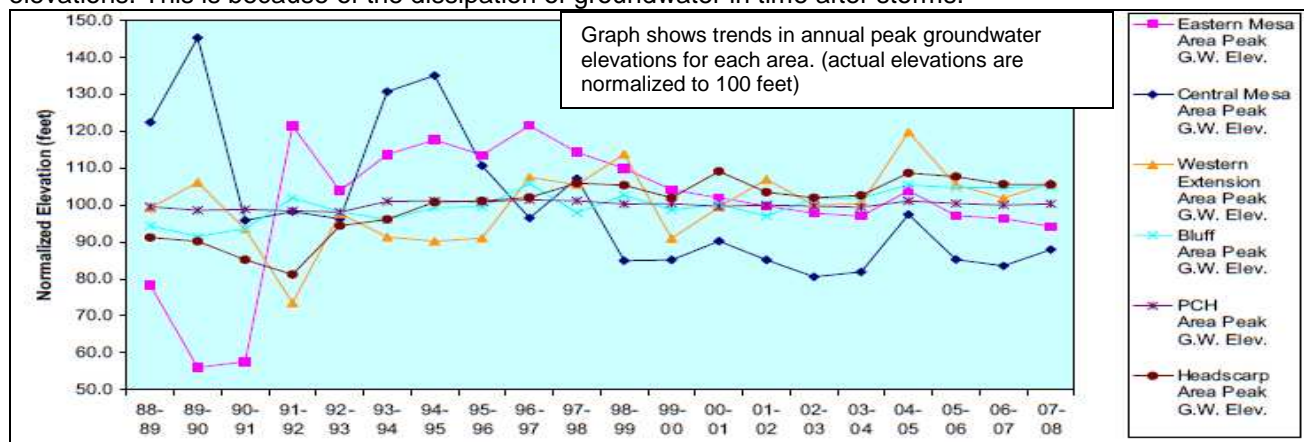


Figure 3.11 Normalized groundwater elevations (in feet) (Report Fugro West Inc. 2008)

3.2.3. Dewatering

The dewatering system installed in the BRM landslide consists of hydraugers (horizontal drains) and wells. These have been installed in order to minimize the water infiltrating the landslide and to keep the groundwater levels stable. By keeping the groundwater level stable, the movement of the landslide due to increasing pore pressures is minimized. When reviewing the slope inclinometer data in Appendix 13 it can be seen that in 1983-1984 a displacement up to 21 cm was measured. After that observation, dewatering equipment was installed and the movement decreased since then.

The production of the hydraugers and wells are presented in Figure 3.12 a and 3.12 b, respectively. Unfortunately, there are some gaps in the data. However, this doesn't mean that they were not active in those periods. There are distinguishing peaks in production in 1989, 1995, 1998-1999 and 2004-2005; see Figures 3.12 a and 3.12 b. This corresponds with the periods in which large amounts of rainfall were measured. It must be noted that the production of the dewatering system is also influenced by the installation and deterioration of drains and wells. Failure of hydraugers or wells could also have led to the local displacement of the slide.

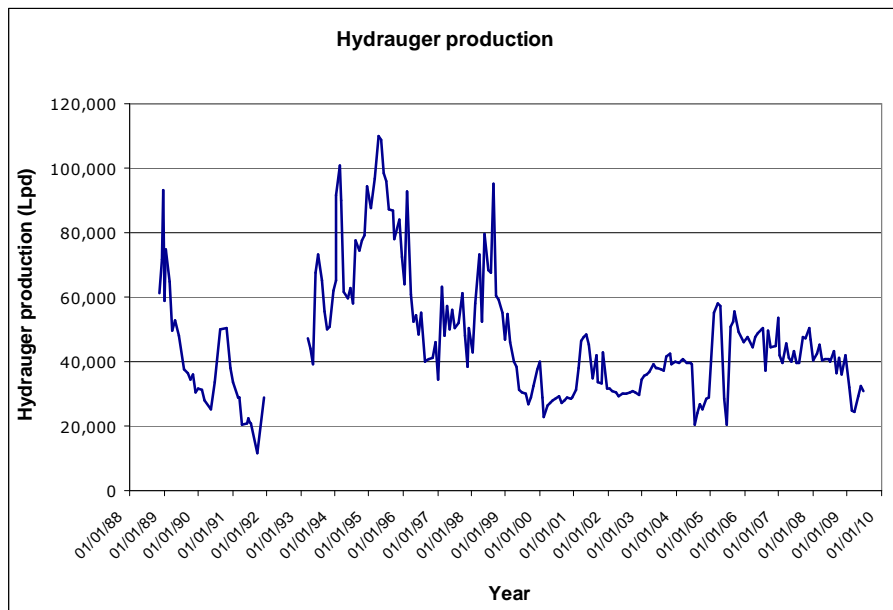


Figure 3.12 a Hydrauger production (Fugro West Inc.)

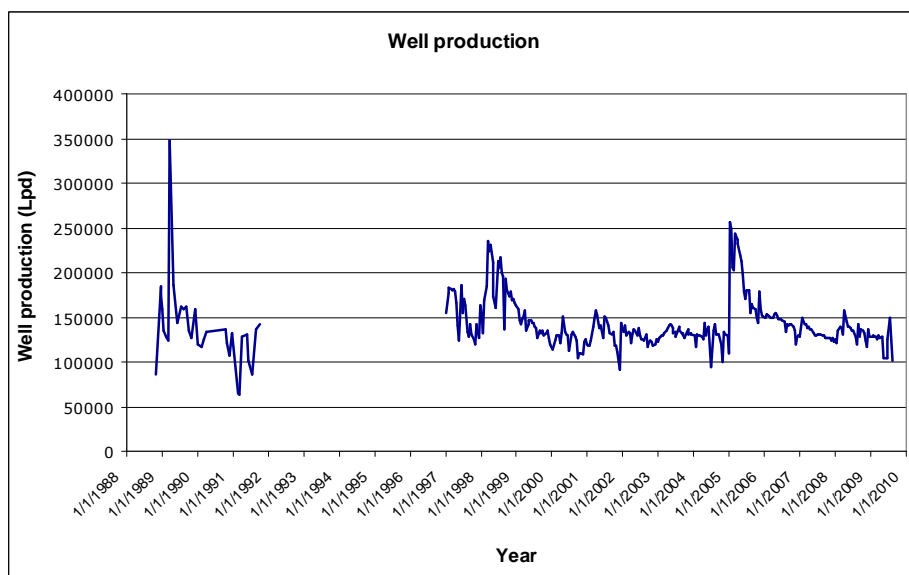


Figure 3.12 b Well production (Fugro West Inc.)

3.3. Earthquakes

Daily earthquakes were registered in Southern California; see Figure 3.13 for the graph of Southern California boundaries. Most of those earthquakes are in the range of 1 to 3 on the Richter scale. This corresponds with a horizontal acceleration of 0.01 to 0.05 m/s^2 , which is about a few tenths of a percent of normal gravitation (California Institute of Technology; earthquake catalog). These vibrations are feeble and hardly felt by humans. In Table 3.1 the frequency of reoccurrence of higher magnitude earthquakes in Southern California for the period 1980-2009 is presented.



Figure 3.13 Southern California boundaries, earthquake investigation area (<http://itouchmap.com/latlong.html>)

Richter scale	Occurrence
4	647
5	65
6	6
7	2
8	0

Table 3.1 reoccurrence of earthquakes with a Richter scale higher than 4. (Source: California Institute of Technology earthquake catalogue)

The faults close to the BRM have only initiated two quakes in the period from 1980 to 2009, both around 2 on the Richter scale. The destruction and thus the initiation of a landslide increase with the Richter scale number. Therefore, this aspect must be included when modelling the stability of a landslide. In Table 3.2 the Richter scale and Mercalli scales are listed with the corresponding acceleration speeds and description of the consequences. The Mercalli scale is an arbitrary set of descriptions based on what people feel and their observations of damage. In Table 3.2 the relation between the Richter scale, Mercalli scale and the acceleration speed is given.

Richter	Mercalli	Acceleration m/s²	Description
<3.5	I	0.01	Instrumental
3.5	II	0.025	Feeble
4.2	III	0.025	Slight
4.5	IV	0.1	Moderate
4.8	V	0.25	Rather strong
5.4	VI	0.5	Strong
6.1	VII	1	Very strong
6.5	VIII	2.5	Destructive
6.9	IX	2.5	Ruinous
7.3	X	5	Disasterous
8.1	XI	7.5	Very Disasterous
>8.1	XII	9.8	Catastopic

Table 3.2 Relation between the Richter scale, Mercalli scale and the acceleration speed (<http://www.geography-site.co.uk/pages/physical/earth/richt.html>)

In this study the infiltration of rainwater plays a vital role. In sequel the influence of earthquakes are excluded, although earthquakes may have some effects, particularly in the region of the BRM, where many faults are present.

4 Unsaturated zone behaviour

The unsaturated zone describes the transition from saturated to dry soil. This transition involves the interaction between the gas, liquid and solid phases. The influence of the unsaturated zone on the strength parameters of soil can be significant. In particular the influence of suction in the soil has influence on the effective stress.

In this Chapter the water content, wetting and drying cycles, soil suction and their influence on the deformation behaviour of slopes will be evaluated.

4.1. Defining the unsaturated zone

The geo-hydrology of the sub surface can be divided in three zones: (i) the dry zone, where only gas (air) and grains are present, (ii) the saturated zone, where only liquid (water) and grains are present, and (iii) the transition zone. The transition zone is in between the dry and saturated zone and denoted as the unsaturated zone in which gas, liquid and grains are present.

The distribution of water and air in the unsaturated zone differs with the degree of saturation. Where the degree of saturation is low, air will be continuous through the soil skeleton. Where the degree of saturation is high, water is continuous. The degree of saturation S over which both water and air are continuous varies typically between 0.25 to about 0.85 and this situation is most common in practice (Atkinson, 1993).

In the zone where air is continuous, water is bound to the soil grains by surface forces. At points of contact water bridges are formed. For bridges to form a minimum degree of saturation is necessary.

4.1.1. Water content

The water content in the unsaturated zone can be described by a soil-water retention curve. The soil-water retention curve was described by van Genuchten, 1980 based on Mualem's model, 1976. This curve plots the water content from the saturated volumetric water content θ_s to the residual water content θ_r . The water content for each pressure head of the curve can be calculated with:

$$\theta = \theta_r + \frac{(\theta_s - \theta_r)}{\left[1 + (g_a |\phi|)^{g_n}\right]^{g_m}} \quad [4.1]$$

where ϕ is the pressure head and g_a , g_n and g_m are empirical parameters. A typical soil-water retention curve is presented in Figure 4.1. For this curve determines the g_a 'start' position, g_n and g_m determine the steepness of the slope, but the influence of m on the steepness is less than that of g_n .

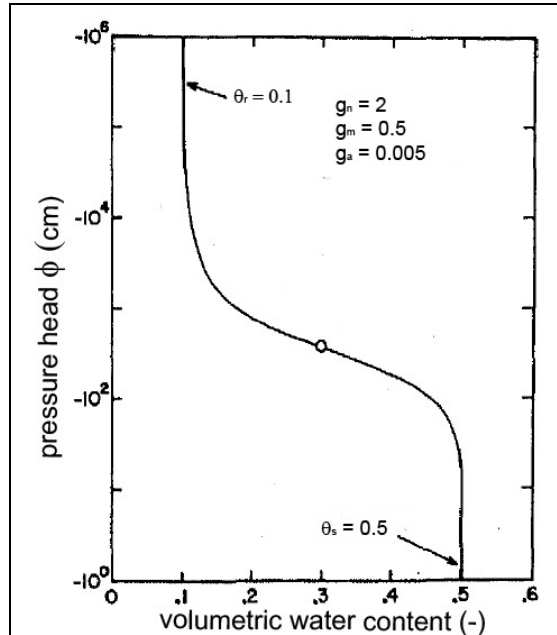


Figure 4.1 Typical plot of the soil-water retention curve based on Eq. [4.1] (van Genuchten, 1980).

The residual water content is defined here as the water content θ_r for which the gradient $\left(\frac{d\theta}{dh}\right)$ becomes zero (excluding the region near θ_s which also has a zero gradient) (van Genuchten, 1980). Therefore, the soil-water retention curve does not include water content in the range between θ_r and zero.

The empirical shape parameters that construct the retention curve vary with soil type. Soils with a higher permeability such as sand have a shorter curve than soils with a low permeability such as clay. A characteristic curve (water content versus pressure head) is presented in Figure 4.2 for sand, fine sand and silts. From this curve it is apparent that materials with smaller pore sizes (such as silt) tend towards larger pore suction at given water content. At very low pressures the water content becomes almost constant. This because the water forms a thin film that is tightly bound by forces of attraction between water molecules and the mineral surfaces (Fitts, 2002).

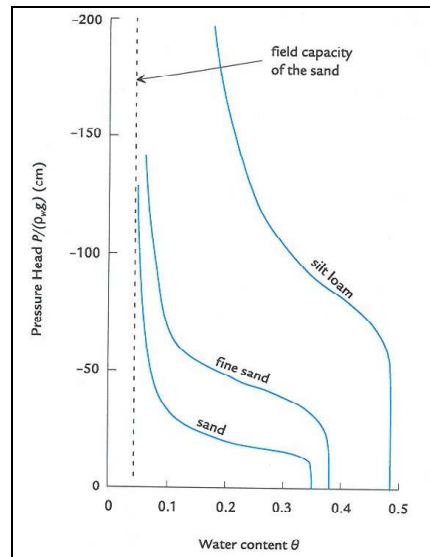


Figure 4.2 Water content vs pressure head (Fitts, 2002)

For the analysis of the BRM the van Genuchten parameters are used to determine the saturation level in the unsaturated zone. In Table 4.1 the van Genuchten parameters used in the calculation are listed along with a reference to the origin of those values (Databases USDA and Hypres are compiled by Plaxis and Deltares).

Formation	θ_r (-)	θ_s (-)	g_a	g_m	g_n	Source	Comment
Sandstone	0.15	0.25	0.79	0.9	10.4	v.Genuchten (1980)	Hygiene sandstone
Landslide debris	0.045	0.43	14.5	0.5	2.7	Plaxis Manual	Sand Database: USDA
Basalt	0.010	0.77	1.3	0.4	1.2	Plaxis Manual	Very fine Database: Hypres
Siltstone	0.034	0.46	2.0	0.5	1.4	Plaxis Manual	Silt Database: USDA
Shear zone	0.045	0.43	14.5	0.5	2.7	Plaxis Manual	Sand Database: USDA

Table 4.1 van Genuchten parameters

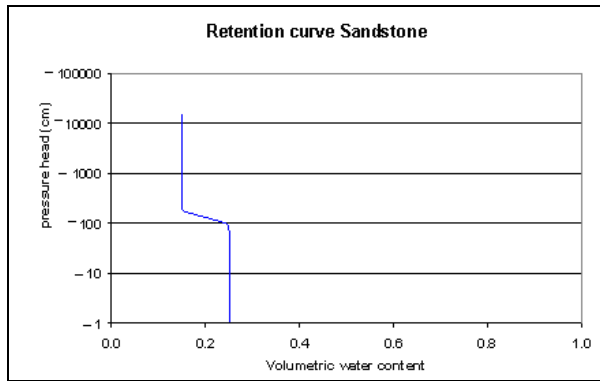


Figure 4.3 a Retention curve Sandstone

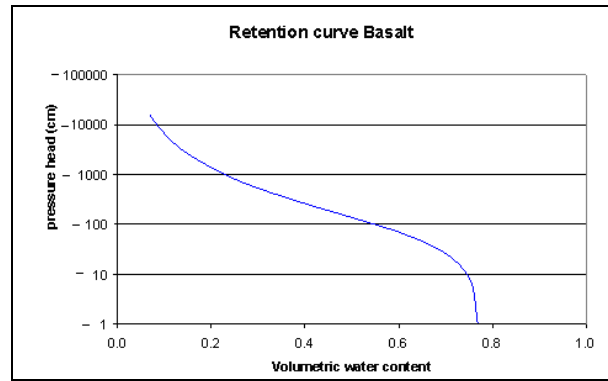


Figure 4.3 c Retention curve Basalt

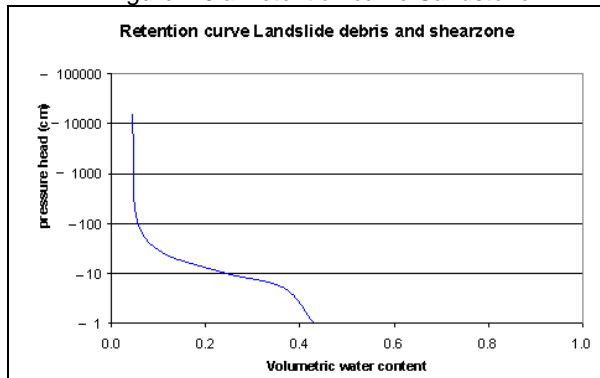


Figure 4.3 b Retention curve Landslide debris and shear zone

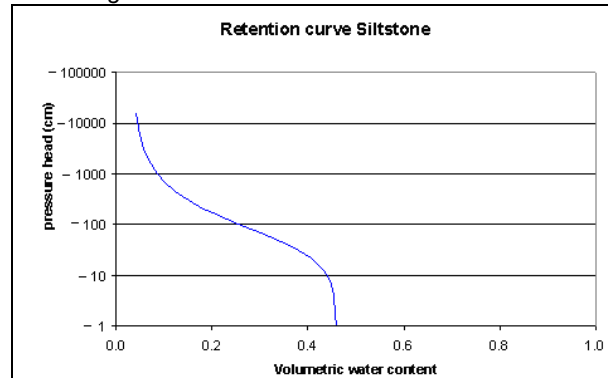


Figure 4.3 d Retention curve Siltstone

The retention curve of sandstone is the steepest followed by the landslide debris and shear zone. In correlation with Figure 4.2, the finer materials as (Siltstone and Basalt) have shallower curves.

Relative permeability

The infiltration is dependent on the relative permeability. Because the tension force bounds the water to the particles the pore space is not fully used for flow. Therefore, decreasing the potential permeability to a relative permeability, which decreases with increasing suction. At the ground surface the highest suction force can be found and has thus the lowest relative permeability.

The relative permeability can be given by:

$$k_{rel}(S) = (S_e)^{g_l} \left[1 - \left(1 - S_e^{\frac{g_n}{g_n-1}} \right)^{\frac{g_n-1}{g_n}} \right]^2 \quad [4.2]$$

where g_l is an empirical parameter and S_e is the effective saturation, which is defined by:

$$S_e = \frac{S - S_r}{S_s - S_r} \quad [4.3]$$

S_r and S_s are the residual and fully saturated soil ($S_s=1$) level, respectively. S_s occurs when θ_s is reached. S_r relates to the water content by:

$$S_r = \frac{\theta_r}{\theta_s} \quad [4.4]$$

The permeability follows from:

$$k = k_{rel} \cdot k_{sat} \quad [4.5]$$

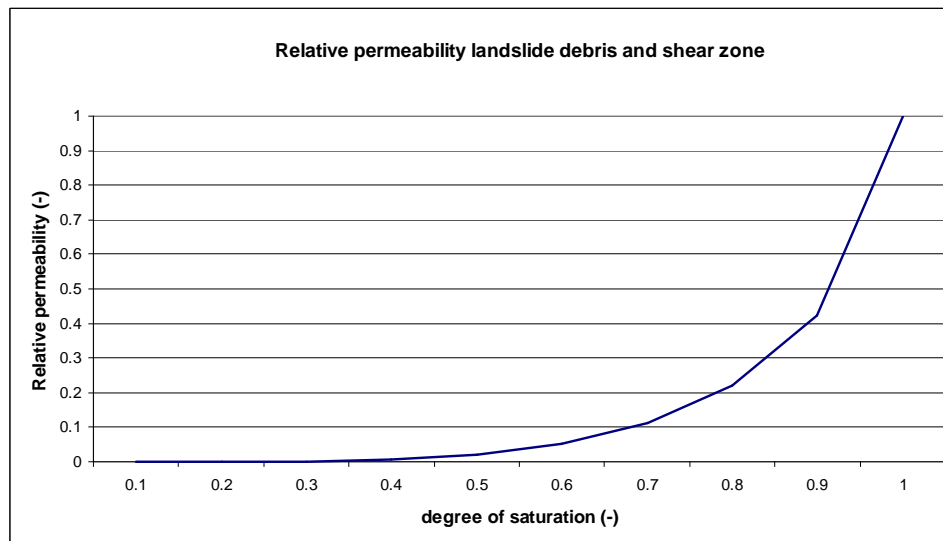


Figure 4.4 Relative permeability as a function of the saturation for Landslide debris and shear zone.

4.2. Soil suction

The water pore pressure is in the unsaturated zone less than the atmospheric pressure due to the tension in the water as it is attracted to and 'stretched' over the mineral surface (Fitts, 2002). This creates an 'under pressure' and thus suction ($u_a - u_w$); known as matric suction. The surface tension T_s of water between two particles is illustrated in Figure 4.5.

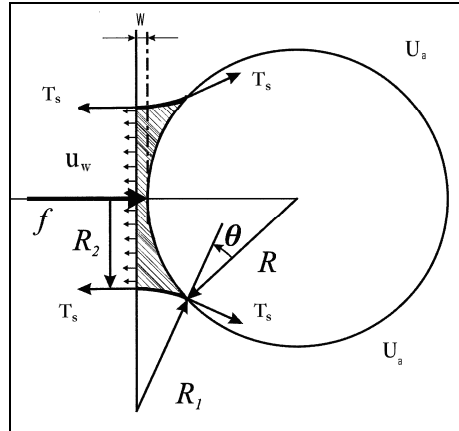


Figure 4.5 Water bridge between two particles (Molenkamp, 2008-2009).

The water between the grains is curved (meniscus) due to surface tension (Fredlund, 1993). The water vapour pressure above a curved water surface is less than above a flat surface. This means that the relative humidity in soil will decrease due to the presence of curved water surfaces. The radius of curvature is inversely proportional to the difference between air and water pressure. The matric suction ($u_a - u_w$) is only one component of the total suction that contributes to the reduction of relative humidity.

Most pore-water in soils contains dissolved salts. The water vapour pressure over a flat surface of solvent is less than the water vapour pressure over a flat surface of pure water. Thus increasing dissolved salts in the pore-water decreases the relative humidity. This decrease of relative humidity due to dissolved salts is called the osmotic suction

Capillary fringe

In soils, the pores with small radii act as capillary tubes that cause the soil water to rise above the water table (Fredlund, 1993). The height of the capillary fringe in soils is associated with the matric suction. The relationship between the surface tension, capillary height and water pressure is illustrated in Figure 4.6.

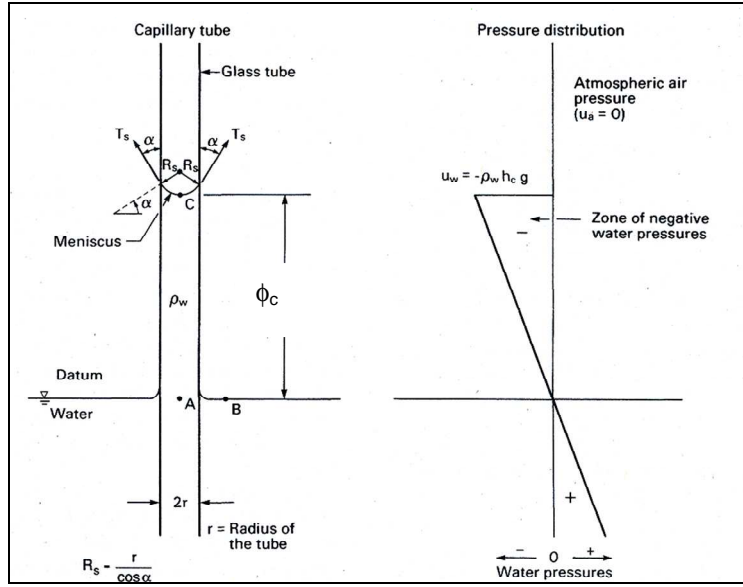


Figure 4.6 Water Capillary fringe (Fredlund, 1993)

The maximum capillary height can be determined according to:

$$\phi_c = \frac{2T_s}{\rho_w g R_s} \quad [4.6]$$

where $R_s = \frac{r}{\cos \alpha}$

The matric suction written in terms of surface tension equals:

$$(u_a - u_w) = \frac{2T_s}{R_s} \quad [4.7]$$

The surface tension is thus able to support a water column with a height of ϕ_c . The role of the radius of the capillary tube (pore space) is important. If R_s increases, the ϕ_c decrease and visa versa. Thus the capillary height and also the matric suction increases with decreasing pore size.

4.2.1. Calculation method for soil suction

The suction in the soil has also an effect on its effective stress. If there is a large suction force, the soil will behave more cohesively and add to the strength. The Bishop's equation (1963) is commonly used to determine the effective stress in the unsaturated zone:

$$\sigma' = \sigma - u_a + \chi(u_a - u_w) \quad [4.8]$$

where:

χ = suction coefficient; $\chi=1$ for fully saturated soil and $\chi=0$ for dry soil ($\sigma' = \sigma$)

$(\sigma - u_a)$ = net normal stress

The term $(u_a - u_w)$ represents a pressure difference due to surface tension acting in general over only a part of the surface area of the soil particle (Bishop and Blight, 1963). It is also referred to as the matric suction term and a change in value is accompanied by a significant change in the value of χ . In Figure 4.7, the χ value against the degree of saturation is presented for different soil types. For a Moraine type of soil the suction coefficient is in excess of the degree of saturation over a wide range. However, for a Boulder clay a transient behaviour occurs, i.e. for high degrees of saturation the suction coefficient is in excess and for low degrees of saturation it is smaller than the degree of saturation. In the other cases (3 and 4) the limited data suggest that the suction coefficient is mainly smaller than the degree of saturation.

In the unsaturated zone there is less water than in the saturated flow. In unsaturated zone the water is often present in the form of attached water (to particles) and water bridges. These phenomena cause a stagnated flow in the unsaturated zone.

It is important to note that when the soil dilates due to shearing the suction increases. Similar as for the water content curves, the value for χ differs per soil type.

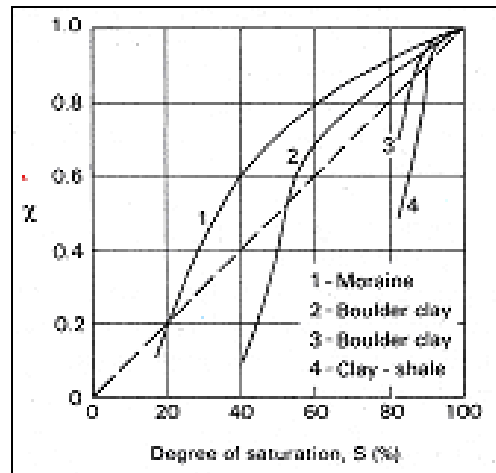


Figure 4.7 Relation between coefficient χ and the degree of saturation for different soils (experiment done by Blight 1961, taken from Fredlund, 1993).

As mentioned in the introduction, the matric suction $(u_a - u_w)$ is only one component of the total suction. The other component is the osmotic suction, which depends on the amount of dissolved salts in the pore-water. In most cases the change in matric suction is the same as the change of the total suction. Only in the case where the salt content of the soil is altered by chemical contamination, the effect of the osmotic suction on the soil behaviour may be significant (Fredlund, 1993).

4.2.2. Matric suction profile

Seasonal change, vegetation and the depth of the water table influence the matric suction profile. Seasonal changes correlate with dry or wet conditions. In dry conditions evapotranspiration increases the suction at the surface. Wet conditions drastically decreases the suction.

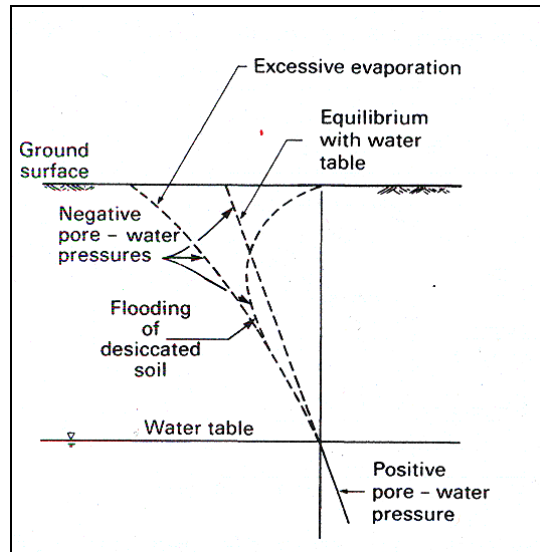


Figure 4.8 Typical pore water pressure profile (Fredlund, 1993)

Evaporation results in a net loss of water and rainfall contributes to the pore water. A typical profile fluctuation between dry and wet seasons is shown in Figure 4.8. Vegetation on the ground surface has the ability to apply a tension to the pore water of up to 1-2 MPa (100-200 meter water column) through the evapotranspiration process (Fredlund, 1993). The tension applied depends on the type of vegetation and the depth of the root zone. The water table influences the magnitude of the suction. The deeper the groundwater table the higher the suction (at the surface).

Landslides are susceptible to changes of the pore pressures. Water pore pressures have negative effects, whereas suction has a strengthening effect. Evapotranspiration increases the suction and therefore an increase in evapotranspiration leads to an increase in soil strength but also an increase of settlement. Hence, a solution for increasing the stability of a slow moving landslide is increasing the evapotranspiration. However, changing the evaporation is not possible because that is dependent on the weather. The transpiration is more viable to change. Planting more vegetation in particularly deep rooted vegetation can give a tension force to great depths.

4.2.3. Interparticle forces

Zooming in on the micro scale of the 'water bridge' connection between two particles, the resulting suction and interparticle forces is analyzed. As mentioned before, water in the unsaturated zone form the water bridge and thus create surface tension. This surface tension allows for 'under pressure' and thus suction of the water between the particles. The interparticle force following from the suction is active between the particles.

The matric suction is the difference between vapour and water pressure ($u_a - u_w$). The dimensionless expression for the suction and interparticle force is described with Eq. [4.9] and [4.10], respectively (Molenkamp and Nazemi, 2003).

$$\Lambda = \frac{sR}{T_s} = \frac{(u_a - u_w)R}{T_s} \quad [4.9]$$

$$F = \frac{f}{T_s R} = \Lambda \pi R_2^2 + 2\pi R_2 \quad [4.10]$$

where:

f = inter particle force

R = radius of particle

The relations between the dimensionless suction, dimensionless interparticle forces, water volume and dimensionless half-separation w are discussed in Molenkamp and Nazemi, 2003, see also Figure 4.5. It was found that the dimensionless suction with large initial water volume V_w increases with decreasing V_w until a maximum suction is reached. However, when V_w continuous to decrease, then the suction will decrease towards zero. The maximum suction increases with decreasing half-separation. The relating dimensionless interparticle force, F , however, reaches a maximum at an intermediate suction. With further increasing suction, F will decrease to a relative small value at maximum suction.

This phenomenon of interparticle force induced by suction is also referred to as suction induced cohesion. When analyzing the stability of soil structures additional cohesion can be assigned to the soil in the unsaturated zone.

4.3. Wetting and drying cycles

The wetting and drying cycles in relation with the matric suction and saturation is shown in Figure 4.9. From this figure it is clear that during the drying cycle the suction increases and during the wetting cycle the suction decreases. The changes in suction can result in irreversible (plastic) changes in volumetric deformations. These deformations are due to the contraction of the soil skeleton and are called: **compaction collapse**.

A decrease in suction for a certain confining stress induces swelling but can in some cases also induce a plastic volumetric deformation which may lead to slipping of soil particles. It has been found that the collapse increases with the intensity of the confining stress. An increase of suction may also lead to plastic compression of the soil skeleton. This process results into a strengthening of the soil, instead of a collapse of the soil skeleton. In Section 4.4 the collapse process during the wetting cycle is further analysed.

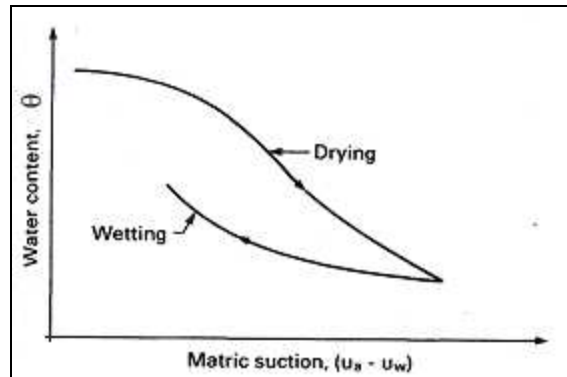


Figure 4.9 Wetting and drying in relation with matric suction (for chalk) (Fredlund, 1993).

4.3.1. Drying cycle (air intake)

In the drying cycle air has to enter the soil skeleton due to increasing suction. There are two critical suction points during this air intake. The first point is when water cavitates and bubbles are formed. In normal circumstances water cavitates at room temperature at a suction of around 100 kPa but in fine-grained soils water in very small pore spaces can sustain much larger suction without cavitation (Atkinson, 1993). The second critical suction point occurs when air is drawn into the pore space. This point depends greatly on the grain size. The condition for critical suction at which air enters is given by:

$$(u_a - u_w) > \frac{4T_s}{(V_s - 1)d_s} \quad [4.11]$$

where V_s is the specific volume derived from the total volume divided by the volume of the soil grains.

4.3.2. Wetting cycle

When it rains, the water doesn't reach the groundwater immediately. Thus, there is a delayed effect in groundwater level rise. Water from transient rainfall events tends to migrate downward and diffuse vertically as a pulse of higher water content, as shown in Figure 4.10 (Fitts, 2002). First, the soil near the surface becomes saturated and then the higher water content pulse migrates downward until it eventually adds to the groundwater level.

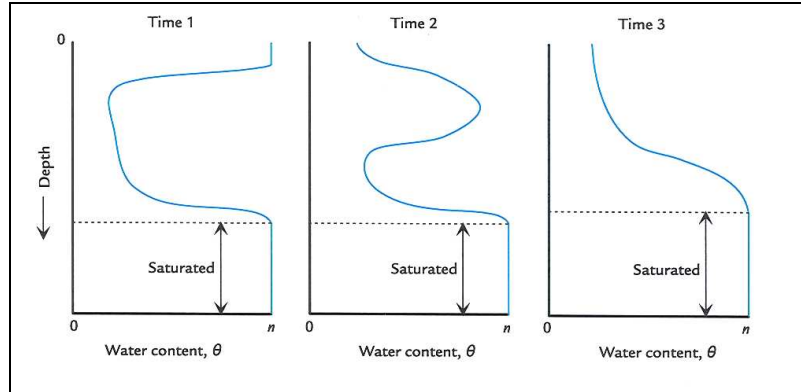


Figure 4.10 Water content after rainstorm (Fitts, 2002)

4.4. Effect of suction on deformation

In the previous sections, the influence of the unsaturated zone has been discussed in relation with the effective stress and cohesion. It has been recognized that the suction in the unsaturated zone, created by surface tension, increases the effective stress of the soil skeleton. In this Section the deformation and collapse phenomena in unsaturated soil is addressed.

There are two approaches to account for deformation and collapse. The first approach is the incorporation of net suction and matric suction into Hook's law. The second, effective stress approach is based on Bishop's effective stress.

Approach1: net stress and matric suction

The continuum requirement for unsaturated soils (when the soil particles are assumed incompressible) is formulated as:

$$\frac{\Delta V_v}{V_0} = \frac{\Delta V_w}{V_0} + \frac{\Delta V_a}{V_0} \quad [4.12]$$

The deformation of an element in the unsaturated zone is illustrated in Figure 4.11.

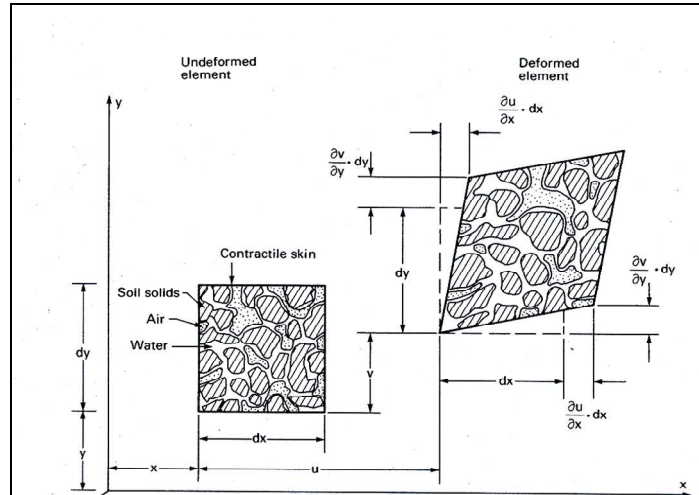


Figure 4.11 Translation and deformation of a two-dimensional element of unsaturated soil (Fredlund, 1993).

The elastic deformation of this element follows from including the matric suction and net normal stress in Hook's Law, according to Fredlund (1993):

$$\begin{aligned} d\epsilon_x &= \frac{d(\sigma_x - u_a)}{E} - \frac{\nu}{E} d(\sigma_y + \sigma_z - 2u_a) + \frac{d(u_a - u_w)}{H} \\ d\epsilon_y &= \frac{d(\sigma_y - u_a)}{E} - \frac{\nu}{E} d(\sigma_x + \sigma_z - 2u_a) + \frac{d(u_a - u_w)}{H} \\ d\epsilon_z &= \frac{d(\sigma_z - u_a)}{E} - \frac{\nu}{E} d(\sigma_x + \sigma_y - 2u_a) + \frac{d(u_a - u_w)}{H} \end{aligned} \quad [4.13,a,b,c]$$

And the total elastic deformation follows from:

$$d\epsilon_v = d\epsilon_x + d\epsilon_y + d\epsilon_z \quad [4.14]$$

$$dV_v = d\epsilon_v \cdot V_0 \quad [4.15]$$

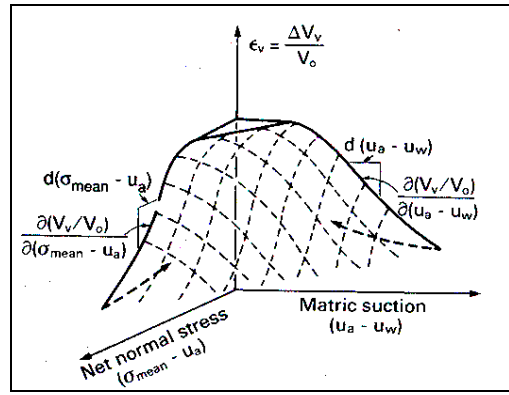


Figure 4.12 Three-dimensional constitutive surface of the soil structure (Fredlund, 1993).

The relation between suction and deformation is shown in Figure 4.12. When the matric suction decreases, the deformation increases. This is very significant for the stability of soil structures. During the wetting cycle, as discussed in Section 4.3, the matric suction decreases and in parts where the previously unsaturated soil becomes fully saturated, the suction becomes zero and pore-water pressures take over.

To describe the *plastic* deformation during the wetting cycle the Barcelona Basic Model (BBM) was formulated by Alonso (1990). The BBM is a widely used elasto-plastic model, including the collapse potential decrease with increasing net stress. The model is intended for unsaturated soils, which are slightly too moderately expansive.

The Load Collapse (LC) yield surface in the $p = (\sigma - u_a)$ and $s = (u_a - u_w)$ plane (see Figure 4.13) follows from, See also Figure 4.14:

$$p'_c = p'_r \left(\frac{p_c^*}{p'_r} \right)^{\left(\frac{\lambda_0^* - \kappa^*}{\lambda_s^* - \kappa^*} \right)} \quad [4.16]$$

p'_r = reference stress

p'_c = pre-consolidation stress

p_c^* = pre-consolidation stress for saturated conditions

κ^* = modified swellings index

λ_0^* = modified compression index, for $s=0$

The stiffness parameter for changes in suction for virgin states of soils is defined by:

$$\lambda_s^* = \lambda_0^* \left[(1-r) \exp(-\zeta s) + r \right] \quad [4.17]$$

r = parameter maximum soil stiffness

ζ = parameter controlling the rate of increase of soil stiffness with suction

In Figure 4.13 the stiffness parameter for $s=0$ and s is illustrated.

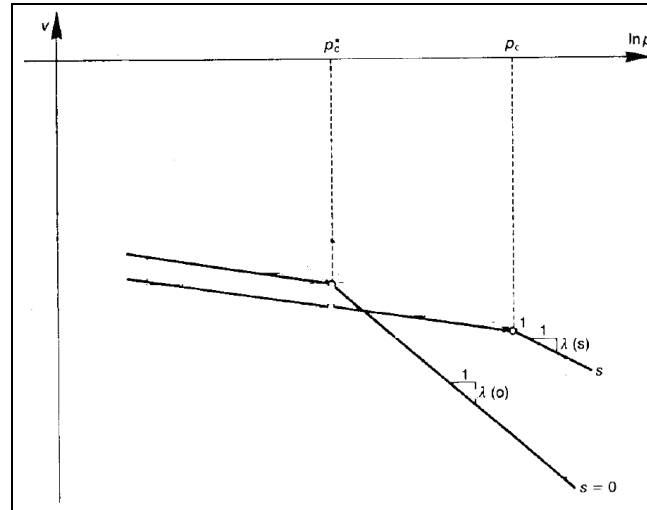


Figure 4.13 stiffness parameter change under influence of suction (Alonso, 1990)

An increase of suction may also lead to plastic strains. Therefore, a Suction Increase (SI) yield curve is introduced. In Figure 4.14 the LC and SI curve are illustrated in a mean stress versus suction plot.

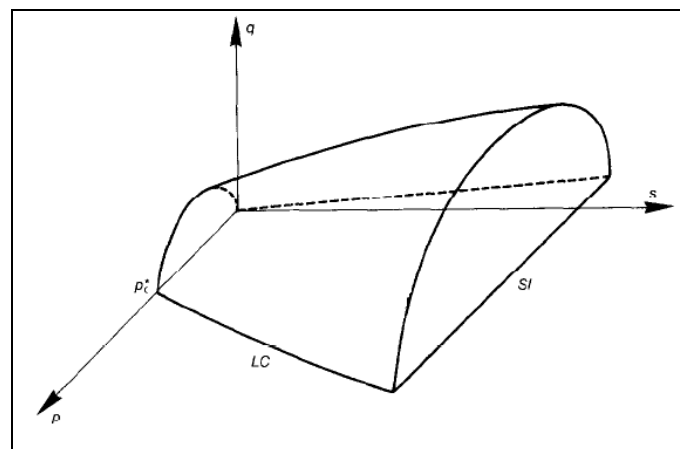


Figure 4.14 Barcelona Basic model in p - q - s space (Alonso, 1990)

The Barcelona Basic model is also implemented in the Finite Element model Plaxis. In Chapter 5 the Finite Element program is elaborated and a material model is chosen for the analysis.

Approach 2: Bishop effective stress

In this approach the effective stress is derived according to Bishop Eq. [4.5]. This effective stress (for each direction) is used in an elasto-plastic model to obtain the elastic strain.

The χ -parameter in Eq [3.5] is often replaced by S (degree of saturation), (Bolzon, 1996), due to lack of experimental data. Bishop's effective stress can now be formulated in tensor notation as:

$$\sigma' = \sigma - [Su_w + (1 - S)u_a] \quad [4.22]$$

As both wetting and drying cycles can cause plastic deformation, a coupled elasto-plastic framework was proposed by Wheeler (2003). In this model the hydraulic hysteresis and the mechanical behaviour are linked by the degree of saturation. The mean Bishop effective stress p^* and a modified suction s^* variable are defined respectively as:

$$p^* = p - Su_w - (1 - S)u_a \quad [4.23]$$

$$s^* = n(u_a - u_w) \quad [4.24]$$

where n is porosity.

The degree of saturation influences the stress-strain behaviour; conversely the volumetric strain also influences the degree of saturation. With volume decrease the pore space decreases, which means a higher saturation at a given suction.

A Load Collapse (LC) yield surface can be constructed with a straight vertical line in a s^* versus p^* plot and alters with the degree of saturation. For example, during the drying process the decrease in saturation causes an increase in suction in water bridges and hence an increase in interparticle force which stabilizes the soil skeleton against interparticle slippage. This results in a delayed collapse of the soil and thus an enhanced LC- surface. In case of wetting, the degree of saturation increases and reduces the stability. Then, the mean Bishop stress reduces, i.e. the vertical LC-surface moves to lower values.

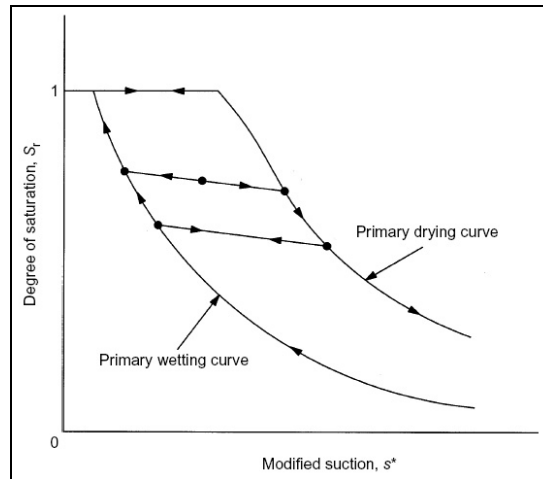


Figure 4.15 Hysteretic behaviour of wetting and drying as an elasto-plastic process (Wheeler 2003)

In Figure 4.15 the hysteretic behaviour of wetting and drying is represented. The plastic changes in S occur along the primary wetting and drying curves. Plastic changes in S on the drying curve correspond with air intake in the soil skeleton. Plastic changes in S on the wetting curve correspond with flooding of the pore spaces in the soil skeleton. The changes in S between the primary wetting and drying curves is reversible and thus not plastic. This behaviour can be represented by Suction Increase (SI) and

Suction Decrease (SD) yield surfaces. In Figure 4.16 this coupled LC, SI and SD yield surfaces for isotropic stress states are shown.

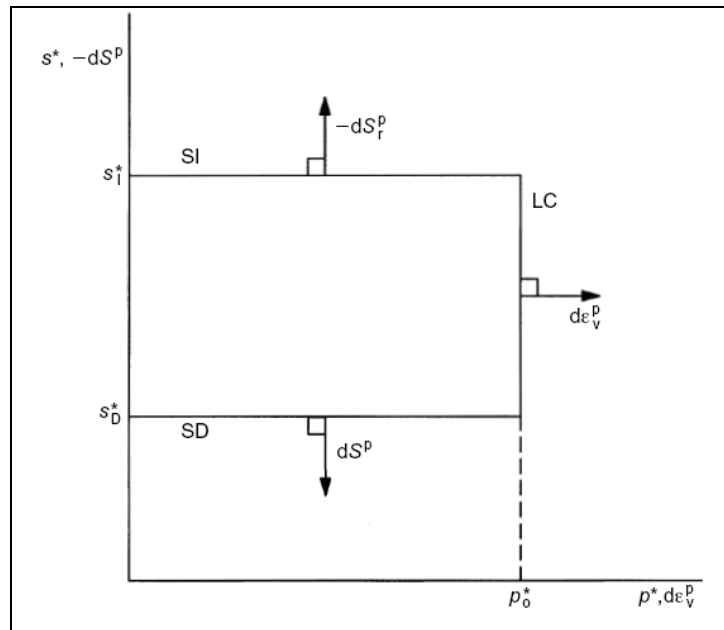


Figure 4.16 LC, SI and SD yield surfaces for isotropic stress states (Wheeler 2003)

According to Figure 4.16, yielding on the LC curve causes plastic volumetric strain, which produces coupled upward movement of the SI and SD curves. Yielding on the SI curve causes plastic decrements of S , which produces coupled upward movement of the SD curve and outward movement of the LC curve. Yielding on the SD curve causes plastic increments of S , which produces coupled downward movement of the SI curve and inward movement of the LC curve.

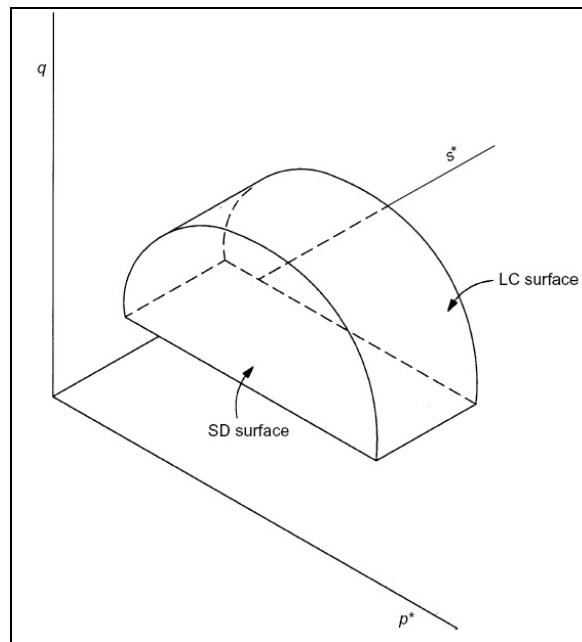


Figure 4.17 LC, SI and SD yield surfaces for anisotropic state in $p^*;s^*;q$ plane (q represents the deviator stress).(Wheeler 2003.)

In Figure 4.17 the LC, SI and SD yield surfaces for the anisotropic state are displayed. Compared to the isotropic case, the LC surface is curved and the SI and SD surfaces are planar.

4.5. Unsaturated zone in rocks

So far the unsaturated zone in soils has been addressed. In this Section the unsaturated zone in rocks will be evaluated. The principles of unsaturated zone mechanics is, however, similar to that for soils.

The suction model, formulated by Bishop, was analyzed for Rocks by (Da Silva, 2008). The study focuses on shale type rocks, but also briefly addresses limestone and sandstone. Suction was induced in the experiments with osmosis, using polyethylene glycol as a solute. A modified Bishop effective stress, including the Biot coefficient, was tested to predict the increase in uniaxial compressive strength with suction (Da Silva, 2008). The effective stress expression is interpreted as:

$$\underline{\sigma}' = (\underline{\sigma} - bu_a \underline{I}) + \chi b(u_a - u_w) \underline{I} \quad [4.27]$$

χ is assumed to be equal to the degree of saturation. b is the Biot coefficient and depends on the rock structure macroscopic compressibility K_s to the mineral K_m compressibility:

$$b = 1 - \frac{K_m}{K_s} \quad [4.28]$$

The Biot coefficient can be estimated for rock with (Fabre and Gustkiewics, 1997):

$$b = 1 - \exp\left(-a_r \tan\left(\frac{\pi}{2} n\right)\right) \quad [4.29]$$

where n is the porosity and a_r an empirical parameter, which depends on the rock type. Some examples are: $a_r \approx 5.5$ for sandstone, $a_r \approx 4.5$ for limestone and $a_r \approx 5$ for shale.

Further derivation of equations gives for the uniaxial compressive strength with suction:

$$\sigma_c(s) = \sigma_{c;sat} + 2 \tan\left(\frac{\pi}{4} + \frac{\varphi'}{2}\right) S_r b s \tan \varphi' \quad [4.30]$$

where $\sigma_{c;sat}$ is the saturated uniaxial compressive strength of rock.

From their research, it was concluded that the modified Bishop effective stress was in good agreement with the experimental data. Another observation in the study was that the σ_c remains constant until a suctions of 10 MPa. For suction greater than 10 MPa, σ_c increases depending on rock type. In Figure 4.18 the relation between suction and uniaxial compressive strength for various limestone's and sandstones is shown.

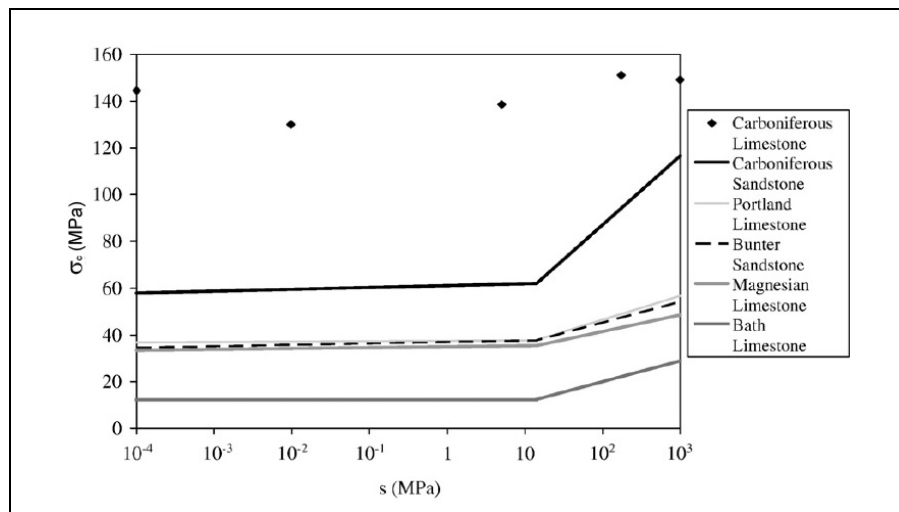


Figure 4.18 Uniaxial compressive strength evolution with suction for limestone's and sandstones. With the following porosity's: Carboniferous limestone ($n=1\%$), carboniferous sandstone ($n=8\%$), Portland limestone ($n=19\%$), Bunter sandstone ($n=21\%$), Magnesian limestone ($n=22\%$), Bath limestone ($n=23\%$). (from West, 1994 modified by Da Silva 2008)

5 Finite Element (FE) modelling

The FE program Plaxis is used to study the behaviour of slow moving landslides with as main influence the precipitation and evapotranspiration. The latest development in FE modelling is the coupling between deformation and groundwater flow, known as coupled analysis. In addition, the mechanics of the unsaturated zone is included. The implementation of these two aspects in the new version of Plaxis is therefore a major step forward in the prediction of soil structure behaviour.

The case study here is the Big Rock Mesa (BRM); see Chapter 3. The BRM is a landslide located in California (USA) near the city of Malibu (North of Los Angeles). The BRM consists predominately of sandstone with intrusive basalt layers.

In this Chapter the material model selected for the calculations will be discussed. Also the constitutive laws for the flow, deformation and unsaturated zone will be elaborated.

5.1. Material models

In Plaxis various material models can be selected to describe the soil/rock mechanical behaviour, including: the Mohr-Coulomb, Cam Clay, Barcelona Basic, Soft Soil Creep, Jointed Rock and the Hardening model.

- The BRM landslide consists mainly of sandstone, basalt and landslide debris. Thus the Soft Soil Creep model can be excluded.
- The Mohr-Coulomb model is widely used to describe elasto-plastic material behaviour.
- The advantage of the hardening model over the Mohr-Coulomb model is the increase of stiffness through compaction hardening. In rock, the grains are cemented together which limits the compaction hardening.
- The Jointed Rock model allows for diversity in stiffness (in x, and y-direction) due to faults. However, this study focuses on the movement of the shear zone.
- The Barcelona Basic model is an extension of the Cam-Clay model for the unsaturated zone.

The Mohr-Coulomb model and the Barcelona Basic model are considered for the analysis of the BRM. The Barcelona basic model describes, like the Cam-Clay model, the behaviour of soft soils (clays). However, the Barcelona Basic model is the only model with a specific application for unsaturated zone behaviour. In this Section both models are briefly discussed. In Section 5.4 the models are compared with respect to unsaturated zone mechanics.

5.1.1. Mohr-Coulomb (MC)

The MC model is widely used to determine the deformations of a soil or rock body. An elasto-plastic behaviour is assumed to derive the deformations for different stress situations and to establish the plastic yield surfaces.

In elasto-plastic models the strain can be divided into a recoverable elastic strain (ϵ^e) and an irrecoverable plastic strain (ϵ^p) part:

$$\underline{\epsilon} = \underline{\epsilon}^e + \underline{\epsilon}^p \quad [5.1]$$

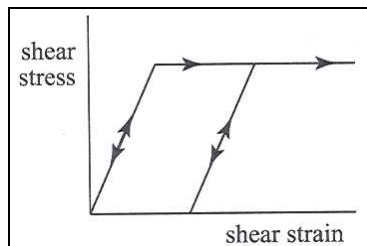


Figure 5.1 Elastic-plastic model (Wood, 2004)

The elastic stress-strain relationship follows from Hooke's Law:

$$\begin{pmatrix} d\sigma_{xx} \\ d\sigma_{yy} \\ d\sigma_{zz} \\ d\sigma_{xy} \\ d\sigma_{yz} \\ d\sigma_{zx} \end{pmatrix} = \frac{E}{(1+\nu)(1-2\nu)} \begin{pmatrix} 1-\nu & \nu & \nu & 0 & 0 & 0 \\ \nu & 1-\nu & \nu & 0 & 0 & 0 \\ \nu & \nu & 1-\nu & 0 & 0 & 0 \\ 0 & 0 & 0 & 1-\nu & 0 & 0 \\ 0 & 0 & 0 & 0 & 1-\nu & 0 \\ 0 & 0 & 0 & 0 & 0 & 1-\nu \end{pmatrix} \begin{pmatrix} d\epsilon_{xx}^e \\ d\epsilon_{yy}^e \\ d\epsilon_{zz}^e \\ d\gamma_{xy}^e \\ d\gamma_{yz}^e \\ d\gamma_{zx}^e \end{pmatrix} \quad [5.2]$$

In matrix form:

$$\underline{\dot{\sigma}} = \underline{D}^e \underline{\dot{\epsilon}}^e \quad [5.3]$$

The MC yield functions, which indicate whether plastic deformations occur, can be given by:

$$\begin{aligned} f_1 &= \frac{1}{2}(\sigma'_1 - \sigma'_3) - \frac{1}{2}(\sigma'_1 + \sigma'_3) \sin \phi - c \cos \phi \\ f_2 &= \frac{1}{2}(\sigma'_3 - \sigma'_1) - \frac{1}{2}(\sigma'_1 + \sigma'_3) \sin \phi - c \cos \phi \\ f_3 &= \frac{1}{2}(\sigma'_2 - \sigma'_3) - \frac{1}{2}(\sigma'_2 + \sigma'_3) \sin \phi - c \cos \phi \\ f_4 &= \frac{1}{2}(\sigma'_3 - \sigma'_2) - \frac{1}{2}(\sigma'_2 + \sigma'_3) \sin \phi - c \cos \phi \\ f_5 &= \frac{1}{2}(\sigma'_1 - \sigma'_2) - \frac{1}{2}(\sigma'_1 + \sigma'_2) \sin \phi - c \cos \phi \\ f_6 &= \frac{1}{2}(\sigma'_2 - \sigma'_1) - \frac{1}{2}(\sigma'_1 + \sigma'_2) \sin \phi - c \cos \phi \end{aligned} \quad [5.4]$$

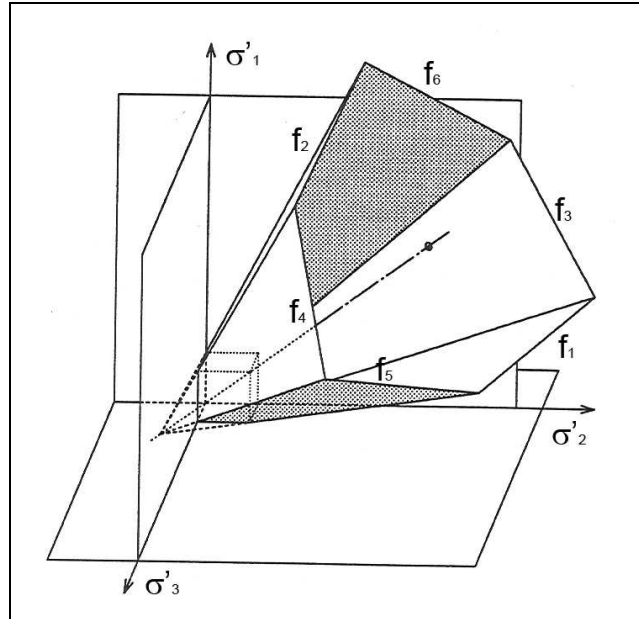


Figure 5.2 Mohr Coulomb yield surfaces in principal space (Sitters, 2006)

The material behaviour related to the yield criteria for any hardening/softening elasto-plastic model is specified by:

$f < 0$ and $df \neq 0$	elastic behaviour
$f = 0$ and $df < 0$	unloading from plastic state
$f = 0$ and $df = 0$	plastic behaviour

The representation of the yield criterion as mean effective stress (p') and deviatoric stress (q) can be defined with the following yield function (Wood 2004):

$$f(p', q) = q - Mp' \quad [5.5]$$

The mean effective stress (p') and deviatoric stress (q) can be expressed as:

$$p' = \frac{1}{3} \sigma'_1 + \sigma'_2 + \sigma'_3 \quad [5.6]$$

$$q = \frac{1}{\sqrt{2}} \sqrt{(\sigma'_1 - \sigma'_2)^2 + (\sigma'_2 - \sigma'_3)^2 + (\sigma'_3 - \sigma'_1)^2} \quad [5.7]$$

In Figure 5.3 the yield surface in $p' - q$ plane is illustrated. The tangent of the yield surface (M) relates to angle of internal friction (ϕ) for triaxial compression:

$$M = \frac{6 \sin \phi}{3 - \sin \phi} \quad [5.8]$$

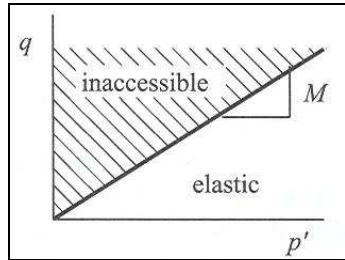


Figure 5.3 Elastic-plastic Mohr-Coulomb model (Wood, 2004)

The plastic strain can be derived from the flow rule:

$$\underline{\dot{\epsilon}}^p = \lambda_p \frac{\partial g}{\partial \underline{\sigma}'} \quad [5.9]$$

where:

λ_p = plastic multiplier

g = plastic potential

For many materials the plastic potentials are equal to the yield functions (associated plastic flow). For the associated flow the angle of dilatancy (ψ) is equal to the friction angle (ϕ). In the case of soil and rock the dilatancy angle is generally smaller than the friction angle. Then, non-associated flow occurs and $g \neq f$.

The Mohr-Coulomb plastic potential functions are given by:

$$\begin{aligned}
 g_1 &= \frac{1}{2}(\sigma'_1 - \sigma'_3) - \frac{1}{2}(\sigma'_1 + \sigma'_3) \sin \psi + c \\
 g_2 &= \frac{1}{2}(\sigma'_3 - \sigma'_1) - \frac{1}{2}(\sigma'_1 + \sigma'_3) \sin \psi + c \\
 g_3 &= \frac{1}{2}(\sigma'_2 - \sigma'_3) - \frac{1}{2}(\sigma'_2 + \sigma'_3) \sin \psi + c \\
 g_4 &= \frac{1}{2}(\sigma'_3 - \sigma'_2) - \frac{1}{2}(\sigma'_2 + \sigma'_3) \sin \psi + c \\
 g_5 &= \frac{1}{2}(\sigma'_1 - \sigma'_2) - \frac{1}{2}(\sigma'_1 + \sigma'_2) \sin \psi + c \\
 g_6 &= \frac{1}{2}(\sigma'_2 - \sigma'_1) - \frac{1}{2}(\sigma'_1 + \sigma'_2) \sin \psi + c
 \end{aligned}
 \tag{5.10}$$

The MC model allows for an elasto-plastic behaviour of the soil and rock with plasticity following non-associated flow.

A disadvantage of the MC model is that the behaviour of rock (and also sand) is not truly elasto-plastic. Irrecoverable deformations also occur before the plasticity according to the MC model sets in. Rock at the surface is brittle, rock at greater depth is more ductile due to the higher temperatures. In rock mechanics, the MC model is often used to determine the yield surfaces and the derivation of elastic strain. The MC yield surface has proven to be a reliable indication for failure of rock.

In the analysis of the BRM the deformation of the shear zone is most important. Since this zone is known for the BRM, it can be included in the modelling. It is assumed that in this case the shear zone consists of disintegrated sandstone and therefore it may be viewed as sand. Sand, however, does allow plastic deformations that can be described with the non-associated flow rule.

5.1.2. Barcelona Basic (BB)

In Section 4.4. the BB model was already introduced. In this section the model is further elaborated and described as it has been implemented in Plaxis.

The Barcelona Basic model is an extension of the Modified Cam-Clay model. The Barcelona Basic model accounts for the effects of suction in the unsaturated zone.

Modified Cam Clay (MCC)

The MCC model can be represented in the $p' - q$ space as shown in Figure 5.4.

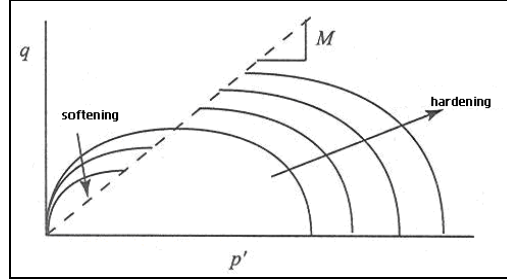


Figure 5.4 Cam-Clay yield surfaces, including hardening and softening effect (Wood, 2004).

For the MCC model, the yield function is written as:

$$f = \frac{q^2}{M^2} + p'(p' - p_c) \quad [5.11]$$

where p_c is the pre-consolidation stress and determines the size of the yield function. At the critical state line (CSL) shearing happens without any change in stress or volume. The constant M is the tangent of this line. The top of the yield curve intersects with this line.

The relation between void ratio e and p' in virgin isotropic compression is logarithmic and can be written as:

$$e - e_o = \lambda \ln \left(\frac{p'}{p^0} \right)$$

However, for isotropic unloading and reloading it holds that:

$$e - e_o = \kappa \ln \left(\frac{p'}{p^0} \right)$$

where;

$$\lambda = \frac{C_c}{2.3} \quad \kappa \approx 1.3 \frac{1-\nu}{1+\nu} C_s \quad [5.15a \text{ and } b]$$

λ = compression index

κ = swelling index

C_c = one-dimensional compression index

C_s = one-dimensional swelling index

The void ratio deformation relation with the volumetric strain is:

$$d\varepsilon_v = \frac{de}{1+e}$$

In Figure 5.5 the linear normal consolidation line and the unloading-reloading lines are presented. Compaction of the volume happens when the void ratio e decreases. This causes the soil to harden. This hardening effect only comes into play when the pre-consolidation stress is reached.

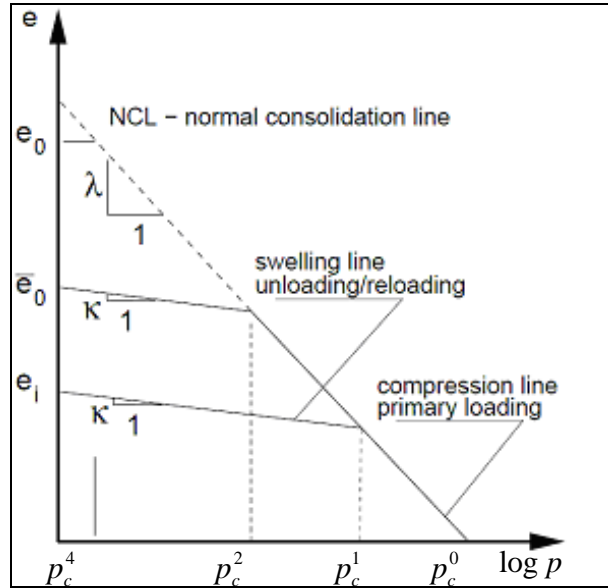


Figure 5.5 Relation between void ratio, mean stress and pre-consolidation stress (<http://www.finesoftware.eu>)

The plastic potential is given by the associated flow, which follows from: $g = f$

Then, the flow rule is written as:

$$\frac{d\varepsilon_v^p}{d\varepsilon_s^p} = \frac{\partial g / \partial p}{\partial g / \partial q} = \frac{M^2 - q^2 / p^2}{2 q / p} \quad [5.16]$$

where:

$d\varepsilon_v^p$ = volumetric plastic strain

$d\varepsilon_s^p$ = plastic shear strain

The hardening and softening effect are described by the expansion and contraction of the yield surface, respectively. This is illustrated in Figure 5.4. The graph can be divided into two area's: dilatancy, which results in softening (i.e. $q > p'M$) and compaction, which results in hardening (i.e. $q < p'M$).

Barcelona Basic model (BB model)

The extension of the MCC model in the BB model lies in the expansion of the yield function with increasing suction (s). In Figure 5.6 this effect is shown in the three-dimensional p - q - s space.

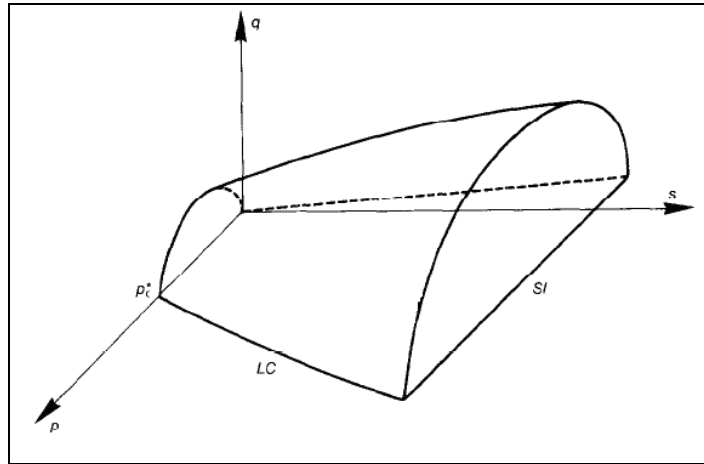


Figure 5.6 BB model in p - q - s space (Alonso, 1990).

In the p - s plane two additional yield surfaces can be identified: the Load-Collapse curve (LC) and the Suction Increase curve (SI). These two surfaces are discussed in Section 4.4.

In Figure 5.7 the yield function for two suction states is presented. The expansion of the yield surface and the movement of the CSL can be explained with the increase of interparticle force in the unsaturated zone as described in Section 4.2.3.

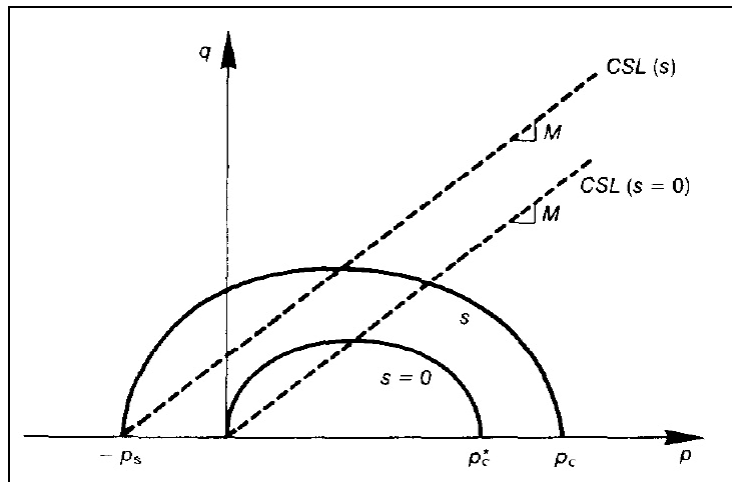


Figure 5.7 p - q plane yield surface for two suction situations, p_s is Pressure increase due to the increase in cohesion, (Alonso, 1990).

Implementation in Plaxis

In the original BB model the effective stress is defined from net stress and matric suction. However, in Plaxis, the Bishop stress has been used to calculate the effective stress.

The behaviour of saturated soils (i.e. $s = 0$) is represented by the MCC model.

The yield function reads:

$$f = 3J^2 - \left(\frac{j(\iota)}{j(-30^\circ)} \right)^2 M^2 (p' + p'_s)(p'_c - p') \quad [5.18]$$

p'_s = Increase in cohesion with suction

J = second stress invariant of deviatoric stress tensor

$$j(\iota) = \frac{\sin \varphi'}{\cos \iota + \frac{\sin \iota \sin \varphi'}{\sqrt{3}}} \quad [5.19]$$

ι = Lode's angle

The elastic response to changes in suction is written as:

$$d\varepsilon_{ij}^e = \frac{\kappa_s}{3(s + p_a)} ds \quad [5.20]$$

where:

κ_s = elastic stiffness changes for suction

The plastic flow rule can be written as:

$$d\varepsilon_{ij}^p = d\lambda_p \frac{\partial G(\sigma_{ij}, \chi_{ih}, s)}{\sigma_{ij}} \quad [5.21]$$

$d\chi_{ih}$ = increment of hardening parameters

$$G = \alpha 3J^2 - \left(\frac{g(\theta)}{g(-30^\circ)} \right)^2 M^2 (p' + p'_s)(p'_c - p') \quad [5.22]$$

$$\alpha = \frac{M(M-9)(M-3)}{9(6-M)} \left[1 / (1 - \kappa^* / \lambda_0^*) \right] \quad [5.23]$$

The evolution of the yield surface is controlled by the hardening parameter p_c^* at $s=0$ (Alonso, 1990):

$$dp'_c = \frac{p'_c}{\lambda_0^* - \kappa^*} d\varepsilon_v^p \quad [5.24]$$

Including Bishop effective stress

In Section 4.2., the Bishop's stress theory is presented. In this context, Bishop's stress (according to equation [4.5]) is used in Plaxis in matrix form as:

$$\underline{\sigma} = \underline{\sigma}' + \underline{m}(\chi u_w + (1 - \chi)u_a) \quad [5.25]$$

where:

$$\underline{\sigma} = (\sigma_{xx} \ \sigma_{yy} \ \sigma_{zz} \ \sigma_{xy} \ \sigma_{yz} \ \sigma_{zx})^T \quad [5.26]$$

$$\underline{m} = (1 \ 1 \ 1 \ 0 \ 0 \ 0)^T$$

There are two special cases, namely:

- Fully saturated ($\chi = 1$) $\Rightarrow \underline{\sigma} = \underline{\sigma}' + \underline{m}u_w$
- Fully dry ($\chi = 0$) $\Rightarrow \underline{\sigma} = \underline{\sigma}' + \underline{m}u_a$

For practical applications the air pore pressure is assumed to be constant in Plaxis and small enough to be neglected ($p_a \approx 0$). The matric suction coefficient χ is determined from experiments. The experimental evidence for χ are sparse and therefore this parameter is often assumed equal to the degree of saturation (Bolzon, 1996). Also in Plaxis the degree of saturation is used for χ .

This assumption leads to the following simplification of Eq.[5.25]:

$$\underline{\sigma} = \underline{\sigma}' + \underline{m}(Su_w) \quad [5.27]$$

As stated in Section 4.4, the BB model is intended for soils, which are slightly too moderately expansive (swelling). Also the MCC model, which is used when $s=0$, is for soft soils. The plastic potential follows from associated flow, where: $\varphi = \psi$. Sand and rock are hard soils and non expansive. The dilatancy is usually smaller than the friction angle ($\varphi > \psi$), advocating non-associated flow.

5.2 Constitutive relations

The constitutive relations for flow of pore water and deformation of the soil skeleton will be discussed in this Section. Also the hydraulic models will be elaborated.

5.2.1 Flow

The flow of water through porous media can be expressed with the law of Darcy:

$$q_x = -k_x \frac{\partial \phi}{\partial x} \quad [5.28]$$

where:

$k_{x,y,z}$ = permeability in x,y and z-direction

For equilibrium in a 3-dimensional space it holds that:

$$k_x \frac{\partial \phi}{\partial x} + k_y \left(\frac{\partial \phi}{\partial y} + \gamma_w \right) + k_z \frac{\partial \phi}{\partial z} = 0 \quad [5.29]$$

which in terms of pressure is written as:

$$\nabla \underline{u}_w + \rho_w \underline{g} + \underline{\phi} = 0 \quad [5.30]$$

$$\underline{g} = [0, -g, 0]^T$$

In a 2-dimensional situation the z-direction is omitted. For transient flow the continuity condition applies (Plax flow Manual):

$$\frac{\partial q_x}{\partial x} + \frac{\partial q_y}{\partial y} + c_c \frac{\partial \phi}{\partial t} = Q \quad [5.31]$$

where c_c is the effective capacity and Q is the discharge.

The boundary conditions as used in Plaxis are as follows (Plaxis Manual):

- Closed boundary $\underline{q} \cdot \underline{n} = 0$
- Inflow $\underline{q} \cdot \underline{n} = -|\bar{q}|$
- Outflow $\underline{q} \cdot \underline{n} = |\bar{q}|$

(\underline{n} is the outward pointing normal vector component on the boundary)

Boundary condition infiltration/evapotranspiration

The flux is described with:

$$\begin{array}{lll} \phi \leq y + \bar{\phi}_{\max} & \text{if} & \text{ponding} \\ \underline{q} \cdot \underline{n} = -\underline{q} & \text{if} & y + \bar{\phi}_{\min} < y + \phi < y + \bar{\phi}_{\max} \\ \phi \leq y + \bar{\phi}_{\min} & \text{if} & \text{drying} \end{array}$$

Ponding is rainfall water accumulating at the surface because the maximum infiltration rate of the soil is reached. When the maximum infiltration rate is reached, the condition switches to the inflow due to the prescribed head $\bar{\phi}_{\max}$. If the soil can take in more water, the prescribed head changes back to inflow.

Drying of the soil due to an outward flux (evapotranspiration) lowers the groundwater level. The condition of $\bar{\phi}_{\min}$ is a limit to where the groundwater level can drop with respect to the surface.

In Figure 5.8 a general overview of these conditions is given.

In the case of the BRM, the evapotranspiration is known and therefore the outflow through the surface is exact. The condition for maximum lowering of the groundwater head is thus set low to allow for maximal influence of the evapotranspiration on the lowering of the groundwater level. The condition $\bar{\phi}_{\min}$ is set to -360 m.

The rain inflow on the other hand is less specific, because the run off is an estimated. Moreover, the hydrauger outflow, which is also subtracted from the rainfall, is an overall average. The condition of prescribed ponding head $\bar{\phi}_{\max}$ is set to 0.01 m.

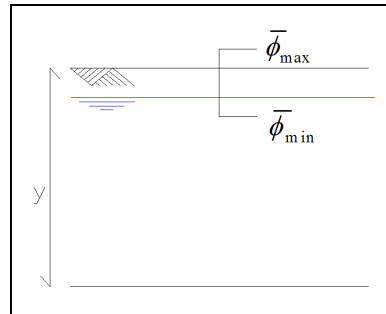


Figure 5.8 Infiltration and evapotranspiration conditions

The pore pressure profile in Plaxis for steady state is considered to be linear for the hydrostatic situation. In case of transient flow, evapotranspiration at the surface causes the suction to increase. This leads to an increase in pore suction at the surface. Long term evapotranspiration can therefore lead to a decrease in phreatic level as illustrated in Figure 5.9.

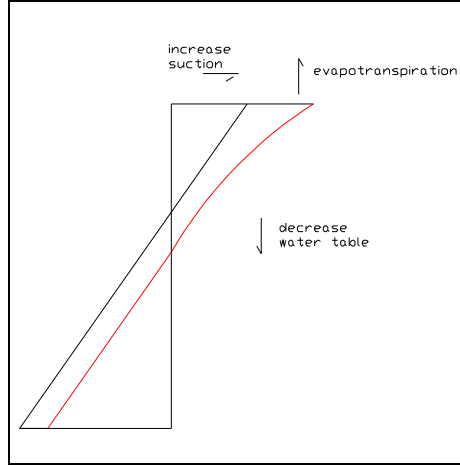


Figure 5.9 General pore pressure profile

5.2.2. Deformation

In this section the relations between the deformation and the stress and strain conditions are given. As discussed in the previous sections, pore water pressures and suction has a large effect on the stress and strain situation. To describe these relations, the linear momentum of a soil element is considered, which is governed by:

$$\underline{\underline{L}}^T \underline{\underline{\sigma}} + \underline{p} = 0 \quad [5.34]$$

where vector \underline{p} assembles the components of the body forces.

When including the Bishop stress as presented in Equation 5.34, the balance becomes:

$$\underline{\underline{L}}^T (\underline{\underline{\sigma}}' + s \underline{u}_w \underline{m}) + \underline{p} = 0 \quad [5.35]$$

where $\underline{\underline{L}}^T$ is the transpose of a differential operator, which is represented by:

$$\underline{\underline{L}}^T = \begin{pmatrix} \frac{\partial}{\partial x} & 0 & 0 & \frac{\partial}{\partial y} & 0 & \frac{\partial}{\partial z} \\ 0 & \frac{\partial}{\partial y} & 0 & \frac{\partial}{\partial x} & \frac{\partial}{\partial z} & 0 \\ 0 & 0 & \frac{\partial}{\partial z} & 0 & \frac{\partial}{\partial y} & \frac{\partial}{\partial x} \end{pmatrix} \quad [5.36]$$

The relationship between strain and displacement can be formulated as:

$$\underline{\underline{\varepsilon}} = \underline{\underline{L}} \underline{r} \quad [5.37]$$

where \underline{r} is the displacement vector.

The relation between stress and strain can be given by:

$$d\underline{\underline{\sigma}}' = \underline{\underline{M}} d\underline{\underline{\varepsilon}} \quad [5.38]$$

where $\underline{\underline{M}}$ is the material stress-strain matrix

The governing equation for the deformation model is:

$$\underline{\underline{L}}^T \left(\underline{\underline{M}} (\underline{\underline{L}} d\underline{\underline{r}} + s u_w \underline{\underline{m}}) + \underline{\underline{p}} \right) = 0 \quad [5.39]$$

5.3. Finite Element model

In FE modelling a continuum is divided into elements connected at the nodes. Shape functions (or interpolation functions) describe the variations of displacement within the elements in terms of the value of displacement at the nodes (Wood, 2004). The displacement field \underline{r} in an element results from interpolation of the (discrete) nodal values represented by vector \underline{v} . For this interpolation, shape functions are assembled in a matrix $\underline{\underline{N}}$, hence:

$$\underline{r} = \underline{\underline{N}}\underline{v} \quad [5.40]$$

Then, the displacement-strain relation becomes:

$$\underline{\varepsilon} = \underline{\underline{L}}\underline{\underline{N}}\underline{v} = \underline{\underline{B}}\underline{v} \quad [5.41]$$

5.3.1 Coupled analysis

In Plaxis the deformations are directly coupled to the hydrological conditions. This coupled analysis is represented by:

$$\begin{bmatrix} \underline{\underline{K}} & \underline{\underline{Q}} \\ \underline{\underline{Q}}^T & -\underline{\underline{S}} \end{bmatrix} \begin{bmatrix} \frac{d\underline{v}}{dt} \\ \frac{d\underline{u}_w}{dt} \end{bmatrix} = \begin{bmatrix} 0 & 0 \\ 0 & \underline{\underline{H}} \end{bmatrix} \begin{bmatrix} \underline{v} \\ \underline{u}_w \end{bmatrix} + \begin{bmatrix} \frac{d\underline{f}_u}{dt} \\ \underline{G} + \underline{q}_p \end{bmatrix} \quad [5.42]$$

In the case of a purely hydrological problem, the flow mode can be used according to the following equation:

$$\begin{bmatrix} 0 & 0 \\ 0 & -\underline{\underline{S}} \end{bmatrix} \begin{bmatrix} \frac{d\underline{v}}{dt} \\ \frac{d\underline{u}_w}{dt} \end{bmatrix} = \begin{bmatrix} 0 & 0 \\ 0 & \underline{\underline{H}} \end{bmatrix} \begin{bmatrix} \underline{v} \\ \underline{u}_w \end{bmatrix} + \begin{bmatrix} \frac{d\underline{f}_u}{dt} \\ \underline{G} + \underline{q}_p \end{bmatrix} \quad [5.43]$$

The matrix components used in Eq.[5.43] and their physical meaning are summarized in Table 5.1.

Matrix component	Description	Definition
$\underline{\underline{H}}$	permeability matrix	$\underline{\underline{H}} = \int_V (\nabla \underline{\underline{N}})^T \frac{k_{rel}}{\gamma_w} \underline{\underline{k}}^{sat} (\nabla \underline{\underline{N}}) dV$
$\underline{\underline{K}}$	stiffness matrix	$\underline{\underline{K}} = \int_V \underline{\underline{B}}^T \underline{\underline{M}} \underline{\underline{B}} dV$
$\underline{\underline{S}}$	compressibility matrix	$\underline{\underline{S}} = \int_V \underline{\underline{N}}^T \left(\frac{nS}{K_w} - n \frac{dS}{dp_w} \right) \underline{\underline{N}} dV$
$\underline{\underline{Q}}$	coupling matrix	$\underline{\underline{Q}} = \int_V \underline{\underline{S}} \underline{\underline{B}}^T \underline{\underline{m}} \underline{\underline{N}} dV$
$\underline{\underline{Q}}^T$	coupling matrix	$\underline{\underline{Q}}^T = \int_V \underline{\underline{N}}^T \underline{\underline{S}} \underline{\underline{m}}^T \underline{\underline{L}} \underline{\underline{N}} dV$
$\underline{\underline{G}}$	vector for the effect of gravity on flow in vertical direction	$\underline{\underline{G}} = - \int_V (\nabla \underline{\underline{N}})^T \frac{k_{rel}}{\gamma_w} \underline{\underline{k}}^{sat} \rho_w \underline{\underline{g}} dV$
$\Delta \underline{\underline{f}}_u$	increment of the load vector	$\Delta \underline{\underline{f}}_u = \int_V \underline{\underline{N}}^T \Delta \underline{\underline{b}} dV + \int_{\Gamma} \underline{\underline{N}}^T \Delta \underline{\underline{t}}_t dS$
$\underline{\underline{q}}_p$	flux on boundaries	$\underline{\underline{q}}_p = \int_{\Gamma} \underline{\underline{N}}^T \hat{q}_w dS$
Where	b = body force vector in the Volume t_t = traction on the boundary Γ	

Table 5.1. Matrix components used in the coupled analysis of Plaxis.

The coupling matrices describe the interplay between the flow and the deformations within the soil elements. The matrix $\underline{\underline{Q}}$ in the deformation equation is multiplied with the pore pressures to incorporate these pressures into the calculation of the deformations. On the other hand the matrix $\underline{\underline{Q}}^T$ in the flow equation is multiplied with the deformations, thus incorporating the displacement of the soil elements. For further details the reader is referred to the Plaxis manual, coupled analysis (Galavi, 2009).

5.4. Unsaturated zone mechanics

The stresses are determined according to Equation 5.27 in the calculation performed with Plaxis. This applies to all material models used in these calculations.

If suction increases, then the stress increases and the yield surface expands. The reverse is also true, i.e. if suction decreases, then the stress decreases and the yield surface shrinks. The increase in suction leads to an increase in interparticle forces (see also Section 4.2.3). These forces cause a decrease in void ratio, thus compacting and increasing the stiffness of the material. In Figure 5.10 this shift in yield surface is illustrated in the p - q plane for the MC model. This shift of the yield surface is due to suction induced cohesion as explained in Section 4.2.3.

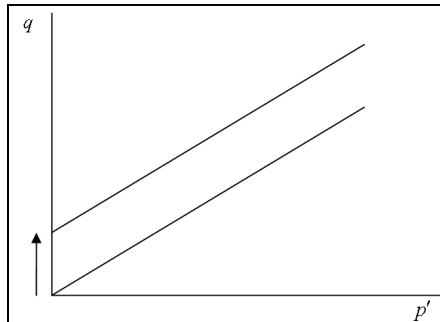


Figure 5.10 Shift of the MC yield surface due to suction (induced cohesion)

In the MC model there is no cap on the mean stress, whereas with the BB model and with the MCC model a cap is included. This cap indicates the collapse due to isotropic compression, which leads to hardening of the soil.

The BB model also includes the LC and SI curves, which describe the elastic region in the s - p plane. In Figure 5.11 these shifts are shown for loading and unloading, and for wetting and drying. The LC curve describes the increase in p_c due to an increase in suction.

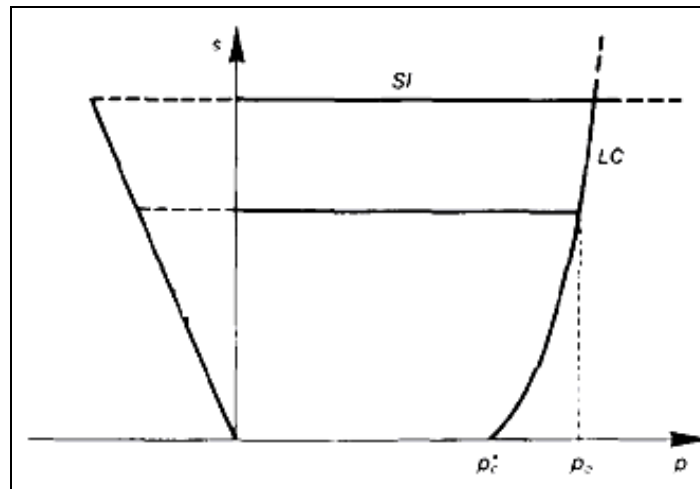


Figure 5.11 SI and LC collapse curve in the p - s plane

In Section 3.1.2 the formation of sandstone is described. Because of the Lithofication processes forming sediment stone, the compaction hardening is extremely small. The pre-consolidation stress p_c of sand- and siltstone is very high for the same reason.

Because the BB model offers no advantages over the MC model for sandstone, basalt or siltstone the MC model is used in the sensitivity study (See Chapter 7). The shear zone of the BRM is located deep below the surface, compaction has already occurred and the shear stresses and deformations are dominant. Landslide debris occurrences are not frequent and play a limited role in the movement of the landslide. Therefore the MC model is also used for the landslide debris and shear zone.

In Chapter 6 the parameters for the MC model corresponding with the different formations were already selected.

6. Motivation of parameters used in modelling of the BRM slide

When studying a landslide, many parameters have an influence on its behaviour. The hydraulics, strength, and shear zone parameters are most important. Because it is often impossible to account and measure all these parameters, other methods have to be used in order to estimate their influence. Some of these methods are geo-statistics, estimations from observations, interpolation or extrapolation to known stable and unstable situations and construction of a water balance.

In Chapter 3, the available data and geological situation have been evaluated. However, in this Chapter the additional information needed to construct a sufficiently reliable model is assessed with the above-mentioned methods. Also choices for simplification of the situation for modelling are discussed as well as the choices for modelling the steady state and the simulated periods.

6.1. Suppositions for modelling

Suppositions for the dimensions and tectonic movement have to be made for modelling the BRM landslide. The BRM will be modelled in 2D, i.e. the plane of a cross-section. However, the groundwater flow is 3-dimensional. The groundwater flow perpendicular to the cross-section is ignored. One boundary is along the ocean, which means there is a salt-fresh water divide. The location of this divide is not known.

This research focuses on the effect of precipitation on slow moving landslides. The faults (see Section 3.1.3) will be described in the geological analysis, but will be excluded in the model.

6.2. Selection of the period for modelling

The monitoring of the BRM started in 1993 on a regular basis. Before 1993 the displacement data are very limited. In Figure 5.6, the average displacement of 24 measuring points as a function of time was shown. In Figure 5.7, the maximum displacement for the same period was presented.

These figures indicate a relatively large displacement in for example 1994-1995. The cause of this large average and maximum value is the inclinometer reading of SP-26. SP-26 is located in the headscarp slide on top of the main slide (see Figure 6.2). When eliminating SP-26 from the results, as shown in Figure 6.1, the maximum displacement is significantly lower.

The reasons for choosing 2004-2005 as the period for this study are:

- The displacement measured follows after 3 years of no movement.
- The large amount of rainfall in 2004-2005 as illustrated in Figure 5.9.
- Available mass movement data of the slide (that is shown in Figure 5.8, with the number of non-zero inclinometer measurements).

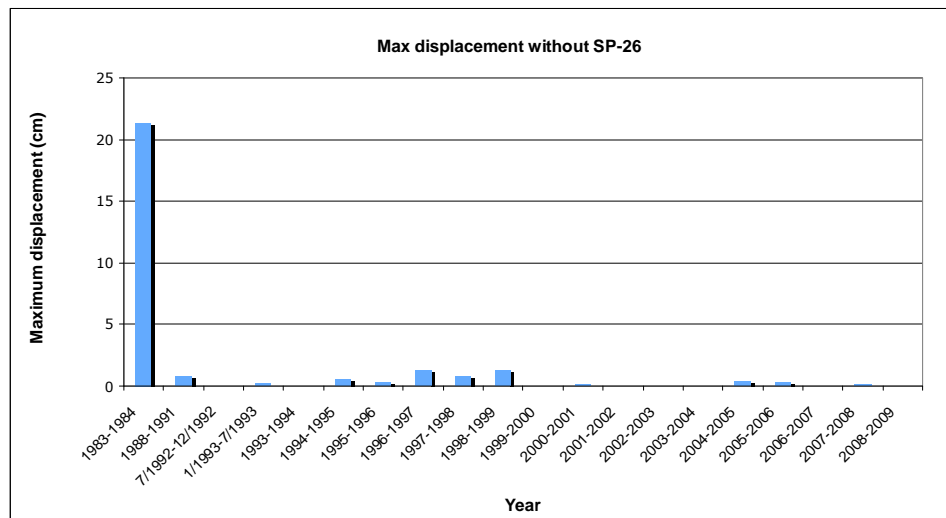


Figure 6.1 Maximum displacement over 23 inclinometers without the inclinometer reading of SP-26 (Fugro West Inc.)

From the figures illustrated in Section 5.14 and Figure 6.1, the largest displacement occurred in 1983-1984. Unfortunately, insufficient data from that period are available for modelling.

6.3. Selection of the cross-section

Cross-section D-D' (Appendix 7): This cross-section cuts through the largest part of the slide and includes the headscarp region. In the headscarp region the largest movements were measured. Also the cross-section D-D' includes the majority of the inclinometers on the slope.

In the following paragraph, the specific data of the landslide in these cross-sections are presented and evaluated. These data will be included in the parametric study.

The geometry of the main slide is presented in Figure 6.2. The slide consists of the main slide and two smaller 'sub' slides. The red lines indicate the slides that will be modelled and the blue line indicates the average groundwater level. The slide on top is the headscarp slide and the slide at the bottom of the main slide is referred to as the down slope slide.

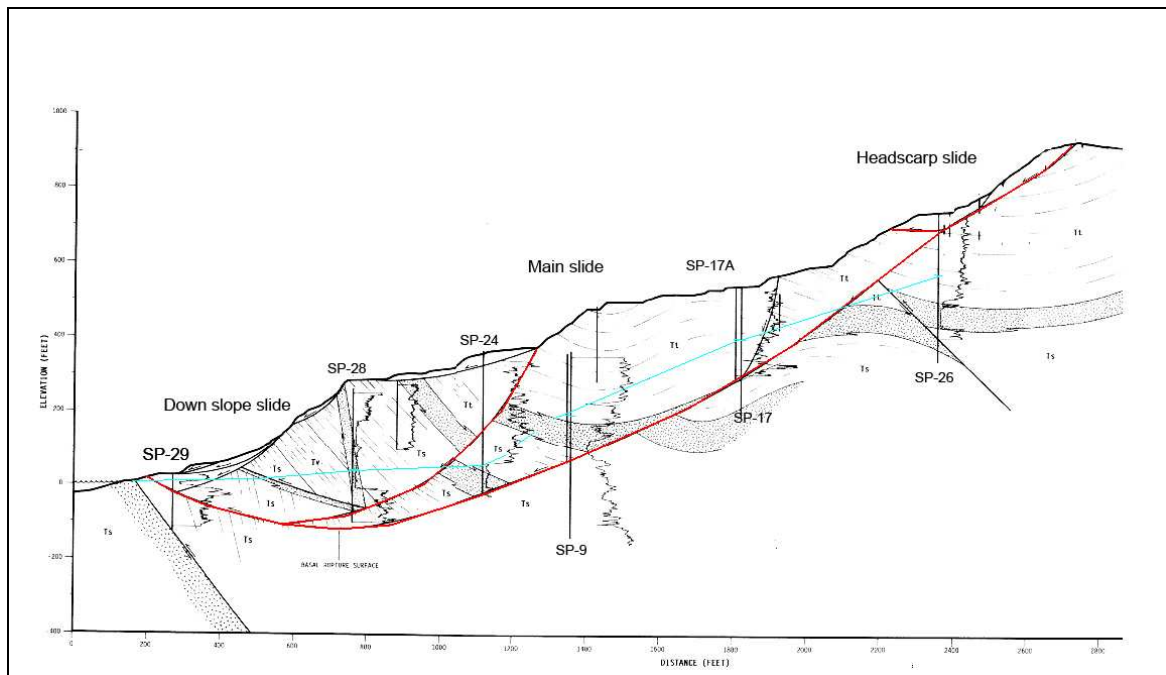


Figure 6.2 Cross-section D-D' (Bing Yen & associates, 1991)

From Figure 6.2 it is clear that the average groundwater level does not reach the smaller landslide in the upper headscarp area. There is also a jump in groundwater level between SP-24 and SP-9. This may be due to groundwater built up on top of the Conejo Volcanic rock.

The dewatering graphs are displayed in Appendix 14. In the dewatering graphs it can be seen that in the period 1994-1995 and 1998 high peaks occur corresponding with the rainfall data. However, there is no peak registered in 2005 in the hydraugers graph, while in the well production graph such a peak is present. This can be explained by the facts that five hydraugers were producing at a lesser rate than in 1998 (possibly due to clogging) and one hydrauger was shut down in 2000. Graphs of the displacement and rainfall of the main, headscarp and down slope slides are presented for the period 1992 to 2008 in Figures 6.3 a, b and c, respectively.

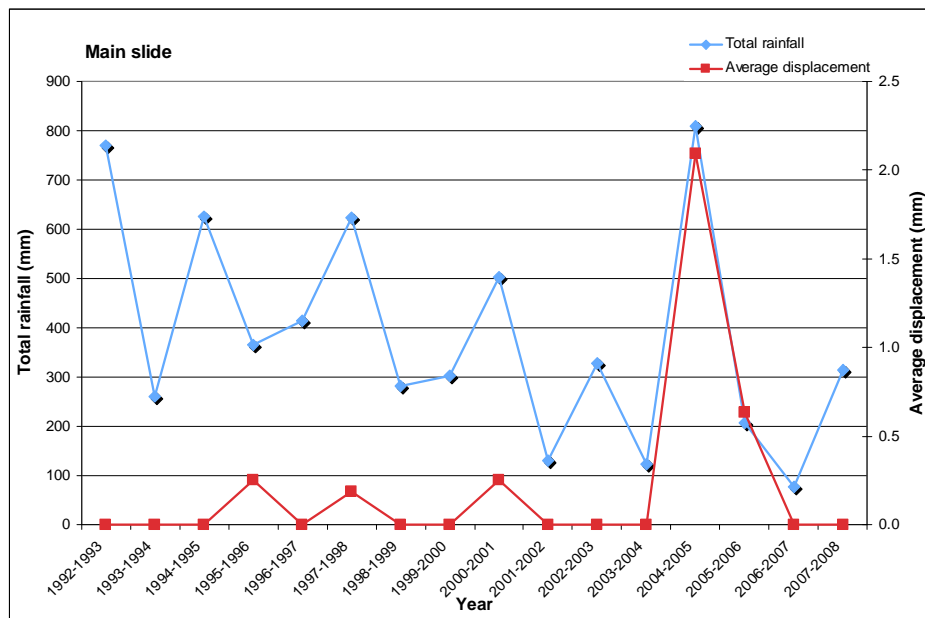


Figure 6.3a Rainfall and average displacement of the main slide of the Big Rock Mesa landslide.

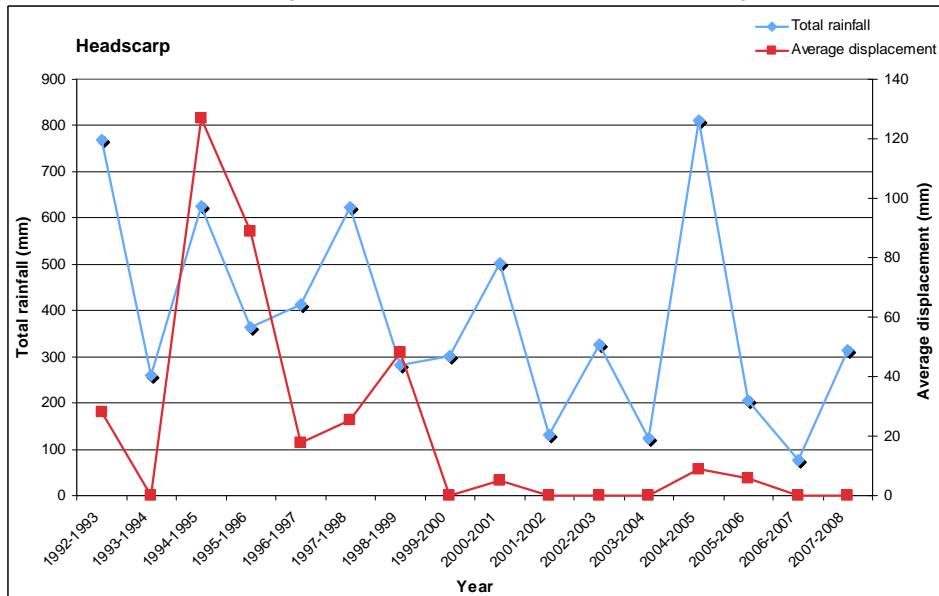


Figure 6.3 b Rainfall and average displacement of the headscarp slide of the Big Rock Mesa landslide.

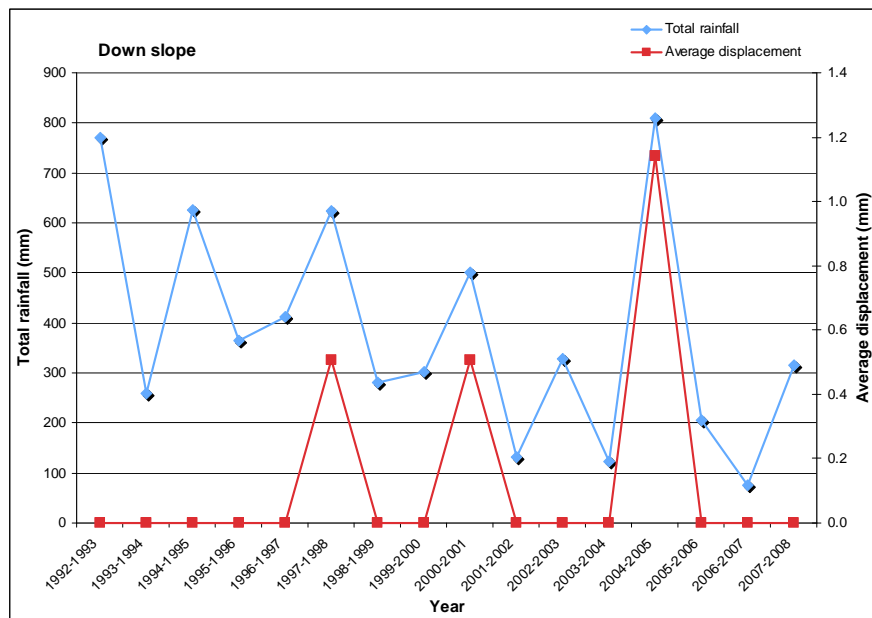


Figure 6.3 c Rainfall and average displacement of the down slope slide of the Big Rock Mesa landslide.

Displacement of the Main and Down slope slide occurs in periods of high annual rainfall. However, a significant movement of the headscarp slide occurred in the 1994-1996 when a relatively low rainfall happened; see Figure 6.3b. This may have other causes besides rainfall such as human constructions or local infiltration of water due to waste disposal systems etc. Note that the headscarp slide consists of loose landslide debris.

The displacement of the headscarp slide is presented in Figure 6.3 b. The displacement of this slide is higher than the other slides. The headscarp slide is a shallow slide on top of the slope, which is visual in Figure 6.2. It is likely that the headscarp slide contains more loose soil from weathered rock debris. Loose soil has poorer properties (including friction angle) than hard rock, which means it has less strength to accommodate activating landslide forces.

6.4. Hydraulic system

As mentioned in Section 6.1 the groundwater flow is a 3-dimensional problem. Water enters and exits the surface by rainfall and evapotranspiration. The horizontal flow is influenced by permeability of the different strata, the inflow from the vertical boundaries and by a fresh-salt water divide. Another outflow from the landslide is by wells and hydraugers installed to lower the groundwater surface.

6.4.1 Groundwater surface

To construct a water level surface, the geo-statistical program 'Surfer' has been used. The Kriging procedure has been adopted to estimate the groundwater surface of the BRM (Manual 'Surfer') . This surface is presented in Figure 6.4 along with the location of the surface, which is presented in Figure 6.5. Kriging is a least square method, whereby the sum of the square deviation is minimized.

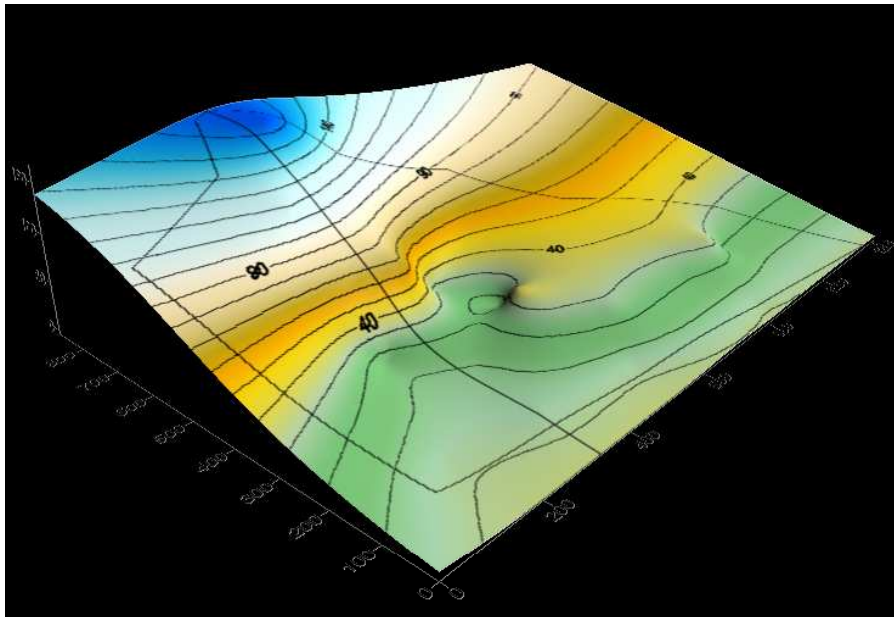


Figure 6.4 3D groundwater surface mean levels 2003-2004 (Surfer).

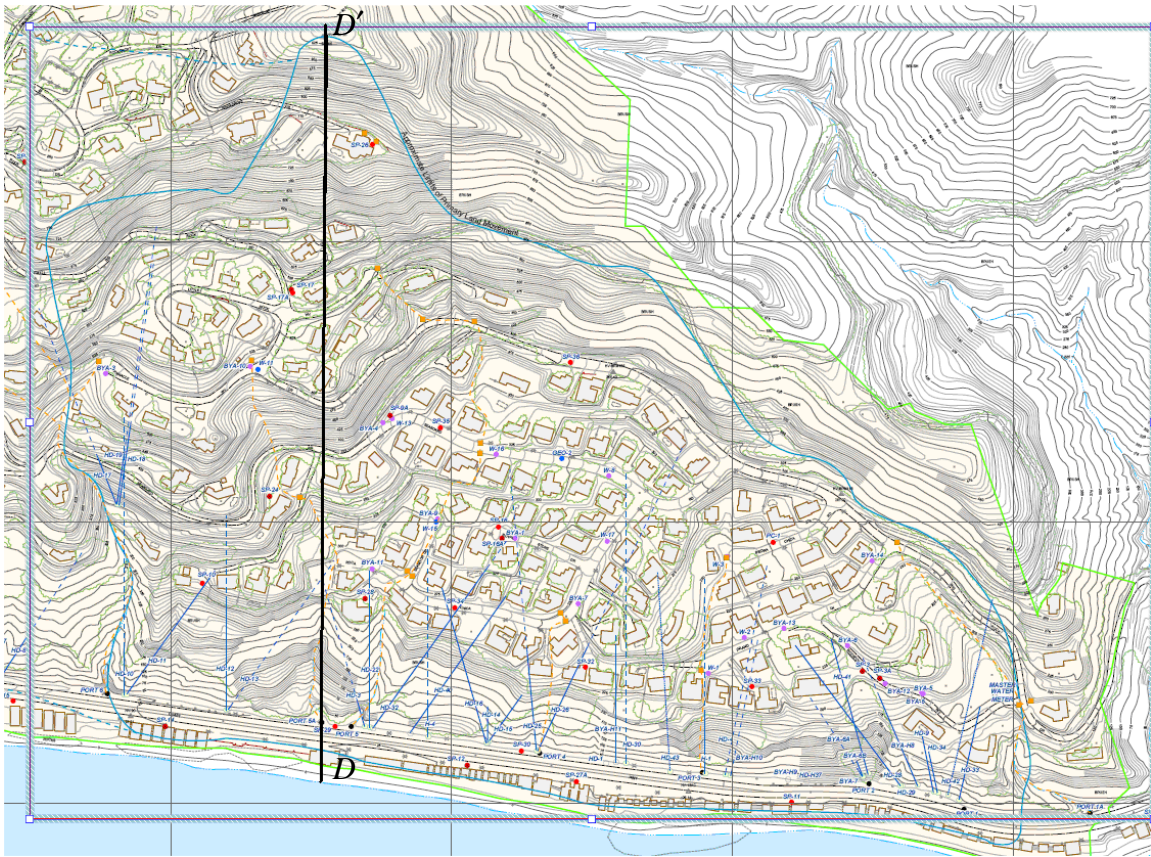


Figure 6.5 Area plotted in SURFER for Figure 6.4 (Fugro West Inc) Show cross-section D-D'

6.4.2. Upper and lower boundary groundwater level

A first estimation of the stability of the slide is made by calculation of the safety factor (see Eq. [6.17]) for the upper and lower boundary of the groundwater level. These groundwater boundaries have been determined by taken the highest and lowest value of the total data set. In Table 6.1, the highest and lowest values (with respect to Mean Sea Level (MSL) for each measuring point are shown including the first date of measurement and comments on anomalies. The location of the measuring points is shown in Appendix 3.

Area	Point (SP)	Lowest (m) MSL	Highest (m) MSL	First measuring date	Anomalies
Head	26	160.1	170	Mar 1987	Slight upward trend.
Central	9A	61.1	74.4*	Dec 1983	First two measurements excluded due to high relative values. Varies greatly until '96 after relatively steady.
	16	13.2	69.0	Jun 1984	Until '90 rel. high. After '96 steady rel. low trend.
	16A	26.7	59.8	Mar 1988	Varies greatly between 60 and 30 m.
	17	116.4	125	Dec 1983	-
	17A	112.9*	118.8	Sept 1988	First three measurements excluded due to low relative values.
	24	9.1	15.8*	Feb 1988	First four measurements excluded due to high relative values.
	35	25.8	31.7	Nov 1998	-
Bluff	36	57.5	59.5	Nov 1998	-
	10	12.5	22.6*	Dec 1983	First four measurements excluded due to high relative values.
	28	9.6	12.3	Sept 1988	One high peak.
	32	15.1	43.1	Sept 1988	One high and one very low peak.
East	34	22.2*	27.6	Nov 1998	First two measurements excluded due to low relative values. Slightly upward trend.
	PC-1	41.4	57.9	May 1995	One very high peak.
	3	26.5	38.4	Nov 1983	After 2008 strong downward trend.
	3A	15.1	31.6*	Apr 1985	First measurement excluded due to high relative values. Varies greatly.
PCH	33	20.2	47.8	Sept 1988	After 1988 strong downward trend.
	11	1.2	2.5	Sept 1988	-
	12	0.8	2.5	Sept 1988	-
	14	0.3	2.7	Oct 1987	-
	15	1.5	6.1	Oct 1987	-
	19	0.5	1.8	Sept 1988	-
	27A	2.2	4.3	Sept 1988	-
	29	4.6	6.8	Oct 1987	-
	30	1.7	4.8	Oct 1987	After 1998 upward trend.
* adjusted to settling period because of relatively extreme high or low values					
Note: All points have some interval periods of no measurement (varying from an few years to a few months)					
Note: Minimum and maximum values taken over the period from installation till August 2009					

Table 6.1 Highest and lowest values for each measuring point, first date of measurement and comments on anomalies.

The data of the highest and lowest values are then imported in Surfer. In this program a most likely groundwater surface is given. The groundwater line for the cross-section D-D' is illustrated in Figure 6.6 a and b. In Figure 6.6 c the bandwidth of the upper and lower boundary is shown. The bandwidth varies from 1-2 m at the bottom to 7-10 m in the middle and upper part.

The highest and lowest values, as displayed in Table 6.1, are based on monthly measurements from the date of first measurements to August 2009. This frequency of measuring could cause that peaks due to heavy rainfall may be missed. Thus, the upper and lower band that has been established, could be higher or lower.

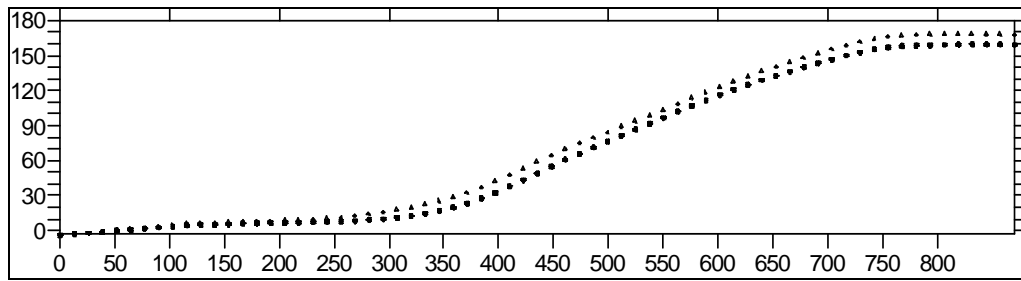


Figure 6.6 Cross-section D-D' water level bandwidth. Note: water level with respect to MSL.

6.4.3 Water balance reference period

As a reference level the mean ground water level (GWL) of 2003-2004 is used. The monitoring period of GWL's is from 1991 to 2009. In this period some changes occurred in the dewatering of the slide. The mean GWL over this period (91-09) is therefore excluded. Instead, the mean GWL of the period 2003-2004 which is taken is just prior to years studied here (04-05) and hence serves as an appropriate starting point. Also in 2003-2004 no movement was measured and it can therefore be assumed that the slide was stable for the mean GWL of 2003-2004. The water balance is constructed for the whole slide.

The known inflow is the rainfall and the known outflow consists of evapotranspiration and dewatering. The data available consists of monthly groundwater level and hydrauger production measurements, bi-monthly well production and daily rainfall and evapotranspiration measurements.

The run-off is estimated at 20% of the rainfall. This is based on study by D. Burns, T. Vitvar, J. McDonnell, J. Hassett, J. Duncan and C. Kendall (2005), where the run-off was calculated for different residential density situation. The BRM is a sub-urban environment and has therefore a medium residential density. For this situation the run-off is about 20% of the rainfall.

Besides rainfall another in flux is active in order to account for the volume change and out flux. This influx can consist of inflow through the boundary of BRM and through the on-site waste disposal units and other domestic use of water. It is also unknown if there is another out flux, such as outflow through the boundaries of the BRM. Therefore, the term X-flow, is introduced which covers all the unknown inflow minus outflow. It can also be assumed that the main component will be the inflow through the boundaries of the BRM since there is a 'high' valley located above the BRM. Analysis of the data of water consumption by the residents shows that the difference between wet and dry periods is about 380 m³/d. It is anticipated that only a minor part (say 10 %) of this consumption is used for irrigation. Therefore, the contribution by irrigation to the X-flow is probably small and can be neglected.

The water balance for the steady state 2003-2004 is given, by:

flux in – flux out = rate of change in water storage (Fitts,2002), hence:

$$R+X-D-ET-RO=\Delta Z$$

[6.1]

where R is rainfall, X is X-flow, D is dewatering, RO is run-off, ET is evapotranspiration and ΔZ equals phreatic storage change dV/dt .

Figure 6.7 represents the hydraulic system of the BRM.

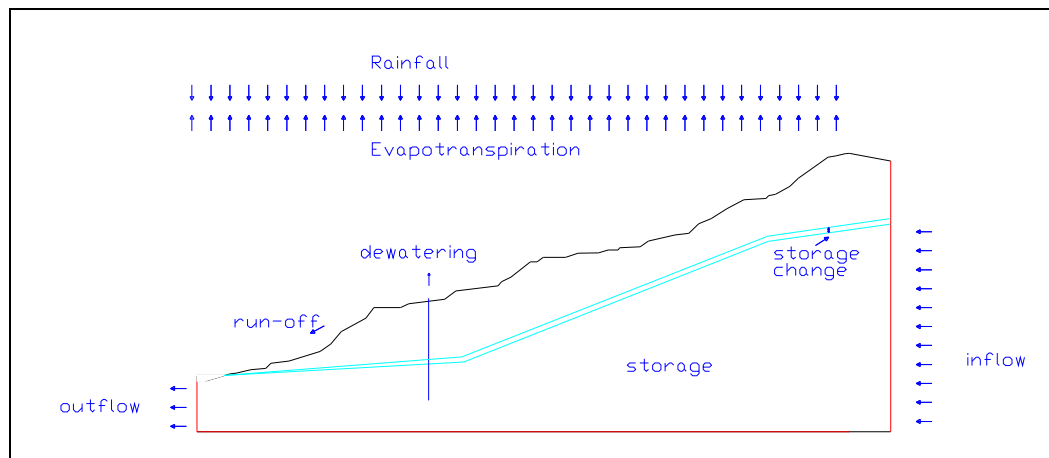


Figure 6.7 Hydraulic system of the BRM.

In Table 6.3 the inflow and outflow rates for this water balance is given.

	Flow rates	
Rainfall (R)	303	m ³ /d
run-off (RO)	61	m ³ /d
Evapotranspiration (ET)	1657	m ³ /d
Dewatering (D)	1567	m ³ /d
storage change (dZ)	377	m ³ /d
X-flow (X)	1948	m ³ /d

Table 6.3 In and outflow rates. Note: vales based on year average.

Fresh-salt water divide

In coastal aquifers an interface between fresh and salt water is present. The boundary between fresh and salt pore water is a narrow, diffuse mixing zone this is the result of molecular diffusion together with mixing caused by tidal fluctuations and fluctuating fresh water heads (Fitts, 2002). The flow patterns for fresh and salt water represent long-term averages. Fluctuations in fresh water head and tidal influences cause short-term variation in flow and can shift the interface. This transient process increases the thickness of the mixing zone.

For determining the interface between fresh and salt water the Ghyben-Herzberg relation may be used (Fitts, 2002). This relation is bases on hydrostatic conditions as has the following assumptions:

- Sharp interface between fresh and sharp.
- At the shoreline the fresh water head is equal to the sea level elevation.
- No resistance in vertical flow, for both salt and fresh water (hydrostatic conditions).

The Ghyben-Herzberg is given by:

$$z = \frac{\rho_f}{\rho_s - \rho_f} h$$

where:

z = depth of interface with respect to MSL

ρ_f = fresh water density (1.000g/cm³)

ρ_s = salt water density (1.025g/cm³)

h = head in fresh water

Applying the Ghyben-Herzberg relation to the highest and lowest measured head an upper fresh-salt water interface depth can be determined. In Figure 6.8 the upper fresh-salt water interface for cross-section D-D' is displayed. It is apparent that the fresh-salt water interface lies very deep.

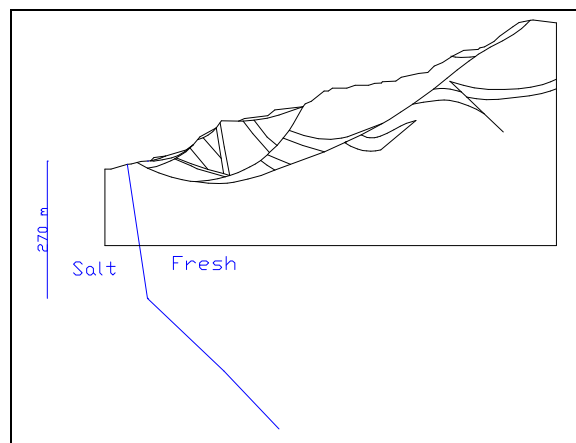


Figure 6.8 Sketched location of fresh-salt water divide.

6.4.4 Water balance analysis period

Critical periods in the analysis year will be reconstructed in Plaxis to further refine the model. In the sensitivity study (Chapter 7) the data for the monitoring year 2004-2005 form the bases for determining the range of values.

Available data

The groundwater level data for the Big Rock Mesa consists of 24 groundwater level (GWL) measuring points over an area of 55 ha. This means roughly 1 point per 2.3 ha. In Table 1 an overview is presented of the number of measurement points per month. For months in which no data points were available, the value of the previous month was adopted. The measurements took place once and sometimes twice a month. However, for detecting peak GWL after rainfall this frequency of measuring is not enough.

Month	Available data points out of a total of 24 points
July 2004	18
August	18
September	20
October	20
November	18
December	23
January 2005	23
February	19
March	9
April	24
May	24
June	24

Table 6.4 Available data points for GWL.

The rainfall and evapotranspiration data consists of daily totals. For this balance the monthly totals are multiplied by the surface area of 55 ha.

The dewatering data consists of monthly average dewatering rates for wells and hydraugers. In total there are 19 wells and 35 hydraugers. The dewatering rate of all the wells and hydraugers were measured twice a month.

Water balance

For the monitoring year 2004-2005 a monthly water balance for the whole slide has been created. Because groundwater fluctuations cause changes in the amount of water present in the system (storage change) the water balance can be formulated as shown in Equation 6.2.

The storage change is derived from:

$$\Delta Z = Z_{n+1} - Z_n \quad [6.2]$$

In Table 6.5 the volume of the landslide area as calculated from the phreatic surface (calculated in 'Surface' 8) until a depth of -150m with a porosity of 0.30 is displayed.

		Total volume of groundwater (m ³) till a depth of -150 m
June 2004	S ₀	30627781
July	S ₁	30659202
August	S ₂	30656882
September	S ₃	30682813
October	S ₄	30657607
November	S ₅	30738521
December	S ₆	30818349
January	S ₇	30884228
February	S ₈	30901364
March	S ₉	30950810
April	S ₁₀	30880942
May	S ₁₁	30870732
June	S ₁₂	30879801

Table 6.5 Volume of groundwater for the landslide area till a depth of -150 m.

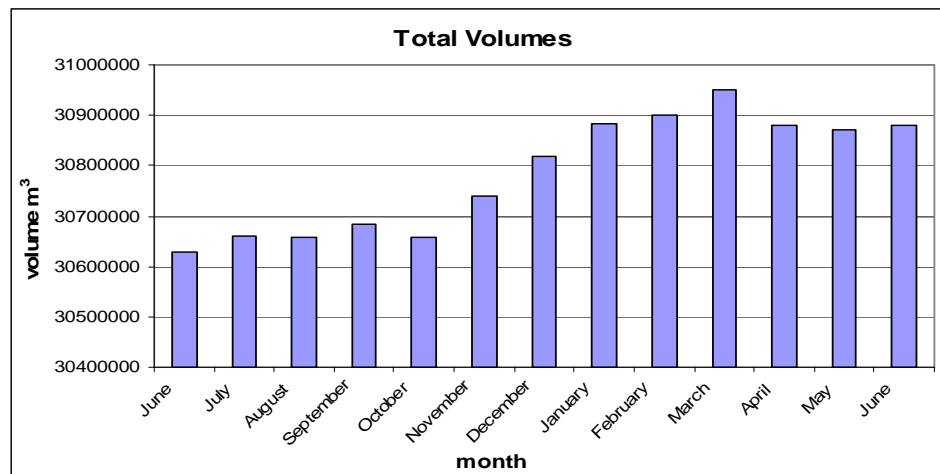


Figure 6.9 Total monthly groundwater storage volumes in 2004-2005 (cf. Table 6.5)

From graph 5.9 it can be derived that the rainfall is highest in February. However in Figure 6.9 the volume is highest in March. This is probably related to the time dependent process of flow from the surface to the groundwater level.

The monthly X-flow is derived from Equation 6.3.

$$X=D+ET+RO-R+\Delta Z$$

[Eq. 6.3]

In Figure 6.11 the Monthly average rates for rainfall (R), X-flow (X), evapotranspiration (ET), Run-off (RO) and dewatering (D) are illustrated. The rainfall and evapotranspiration rates are based on the average monthly rate from the daily recorded measurement. The dewatering is based on the average of the bi-monthly measurements. The X-flow is derived using Equation 6.3.

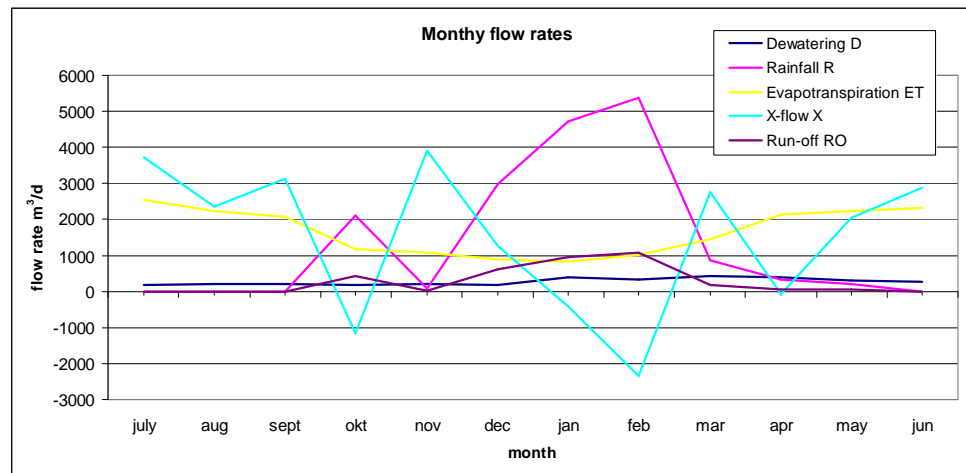


Figure 6.10 Monthly rates for rainfall, X-flow, evapotranspiration and dewatering in 2004-2005

In Figure 6.10 the inflow rates drop in three months below zero and thus suggesting negative X-flow and thus changes from inflow to outflow. This is not possible because an influx does not suddenly change to an outflux. Groundwater flow in such a large land mass does not suddenly change course from one moment to another. Moreover, a negative inflow also suggests that the groundwater flows away from the ocean.

The inflow should be relatively steady with time. Because, the inflow is calculated which Eq. [6.3], and the rainfall and evapotranspiration are fairly reliable (due to the high frequency of measuring data) and the dewatering and run-off play a minor role in the balance, the storage change is the main component influencing the X-flow. The storage change has an unreliability factor due to the many anomalies in measured groundwater level (see Table 6.1), the low frequency of measuring and the small number of measuring points.

The transport of rainwater from surface to groundwater level (GWL) is a transient process. Because the distance between surface and GWL is at some parts very large (50 to 150 m), the time for rain water to travel to the GWL can be long. Thus rainwater is probably stored in the unsaturated zone. This may also explain the negative inflow (see above), because the rainwater has not yet contributed to the storage. This is supported by Figures 5.9 and 6.9 where in February the rainfall is highest, but the storage is higher in the next month.

SWAP Calculation

Swap is a one dimensional numerical simulation for vertical flow through the unsaturated zone. The Darcy equation describes the water flow initiated by a gradient in soil water potential. For one-dimensional vertical flow the Darcy equation can be written as (Alterra Report):

$$q = -k(\phi) \frac{\partial(\phi + z)}{\partial z} \quad [6.4]$$

When considering the water balance of an infinitely small soil volume results in the continuity equation for soil water (Alterra Report):

$$\frac{\partial \theta}{\partial t} = \frac{\partial q}{\partial z} - S_a(\phi) - S_d(\phi) - S_m(\phi) \quad [6.5]$$

The soil water flow is calculated with Richards' equation, which follows from Eq. [6.4] and [6.5]:

$$\frac{\partial \theta}{\partial t} = \frac{\partial \left[k(\phi) \left(\frac{\partial \phi}{\partial z} + 1 \right) \right]}{\partial z} - S_a(\phi) - S_d(\phi) - S_m(\phi) \quad [6.6]$$

where:

$S_a(\phi)$ = soil water extraction rate by plant roots

$S_d(\phi)$ = extraction rate by drain discharge in saturated zone

$S_m(\phi)$ = exchange rate with macro pores

$k(\phi)$ = hydraulic conductivity

ϕ = pressure head

z = vertical coordinate

Infiltration

The infiltration rate of water into the unsaturated zone is high in the first few time steps. This is due to the high pressure gradient in the surface region (e.g. $\phi h(0)=0 < \phi h(z) < \phi h(0.01)$ for $0 < z < 0.01$ m), i.e. where the suction is high. This is illustrated in Figure 6.11.

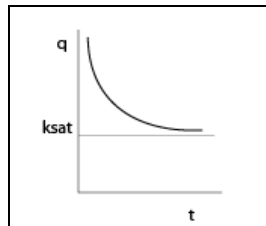


Figure 6.11 Infiltration rate of the soil adjacent to the surface

In the SWAP model the van Genuchten retention curve for the unsaturated zone is implemented as described in section 4.1. The parameters used in the calculations with the SWAP model for the unsaturated zone are specified in Table 6.6.

Parameter			Notes
g_n	4.0 (-)		Maximum value in SWAP
g_a	0.79 (1/m)		See Section
g_l	4.71 (-)		See Section
S_s	1 (-)	$\theta_s = 0.25$	Is equal with the porosity n
S_r	0.15 (-)	$\theta_r = 0.038$	θ_r is adjusted from 0.153 to achieve a more realistic S_r
$k_{y,sat}$	0.9 (m/d)		See Section 6.5.1

Table 6.6 Parameters for the unsaturated zone

In the SWAP model the Richards' equation is applied integrally for the unsaturated-saturated zone. It solves this equation numerically, using known relations between θ , ϕ and K . The implicit backward finite difference scheme, with explicit linearization of hydraulic conductivity, is used within SWAP to solve Eq. [6.4]. This results in an accurate mass balance and a rapid convergence will be achieved.

A calculation of a one-dimensional profile was performed for the sandstone layer. In this calculation the 'van Genuchten' parameters as specified in table 6.6 were used. The profile length is taken as the average distance between groundwater level and surface for the whole slide as derived with Surfer (see Section 6.4.1). The total length of the profile equals 50 m where the groundwater table is set at -42.5 m below the surface.

The daily rainfall and evapotranspiration were implemented for the period January 2004 – December 2005. For the bottom boundary a head of 7.5 m is prescribed. In Appendix 18 the SWAP data file is presented, which includes all the implementation data.

The distance between surface and groundwater level is long. For evaporation to occur the water needs to be close to the surface. The characteristics of the retention curve results in a shallow slope in the centre, which leads to reaching the residual water content at a depth of about 35 m, which is further elaborated in Chapter 7. Thus the evaporation can only occur when there is water infiltration into the region adjacent to the surface. To account for this aspect a maximum for the Darcy flux (cf. Equation 6.7) is included in the SWAP model according to:

$$E_{\max} = k^* \left(\frac{\phi_{atm} - \phi_1 - z_1}{z_1} \right) \quad [6.7]$$

where, k^* (m/d) is the average hydraulic conductivity between surface and first node, ϕ_{atm} (m) is the soil water pressure in equilibrium with the air relative humidity, ϕ_1 (m) is the soil water pressure head in the first node and z_1 (m) represents the soil depth to the first node. For accurate calculation of extreme hydraulic conditions, the node distance at the top ten centimetres should not be greater than 1 centimetre.

Figure 6.12 a graph of the water storage in the unsaturated zone is shown. From this graph it is evident that the infiltrated groundwater is stored in the unsaturated zone. The reduction in the amount of water stored in the unsaturated zone is due to evapotranspiration. Chapter 7 describes a sensitivity study pivoting the infiltration of rainwater into the unsaturated zone. The influence of increasing rainfall of the unsaturated zone profile is analyzed.

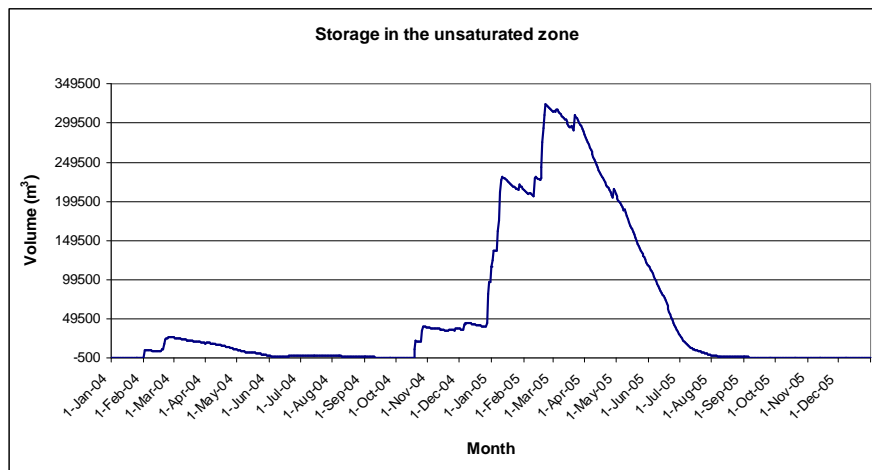


Figure 6.12 Storage in the unsaturated zone

In order to reach the same evapotranspiration as the reference evapotranspiration used in the water balance, calculations suggest that evapotranspiration by means of vegetation is required (i.e. transpiration by extraction via plant roots). However, the actual role of vegetation is yet unclear and should be subject of further investigation. In the following, the actual transpiration is considered to be close to reference evapotranspiration. To this end, the crop parameters in the SWAP model are adjusted. This means that the transpiration lies between 90-99 % of the reference evapotranspiration for period December 2004 – June 2005 which is considered in the simulation discussed in Chapter 7. In general it holds that the difference between reference evapotranspiration and actual evapotranspiration is largest for the dry periods with limited water in the soil.

In Figure 6.10 the unsaturated zone storage significantly increases in the wet months. When the evapotranspiration becomes dominant in April the storage decreases until August when no water is left in the unsaturated zone. Thus the evapotranspiration can only occur when there is water in the unsaturated zone. Therefore the evapotranspiration in the dry months cannot be as high in the dry months as illustrated in Figure 6.10. The evapotranspiration can only be so high if the soil would be irrigated.

The x-flow component in the water balance governs the unknown net flow. This unknown net flow also includes water infiltrating by irrigation, by septic tanks and other means. This additional water infiltrating the soil can locally add to the water in the unsaturated zone.

6.5. Soil/Rock properties

The permeability and the strength of the rock and soil are the most important parameters of the slide. From geological descriptions, cross-sections, groundwater levels and known stable conditions these parameters will be determined in this section. In addition, the influence of groundwater level change and shear zone thickness will be investigated.

6.5.1. Permeability

For deriving the permeability of the different rock types, the steady state situation of the month June 2004 is evaluated. The mean groundwater level of this month is calculated in Surfer according Section 6.4.1. The permeability's were estimated from the geological description of the BRM and the cross-section D-D' in Appendices 14 and 7, respectively, in combination with in literature available typical values (*Fitts, 2002*). In cross-section D-D' the orientation of the strata is also shown. Therefore, the following can be derived from this cross-section:

- Sandstone Tt is mainly horizontally layered and has thus a higher permeability in horizontal directions (x-, z-direction).
- Sandstone Ts has in the middle horizontally oriented strata and in the lower and left part a more vertically oriented strata. Thus in the horizontally orientated part the permeability is higher in the horizontal directions (x-, z-direction) and in the vertically oriented part the permeability is higher in the vertical directions (y-direction)

Because the rock in the shear zone is assumed to be disintegrated, the permeability in this zone is larger in comparison with the surrounding rock. This has a great effect on the groundwater flow. Later in this section this will be further elaborated.

For the initial phase, a steady state calculation was performed. On the left ocean side boundary and on the 'hill'-side boundary the phreatic head is set as a condition. The phreatic head on the left boundary is the ocean level and therefore stationary at 150 m (given that the lower boundary is positioned 150 m below ocean-level and excluding tidal changes).

The phreatic head on the 'hill'-side boundary is initially determined at 316m MSL with SURFER 8 calculations. However, this value derived for phreatic head is positioned in the middle of the basalt layer. The groundwater measuring point closest to this boundary is SP-26, which is approximately 160 m from the 'hill'-side boundary. The level measured in SP-26 corresponds with the in SURFER 8 derived value for the phreatic head. The phreatic head is increased from 317 to 325 m, because there is a long distance between the reference point SP-26 and the hill side boundary with an inclined impermeable basalt layer in between.

From the initial flow calculations the permeability properties have been derived. This process involved the following steps:

- Determine the initial conductivity from literature and geological descriptions.
- Calculate the groundwater level for the initial phase.
- Alter the conductivity to suit the derived groundwater level in Surfer.
- Then repeat the calculations to determine the new conductivities leading to better results.
- Repeat this procedure until a good fit is achieved.

Note that the standard deviation in Surfer is high and that there are unexplained high peaks. Therefore a good fit does not necessarily have to be exactly along the in surfer calculated ground water level line. In Table 6.7 the hydraulic conductivities derived from this process are shown. In Figure 6.13 the formations as modelled in Plaxis are shown. In Table 6.8 some typical conductivity values are presented. These values correspond reasonably well with the values in Table 6.7. The difference in conductivity in vertical and horizontal direction is due to the direction of the strata. Conductivity in the lowest sandstone formation (Sandstone Tt) is lower than in the other sandstone formations. This difference in conductivities is probably caused by the depth of the Sandstone Tt layer. Porosity and conductivity decreases with depth due to the lithofication process of sandstone.

Formation	k_x m/d	k_y m/d
Sandstone Tt	0.15	0.13
Sandstone Ts hor	0.2	0.12
Sandstone Ts ver	0.08	0.1
Basalt	10^{-4}	10^{-4}
Siltstone	10^{-6}	10^{-6}
Shear zone down slope (DS)	2.0	2.0
Shear zone main (M)	1.2	1.2
Shear zone DS + M	2.0	2.0
Landslide debris	2.0	2.0
Very weathered rock	1.0	1.0

Table 6.7 Determined permeability's corresponds with Figure 6.14.

Material	k (m/day)
Sandstone	10^{-5} to 1
Fractured Basalt	10^{-2} to 1000
Igneous and metamorphic rock	10^{-8} to 1
shale	10^{-11} to 10^{-5}

Table 6.8 Typical permeability values (Fitts, 2002).

Note I: Headscarp slide has other landslide debris indication. The conductivity parameters are considered the same as the other landslide debris parameters. However, the strength parameters are taken equal to those of the sandstone Tt to avoid that the Headscarp slide takes part into this evaluation.

Note II: The landslide debris zone is at the toe extended to the left side boundary. This is done to account for the beach, which is located there. The extended zone is at the left side 10 m thick. In cross-section D-D' in Appendix 7 a debris zone along a fault line is located in the same area.

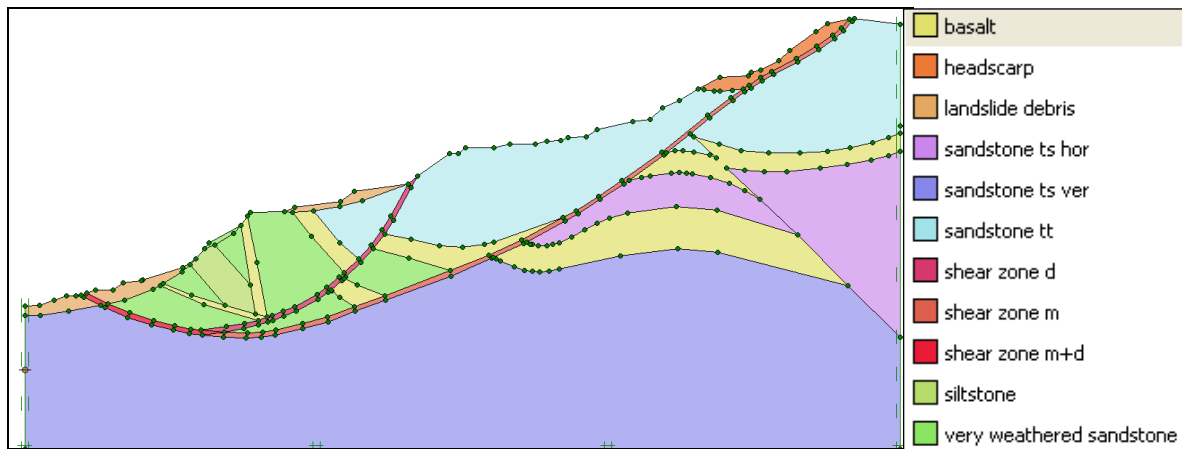


Figure 6.13 Plaxis geometry and formations

Figure 6.14 to 6.17 represent the steady state saturation calculations for the formation permeability's as given in Table 6.7 for different situations.

In case no shear zone is presented, see Figure 6.15.

Groundwater accumulates on top of basalt layers and causes the saturation to be too high in the middle part of the slope. This is in contrast with the mean groundwater level of 2003-2004 determined in 'Surfer'. This groundwater level is also displayed in Figure 6.15.

A shear zone of which the location is known (cf. Figure 6.2) is also introduced; see Figure 6.16.

In this layer the sandstone is assumed to be disintegrated due to shearing of the rock. Therefore, the permeability in this zone is higher than in the surrounding rock. The corresponding saturation profile of the 4 m thick shear zone is displayed in Figure 6.16. The flow pattern changes drastically due to the introduction of the shear zone in the geometry. The shear zone acts as a drain for the water that otherwise would have accumulated on top of the basalt layers as illustrated in Figure 6.15. The saturation level gives now a better fit to the groundwater level line calculated with 'Surfer' (see Section 6.4.1). However, at the lower part of the slope the saturation level is still too high, in comparison with the mean groundwater level of 2003-2004 determined in 'Surfer'. This groundwater level is also displayed in Figure 6.16.

By introducing very weathered sandstone in the lower part of the slope the saturation level gives a better fit to the with 'Surfer' calculated groundwater level. In Figure 6.16 and 6.17 these results for a 3 and 4 m thick shear zone are presented. Comparing the results for a 3 and 4 m shear zone situation, it follows that the saturation level derived for the 4 m thick shear zone gives a better fit to the groundwater line obtained with 'Surfer'.

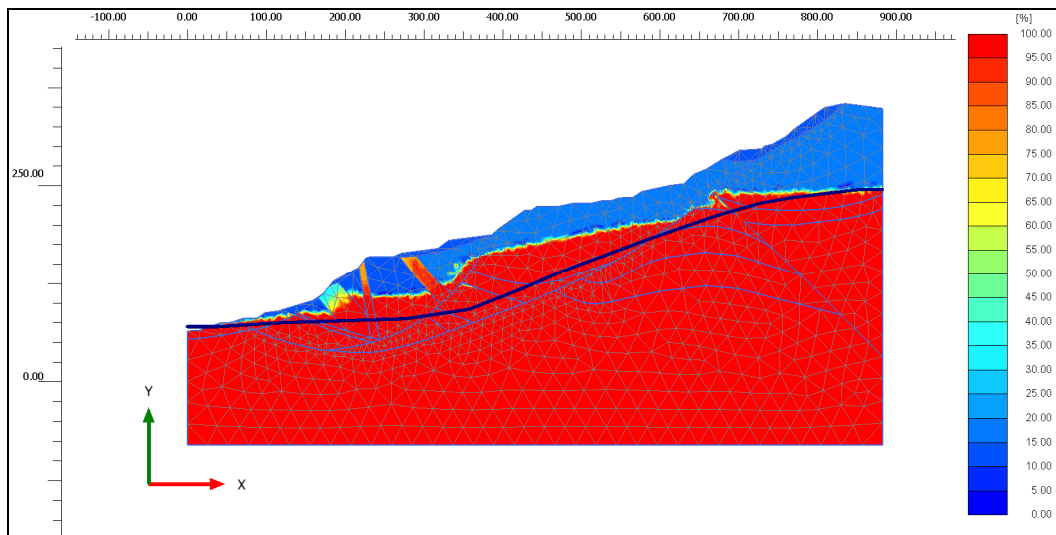


Figure 6.14 Saturation profile for no shear zone.

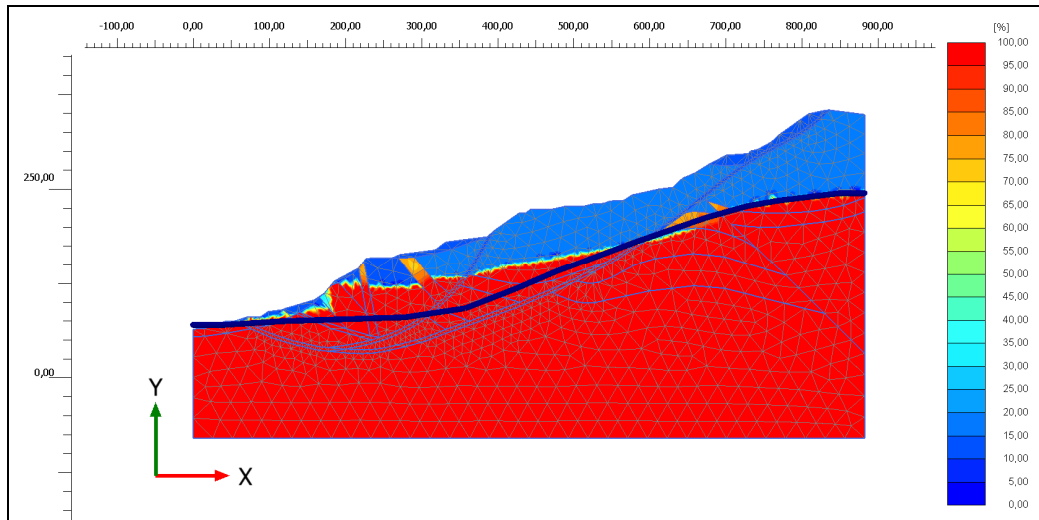


Figure 6.15 Saturation profile for a 4 m thick shear zone.

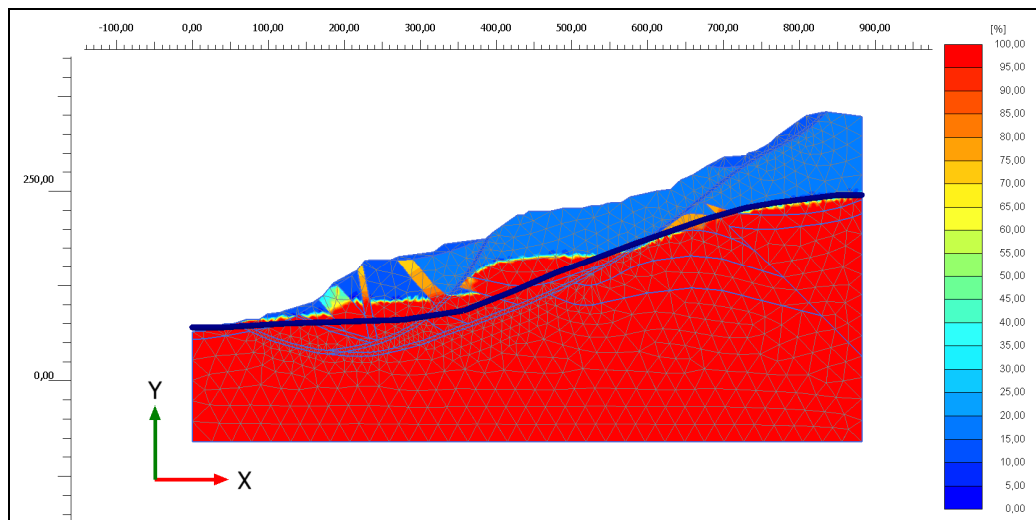


Figure 6.16 Saturation profile for a 4 m thick shear zone with very weathered rock at the lower slope.

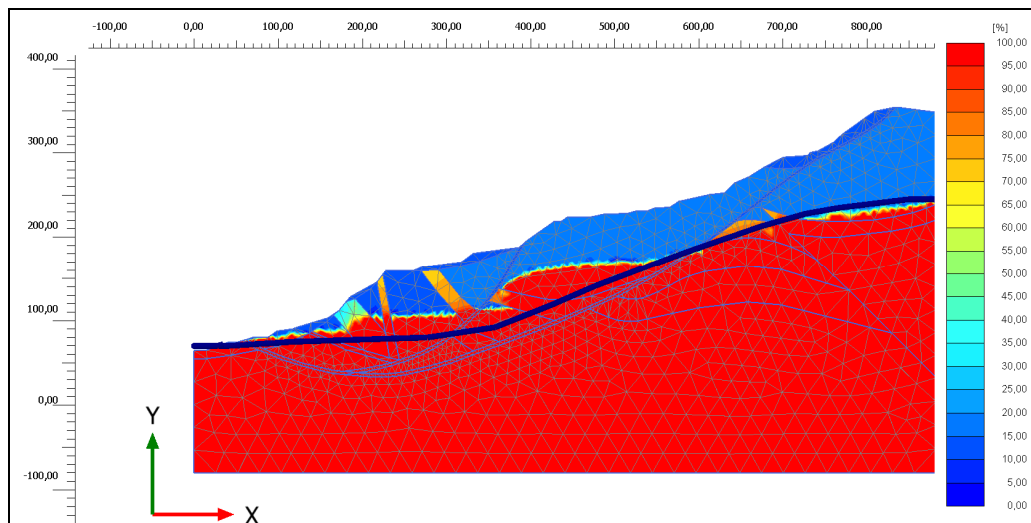


Figure 6.17 Saturation profile for a 3 m thick shear zone with very weathered rock at the lower slope.

Even though the introduction of the shear zone and the very weathered sandstone comes close to the in 'Surfer' derived groundwater level, there are still some discrepancies. Therefore, the parameters were reviewed and some changes were made:

- Three different types of Basalt layers are introduced with different permeability's. The difference in permeability can be accounted for by the degree of weathering.
- The shear zone of the main slide is divided into two sections with slightly different permeability. This may be due to the amount of small grain material in the zone.
- An extra layer is introduced below the shear zone in the lower part of the slide. The reason that the permeability in this layer can be higher may be due to fault near this location, See Appendix 7.

This results in the geometry as shown in Figure 6.18 and the corresponding permeability's are listed in Table 6.8. In Figure 6.19 the result of a steady state calculation is displayed for the geometry presented in Figure 6.18 and the permeability's listed in Table 6.8. The result gives an almost perfect fit to the in Surfer derived groundwater level.

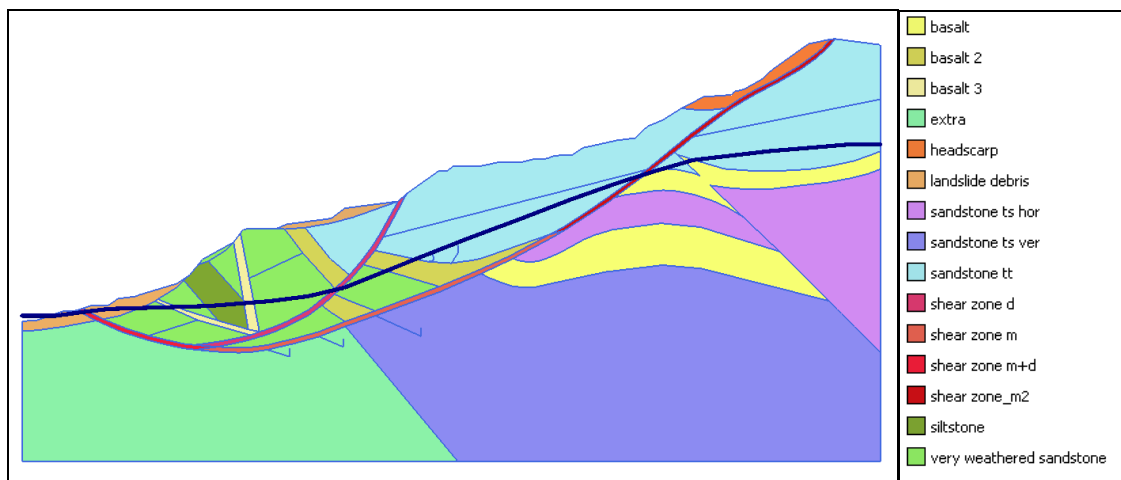


Figure 6.18 Plaxis geometry and formations

Formation	k_x m/d	k_y m/d
Sandstone Tt	0.9	0.9
Sandstone Ts hor	1.0	0.9
Sandstone Ts ver	0.6	0.5
Basalt	10^{-4}	10^{-4}
Basalt 2	0.1	0.1
Basalt 3	1.0	1.0
Siltstone	10^{-4}	10^{-4}
Shear zone down slope (D)	2.5	2.5
Shear zone main (M)	2.0	2.0
Shear zone D + M	2.0	2.5
Shear zone main (M2)	1.0	1.0
Landslide debris	3.0	3.0
Headscarp	3.0	3.0
Extra	4.0	4.0
Very weathered rock	1.5	1.5

Table 6.8 Determined permeability's corresponding to Figure 6.18

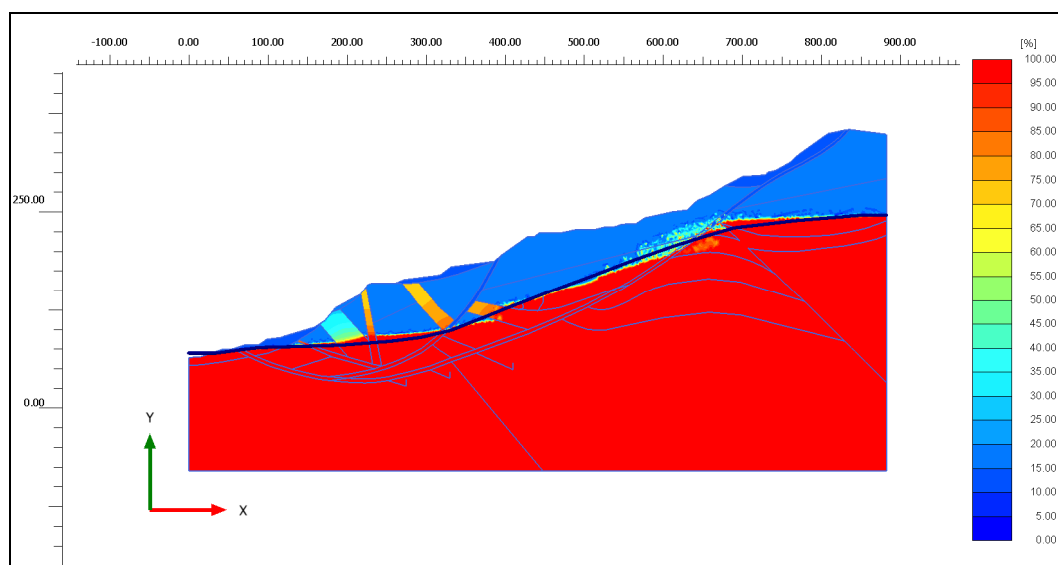


Figure 6.19 Saturation profile for the geometry of Figure 6.18 and permeability's of Table 6.8

Porosity

The porosity (n) is the fraction of pores in the total volume. The void ratio (e) is related to the porosity by:

$$e = \frac{n}{1-n} \quad [6.8]$$

In sedimentary rocks the porosity varies between close to 0 to as high as 90%. In these rocks, porosity generally decreases with age and depth (Goodman 1989).

Some volcanic rocks can have high porosity's due to volcanic gas bubbles in the rock. Generally igneous rock has very low porosity (between 1 or 2%), a large portion of the pore space belongs to fissures. When the weathering of the rock formation increases, the fissures form cracks and the porosity also increases.

As a reference for determining the rock porosities, the tables in Appendix 15 have been used.

The sandstone is at or fairly close to the surface and relatively young (compared to the sandstone formations in the tables in Appendix 16). Therefore, the porosity for both sandstone formations (Tt and Ts) is assumed to be 25%.

Since basalt is assumed to be generally intact with some fissures and cracks, thus slightly weathered, its porosity is estimated at 5%.

Considering the pore structure of siltstone, its porosity is estimated at 25%.

The porosity of the landslide debris and very weathered sandstone is assumed to be comparable to sand and is therefore estimated at 40%. Also the porosity of the shear zone where the rock is assumed to be disintegrated, due to passed movement, the porosity is estimated at 40%.

Formation	n	e
Sandstone	0.25	0.33
Basalt	0.05	0.05
Siltstone	0.25	0.33
Very weathered rock	0.40	0.67
Shear zone	0.40	0.67
Landslide debris	0.40	0.67

Table 6.9 Porosity and void ratio for the formations.

6.5.2. Strength

For determining the strength parameters, the program Roclab (www.roclab.com) is used. Roclab uses the Hoek and Brown criterion (Hoek, 2002), which is translated to Mohr-Coulomb properties. From the geological descriptions of the formations and the cross-section D-D' in Appendices 16 and 7, respectively the observation parameters can be determined. The model was analyzed in Plaxis 9.

Derivation of the strength properties

The Hoek-Brown criterion was developed to link the geological observations to a failure envelope.

The generalized Hoek-Brown criterion reads:

$$\sigma_1' = \sigma_3' + \sigma_{ci} \left(m_b \frac{\sigma_3'}{\sigma_{ci}} + l_r \right)^{a_r} \quad [6.9]$$

with:

$$m_b = m_i \exp \left(\frac{GSI - 100}{28 - 14D_d} \right) \quad [6.10]$$

$$l_r = \exp \left(\frac{GSI - 100}{9 - 3D_d} \right) \quad [6.11]$$

$$a_r = \frac{1}{2} + \frac{1}{6} \left(e^{\frac{GSI}{15}} - e^{\frac{20}{3}} \right) \quad [6.12]$$

where:

- σ_{ci} = uniaxial compressive strength of intact rock material
- σ_3' = minor principal stress (confining pressure) at failure
- σ_1' = major principal stress at failure
- GSI = Geological strength index, which is based on structure and surface conditions
- D_d = disturbance factor (tunnelling, excavation, etc.) No disturbance D=0
- l_r, a_r, m_b = material constant, where $l_r = 1$ for intact rock

Since there is no disturbance in the area due to excavating or tunnelling, the disturbance factor D can be considered zero.

The Rock mass stiffness modulus of deformation follows from:

$$E_m = E_i \left(0,02 + \frac{1 - D / 2}{1 + e^{((60 + 15D - GSI) / 11)}} \right) \quad [6.13]$$

$$E_i = MR \cdot \sigma_{ci}$$

where:

- E_i = Intact rock modulus
- MR = modulus reduction factor

In Table 6.10 the values entered in Roclab for uniaxial strength, GSI, m_i (material constant) and modulus reduction factor (MR) are presented. With these values the Mohr-Coulomb strength parameters and the rock mass modulus can be calculated. The calculated Mohr-Coulomb strength parameters and the rock mass modulus are presented in Table 6.11.

Names	Parameter	Sandstone	Basalt	Siltstone	Very weathered sandstone	Shear zone
Uniaxial compressive strength	σ_{ci} (MPa)	70	175	35	65	3
Geological strength index	GSI (-)	45	70	20	34	20
Material parameter	m_i (-)	5	6	7	5	5
Stiffness index	MR (-)	200	275	300	200	200

Table 6.10 Roclab observation parameters.

Translation to Mohr-Coulomb parameters is obtained with Equations 6.14 and 6.15. The results for the different formation are shown in Table 6.11.

$$c = \frac{\sigma_{ci} \left[(1 + 2a_r)s + (1 - a)m_b \sigma'_{3n} \right] (l_r + m_b \sigma'_{3n})^{a-1}}{(1 + a_r)(2 + a_r) \sqrt{1 + (6am_b(l_r + m_b \sigma'_{3n})^{a-1}) / (1 + a_r)(2 + a_r)}} \quad [6.14]$$

where:

$$\sigma'_{3n} = \frac{\sigma'_{3\max}}{\sigma_{ci}} \quad [6.15]$$

$\sigma'_{3\max}$ = the upper limit of confining stress over which the relationship between Hoek-Brown and the Mohr-Coulomb criteria is considered.

$$\phi = \sin^{-1} \left[\frac{6am_b(s + m_b \sigma'_{3n})^{a-1}}{2(1 + a)(2 + a) + 6am_b(s + m_b \sigma'_{3n})^{a-1}} \right] \quad [6.16]$$

As illustrated with Eq. 6.14 and 6.16 the confining stress $\sigma'_{3\max}$ is important for the determination of the Mohr-Coulomb parameters.

$\sigma'_{3\max}$ is estimated to calibrate a good fit between the Hoek and Brown and Mohr-Coulomb curve. In Figure 6.18 the distribution of $\sigma'_{3\max}$ for plane strain conditions is shown. The lowest sandstone layer has the highest $\sigma'_{3\max}$. The shear zone of the main slide can be divided into two sections: an upper and lower part. Also the Basalt layers can be divided into two sections: a left and right part. The right part has in this case the highest $\sigma'_{3\max}$. In table 6.11 the average $\sigma'_{3\max}$ values assigned to the different layers are listed.

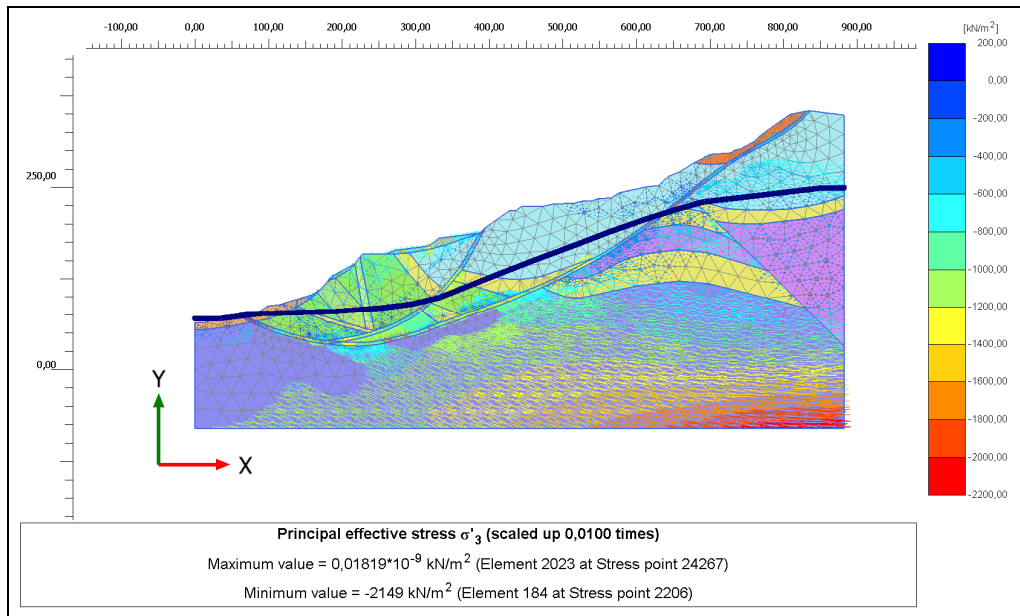


Figure 6.20 The distribution of $\sigma'_{3\max}$ for plane strain conditions.

From Figure 6.20 the value for $\sigma'_{3\max}$ can be assigned to the different layers. The different layers are illustrated in Figure 6.21.

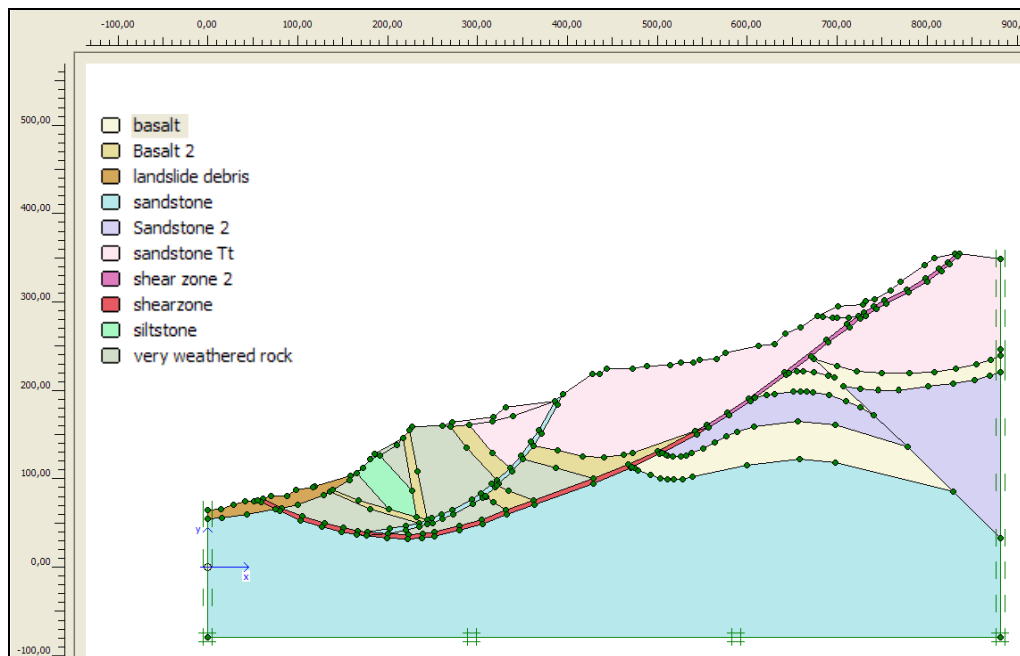


Figure 6.21 Different layers in the strength calculation

By implementing the different parameters (see above) in Roclab, the Mohr-Coulomb criteria can be derived with Eqs. 6.14 and 6.15. In table 6.11, the values for $\sigma'_{3\max}$ and derived Mohr-Coulomb parameters are presented for the different layers.

Parameter	Sand stone	Sand stone 2 + Tt	Basalt	Basalt 2	Silt stone	Very weathered sandstone	Shear zone 2	Shear zone
$\sigma'_{3\max}$ (KPa)	1550	750	600	1250	850	800	500	1000
c (KPa)	712	569	5631	5652	172	346	48	75
ϕ (°)	42	47	53	51	35	43	19	15

Table 6.11 Values derived for $\sigma'_{3\max}$, c and ϕ

In Figure 6.22a and b, the Hoek-Brown and Mohr-Coulomb failure envelope is displayed for Sandstone. The Graphs for the other formations are shown in Appendix 17.

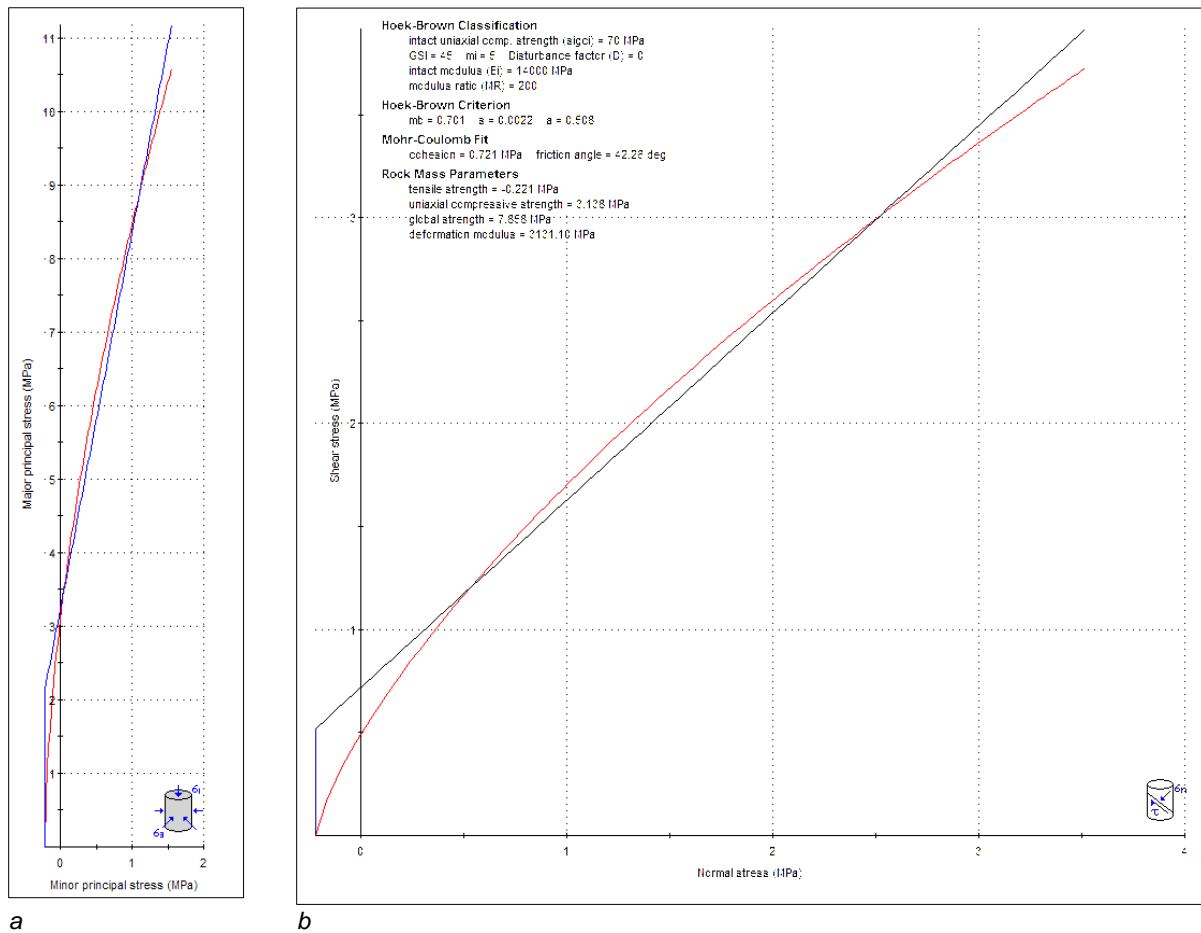


Figure 6.22 a) Major and minor principal stress, b) Shear and normal stress. Formation Sandstone; Red is Hoek-Brown, Blue Mohr-Coulomb (Roclab).

At a certain stress level cracks will begin to form and the bulk volume increases. This increase in volume associated with cracking is termed dilatancy (Goodman, 1989). In this study the rock mass is modelled as a continuum and will not include crack forming. Therefore the dilatancy for rock is ignored.

Plaxis c/phi reduction calculation

The stability of the BRM for upper and lower groundwater levels (see Section 6.4.1) is analyzed with a c/phi reduction calculation in Plaxis. In this case, the shear zone is assumed to be 4 m thick. The safety factor, which is determined according to Eq. 6.17 (*Plaxis 9 manual*), will have to approach 1 for the upper groundwater level. By manual iteration of the strength properties (also verified with Roclab) the properties shown in Table 6.12 have been determined. The landslide debris layers are assumed as sandy layers with little silt. The parameters for the landslide debris layer have been based on NEN6740.

$$\sum M_{sf} = \frac{\tan \phi_{input}}{\tan \phi_{reduced}} = \frac{c_{input}}{c_{reduced}} \quad [6.17]$$

$$SF = \sum M_{sf} \text{ at failure}$$

Parameter	Sand stone	Sand stone 2 + Tt	Basalt	Basalt 2	Silt stone	Very weathered rock	Shear zone 2	Shear zone	Land slide debris
γ_{dry} (kN/m ²)	22	22	27	27	19	22	21	21	18
γ_{sat} (kN./m ²)	23	23	27	27	20	23	22	22	20
ν (-)	0.30	0.30	0.32	0.32	0.29	0.30	0.30	0.30	0.30
c (kPa)	700	600	6000	6000	170	350	30	60	5
ϕ (°)	42	47	53	51	35	40	21	19	32
E_{rm} (kPa)	1.5E6	1.5E6	6.6E6	6.6E6	4.5E5	1.0E6	2.5E5	2.5E5	2.5E4

Table 6.12 Determined Properties γ_{dry} , γ_{sat} and ν for the rock formations based on Goodman 1989, Landslide debris parameters based on NEN6740.

The rock mass stiffness E_{rm} was adjusted such that the displacement is minimal when the factor of safety slightly decreases. This is done because the displacements measured of the BRM are small.

In order to analyze the Down slope slide and the Main slide separately, the shear zone is divided into sections. When analyzing the Main slide, the section of the Down slope slide is given the material data set of sandstone and visa versa. In Figure 6.21 the geometry of the generated mesh is displayed for the analysis of the Main slide and the Down slope slide.

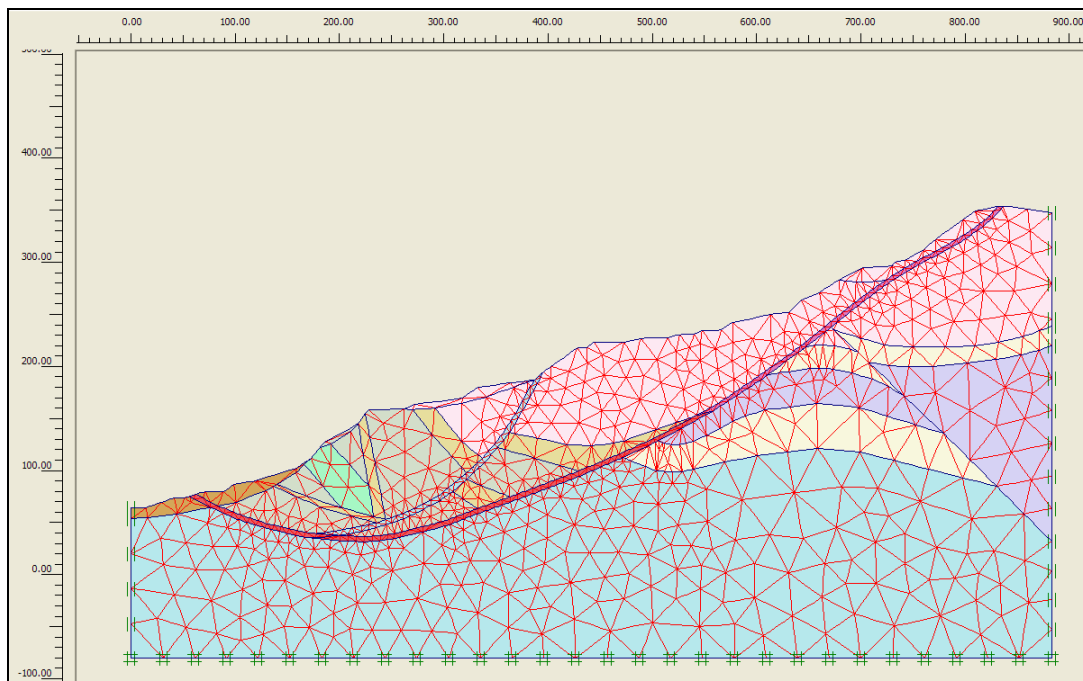


Figure 6.23 the geometry for the analysis of the main slide and the Down slope slide. (Plaxis 9)

In reality the transition from sandstone and basalt layers to the disintegrated rock in the shear zone is smoother. The rock close to the shear zone is usually more fractured than rock further from this zone.

Thickness shear zone

The thickness of the layer of disintegrated rock of the shear zone influences not only the groundwater flow, but also the stability of the slide. To analyze the influence of the shear zone thickness on the main and down slope slide, a shear zone of 3 and 4 meters has been evaluated with the c/phi reduction method and the material properties as in Table 6.12. The thickness of the layer has been increased downwards. The calculations for all shear zone thicknesses are done for upper boundary groundwater levels and with hydrostatic pore pressures. This gives a first impression of the slope stability and allows to verify the parameters derived in this Chapter. In Figure 6.24 the generated pore pressures are presented for the upper boundary. In Figure 6.25 a and b the results are presented in a Safety factor (Sum-Msf) against the calculation step, for the main slide and down slope slide, respectively.

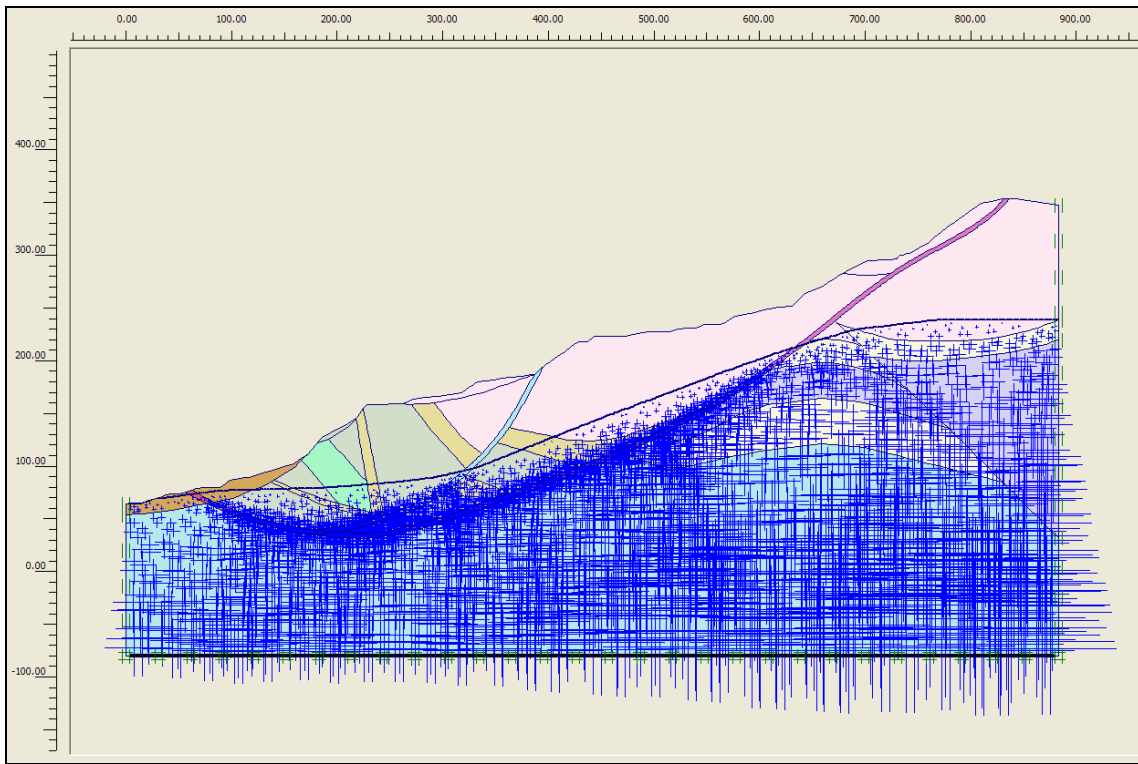


Figure 6.24 The generated pore pressures are presented for the upper boundary. (Plaxis 9)

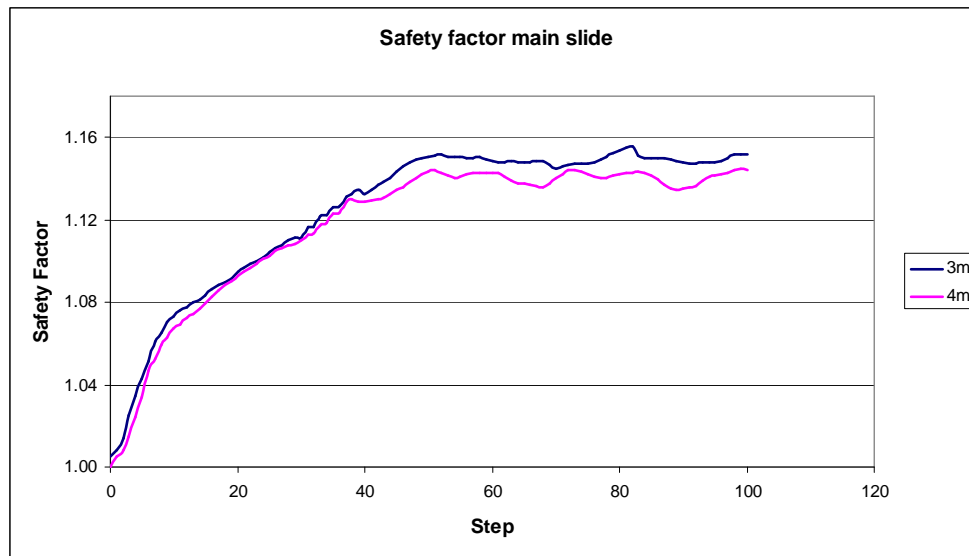


Figure 6.25a Influence of shear zone thickness on the safety factor of the main slide. Blue is 4 m and red 3 m. (Plaxis 9)

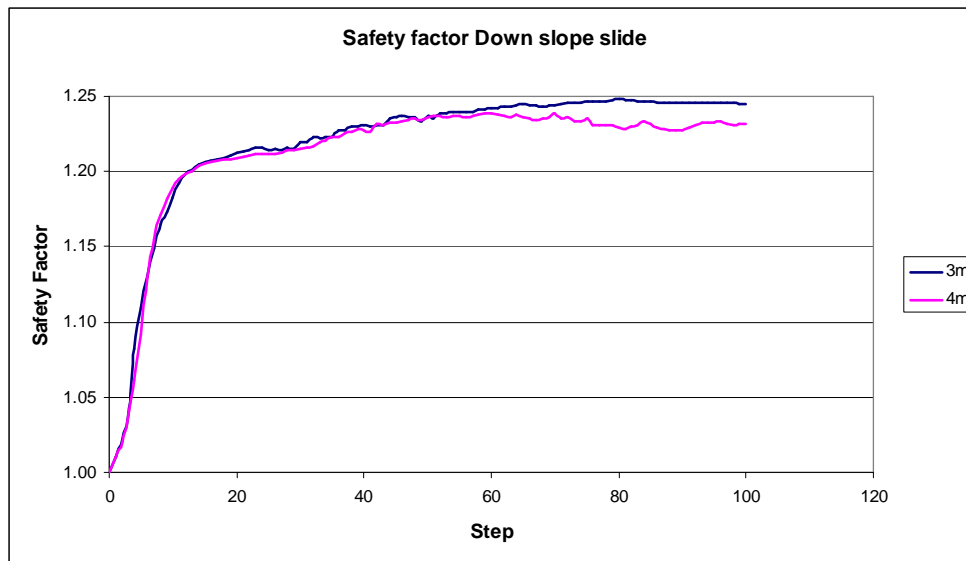


Figure 6.25b Influence of shear zone thickness on the safety factor of the down slope slide. Blue is 4m and red 3m.(Plaxis 9)

For the main slide, where the thickness of the zone varies between 3 and 4m, the safety factor equals 1.15 to 1.14, respectively; see Figure 6.25a. Similarly, for the down slope slide where the thickness of the zone varies between 3 and 4m, the safety factor equals 1.24 to 1.23, respectively; see Figure 6.25b. Thus, the main slide is less stable than the down slope slide.

Upper and lower groundwater levels

In Section 6.4.2 the upper and lower groundwater levels of the data set was determined. The stability of the main and down slope slide under these two levels with hydrostatic pore pressures has been analyzed with the c/phi reduction method in Plaxis.

The calculations was executed for the material properties according to Table 6.12 and for a shear zone of 4 m thick. In Figure 6.26a and b the results are presented in a Safety factor (Sum-Msf) against the calculation step, for the main slide and down slope slide, respectively.

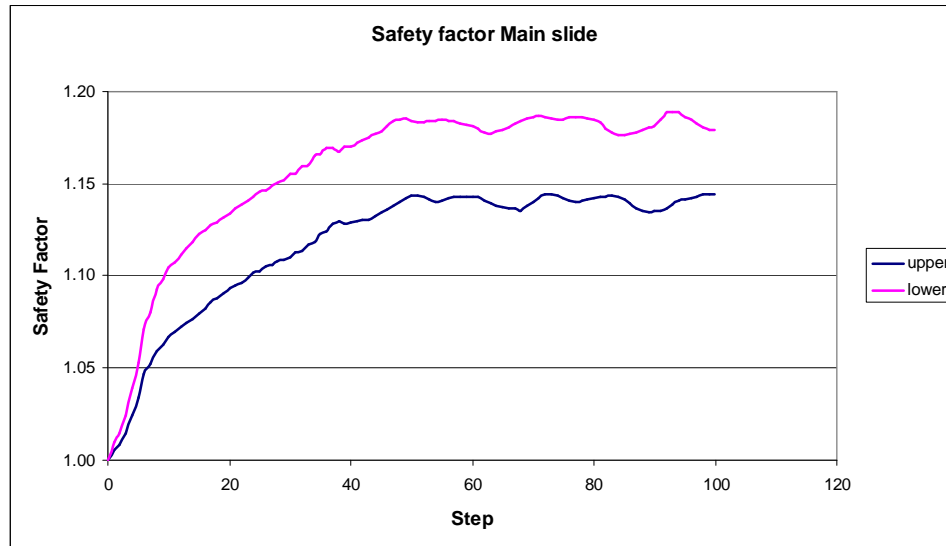


Figure 6.26a Influence of Groundwater level of safety factor for the main slide. Red is lower boundary, blue is upper boundary (Plaxis 9)

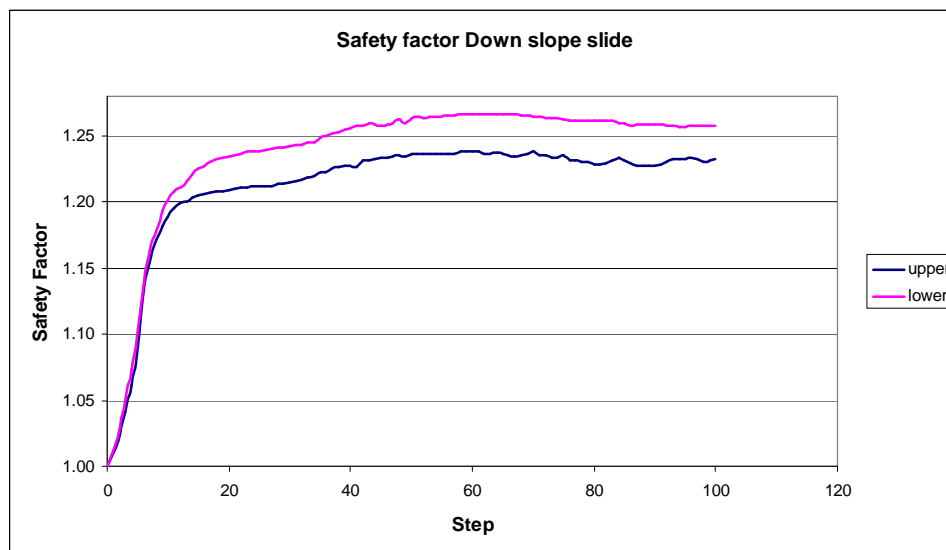


Figure 6.26b Influence of Groundwater level of safety factor for the Down slope slide. Red is lower boundary, blue is upper boundary. (Plaxis 9)

The safety factors for the main slide in Figure 6.26a are 1.18 for the lower boundary, 1.14 for the upper boundary. The safety factor for the down slope side is 1.27 for the lower boundary, 1.23 for the upper boundary (see Figure 6.26b). Thus, the main and down slope slide experiences equal influence of the above mentioned groundwater level differences. However, a groundwater rise from lower to upper has much more influence than an increase in shear zone thickness from 3 to 4 meters. (cf. Figures 6.25 a and b)

For the sensitivity study only the stability of the main slide will be investigated.

6.6. Final model geometry

In Sections 6.5.1 and 6.5.2 the permeability and strength properties of the different formations of the BRM were investigated. In Figure 6.28, the geometry with all the formations is displayed. In Table 6.13 the in this Chapter derived properties of those formations are listed. These properties will be used in the sensitivity study that will be described in the next chapter.

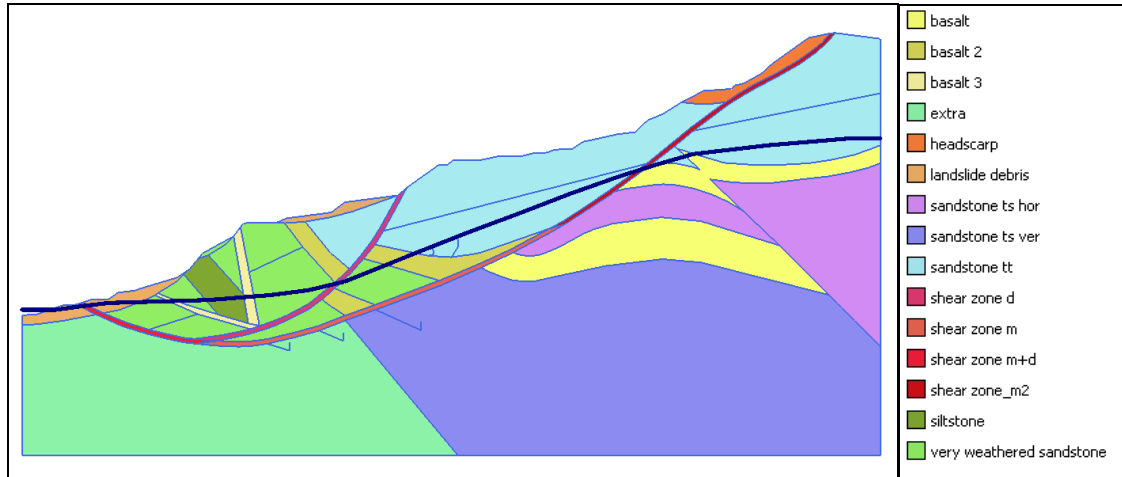


Figure 6.28 Plaxis geometry and formations

Formation	k_x (m/d)	k_y (m/d)	c (kPa)	ϕ (°)	ν (-)	E (kPa)
Sandstone Tt	0.9	0.9	600	47	0.30	1.5E6
Sandstone Ts hor	1.0	0.9	600	47	0.30	1.5E6
Sandstone Ts ver	0.6	0.5	700	42	0.30	1.5E6
Basalt	10^{-4}	10^{-4}	6000	53	0.32	6.6E6
Basalt 2	0.1	0.1	6000	51	0.32	6.6E6
Basalt 3	1.0	1.0	6000	51	0.32	6.6E6
Siltstone	10^{-4}	10^{-4}	170	35	0.29	4.5E5
Shear zone down slope (D)	2.5	2.5	600	47	0.30	1.5E6
Shear zone main (M)	2.0	2.0	60	19	0.30	2.5E5
Shear zone main (M2)	1.0	1.1	30	21	0.30	2.5E5
Shear zone D + M	2.0	2.5	60	19	0.30	2.5E5
Landslide debris	3.0	3.0	5	32	0.30	1.0E6
Head scarp	3.0	3.0	600	47	0.30	1.5E6
extra	4.0	4.0	700	42	0.30	1.5E6
Very weathered rock	1.5	1.5	350	40	0.30	1.0E6

Table 6.13 Properties of the in Figure 6.23 displayed formations, corresponding to tables 6.8 and 6.11.

7. Sensitivity study

A sensitivity study was performed comprising a variation of the rainfall data and the retention curve on the water content and pressure distribution of the unsaturated zone for the Big Rock Mesa landslide. Besides that, the effect of mesh selection in Plaxis was evaluated. The infiltration of rainwater in the unsaturated zone was investigated with Plaxis and compared with SWAP. Also the influence of rising groundwater level on the stability of the BRM slide was studied with Plaxis. Finally some remedial measures will be discussed.

7.1. Water flow through the unsaturated zone

For the vertical one-dimensional flow of water through the unsaturated zone, a column was considered with a height of 50 m and a groundwater level of 7.5 m. This corresponds with the average height of the unsaturated zone derived with 'Surfer'. Both SWAP and Plaxis were used to analyse the water flow through the unsaturated zone. These column dimensions were used in all the analyses presented in this Chapter. The period December 2004 – June 2005 was simulated. All the data used concerning the daily rainfall, reference evapotranspiration, hydrauger output and run-off are displayed in Appendix 19. Both SWAP and Plaxis employ the Richards equation for water flow through an unsaturated zone, see Section 6.4.4. However, Plaxis does not include the extraction rate by plant roots, drain discharge or exchange with macro pores. In SWAP the evapotranspiration entered, is limited by the maximum evapotranspiration depending on the water content near the surface (see Section 6.4.4). The evapotranspiration in Plaxis is simulated by an out-flux at the top boundary. In dry conditions the suction can be high in order to accommodate the water flux.

Plaxis is a finite element model that is described in Chapter 5. For the flow through the unsaturated zone no coupled analysis is used only the flow part of the matrix equation [5.42].

The project settings in Plaxis were as follows:

- The width of the column is set to 0.5 m in order to arrive at a fine enough mesh with minimum amount of total elements.
- The side boundaries are closed to exclude horizontal flow.
- The lower boundary has a prescribed head of 7.5 m.
- At the top boundary the effective daily rainfall is entered. The effective rainfall is derived from the daily rainfall minus the daily average hydrauger production, run-off and the evapotranspiration.
- 15-node elements.

SWAP is a discrete model created for analysis for the unsaturated zone with application to agriculture. The project settings of SWAP were similar to those described in Section 6.4.4. The daily rainfall and evapotranspiration were entered separately.

As mentioned in Section 6.4 the evaporation is small due to the lack of water near the surface. In SWAP a limitation on the evaporation is added, based on the Darcy flux, see Equation 6.4. In order to reach the same evapotranspiration as the reference evapotranspiration used in the water balance and Plaxis, the actual transpiration was taken close to the reference evapotranspiration. This implies that the extraction of water occurs via vegetation with a maximum root depth of 10 m. For the period considered here, the reference evapotranspiration was reached to about 90 to 99%.

The hydraulic permeability and the 'van Genuchten' parameters included in the analysis are presented in Table. 7.1. The corresponding retention curve for these parameters is shown in Figure 7.1.

Parameter			Notes
g_n	4.0 (-)		Maximum value in SWAP
g_a	0.79 (1/m)		See Section
g_l	4.71 (-)		See Section
S_s	1 (-)	$\theta_{sat}=0.25$	Is equal with the porosity n
S_r	0.15 (-)	$\theta_{res}=0.038$	θ_{res} is adjusted from 0.153 to achieve a more realistic S_{res}
$k_{rel;y}$	0.9 (m/d)		See Section 6.5.1.

Table 7.1 The 'van Genuchten' parameters used in the study.

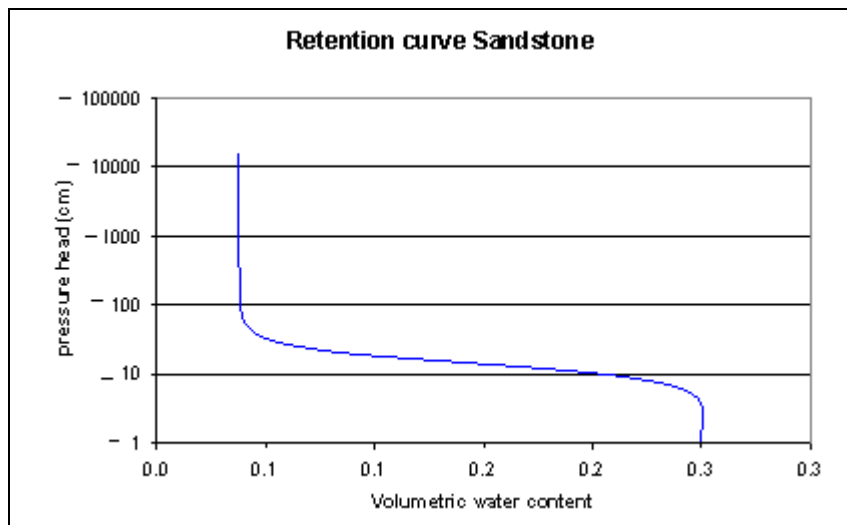


Figure 7.1. Retention curve for the parameters in Table 7.1.

7.1.1. Mesh selection Plaxis

In order to simulate correctly the infiltration of rainwater and flow through the unsaturated zone, a fine enough mesh had to be selected. For the period December 2004 - January 2005 three meshes with different average element height (EH) were used. In Figures 7.2 a, b and c the saturation levels are displayed for EH = 2.38, 0.82 and 0.20 m, respectively. The width of the column was adjusted to limit the total number of elements.

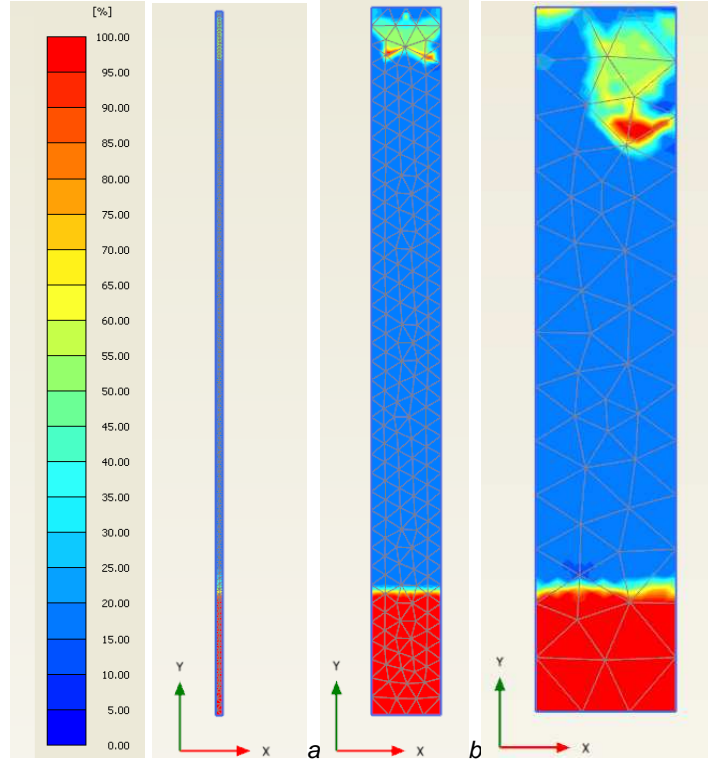


Figure 7.2.a,b and c Mesh refinement (a) EH = 0.20 m, (b) EH = 0.82m and (c) EH = 2.82 m

The element size has a huge influence on the uniform flow through the unsaturated zone. Also the depth of the water pulse at the end of January differs with element size. In Figure 7.2 b and c the element size is too large to give a uniform flow pattern. An element height 0.20 m gives a proper and uniform flow as illustrated in Figure 7.2 a. Thus, larger elements give irregular flow patterns and greater water pulse depths. In the following analyses, a small element height 0.20 m was used to obtain the most accurate results.

Bulk modulus of water

In the coupled and flow analysis in Plaxis, as presented in Section 5.3.1, the compressibility matrix is defined as follows:

$$\underline{\underline{S}} = \int_V \underline{\underline{N}}^T \left(\frac{nS}{K_w} - n \frac{dS}{dp_w} \right) \underline{\underline{N}} dV \quad [7.1]$$

The storage of the water is governed by the terms $\frac{nS}{K_w}$ and $\frac{dS}{dp_w}$. In case of a fully saturated situation $\frac{dS}{dp_w}$ is zero and S equals 1, then the compressibility is only governed by $\frac{n}{K_w}$. The bulk modulus of water is determined

from the relations listed in Table 7.2.

The bulk modulus of water is reduced by the presence of air-bubbles. In the saturated zone air bubbles are often present. In the unsaturated zone the amount of air increases with decreasing saturation, then for the representative bulk modulus can be written:

$$K_w^{unsat} = \frac{K_w K_{air}}{S K_{air} + (1-S) K_w} \quad [7.2]$$

The air pore pressure is assumed to be zero, therefore an artificial small value is used for the bulk modulus of air (K_{air}), namely 1 kPa (Galavi,2009). Thus, in fully saturated state ($S=1$) K_w^{unsat} is equal to K_w .

Drained	Undrained	Equivalent bulk modulus pore water
$G = \frac{E}{2(1+\nu)}$	$E_u = 2G(1+\nu_u)$	$dp_w = K_c \cdot \varepsilon_{vol}$
$K = \frac{E}{3(1-2\nu)}$	$K_u = \frac{E_u}{3(1-2\nu_u)}$	$K_c = \frac{K_w}{n} = K_u - K$
	$\nu_u = 0.495$	

Table 7.2. Relations between bulk and shear modules of drained and undrained soil to determine the equivalent bulk modulus of pore water.

In this analyses, where sandstone (for characteristics see Table 6.13) is considered, the bulk modulus water K_w is 225E6 kPa according to the above described method. This value is two orders of magnitude larger than the bulk modulus of pure water; which is: 2E6 kPa. It is physically impossible for the bulk modulus of water to be greater than that of pure water. The method for deriving K_w is used and tested for soils, whereas in this analysis sandstone is considered. Apparently, this method is not suited for calculating the K_w for rocks. Therefore, in the following the bulk modulus of pure water ($K_w = 2E6$ kPa) is used and thus the influence of air bubbles in the water is ignored.

7.1.2. Rainwater flow in the unsaturated zone

The analysis of the rainwater flow in the unsaturated zone with SWAP for the period July 2004 – June 2005 (see Section 6.1.4) showed that the rainwater does not reach the groundwater table. Also at the end of this period, the infiltrated water is practically all evaporated. In this section the infiltration of rain water is further evaluated with both Plaxis and SWAP.

The differences between the two programs are listed in Section 7.1. The rainfall for the period December 2004 – June 2005 is multiplied with a rainfall factor (RF) of 1, 2, 3, 4 and 5 in order to study the effect of increasing rainfall on the infiltration of rainwater into the unsaturated zone. Figures 7.3 to 7.12 illustrate the volumetric water content profiles for the different RF's at the end of each month.

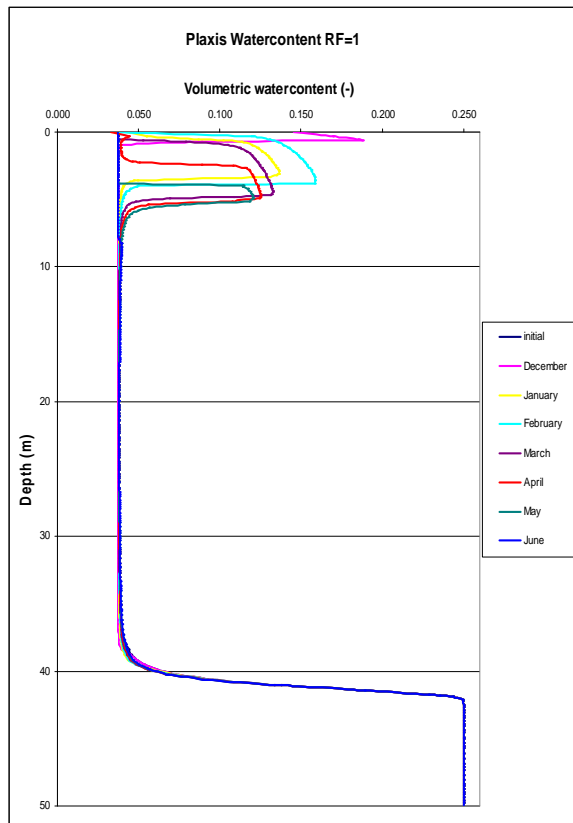


Figure 7.3 Plaxis water content curve for RF = 1

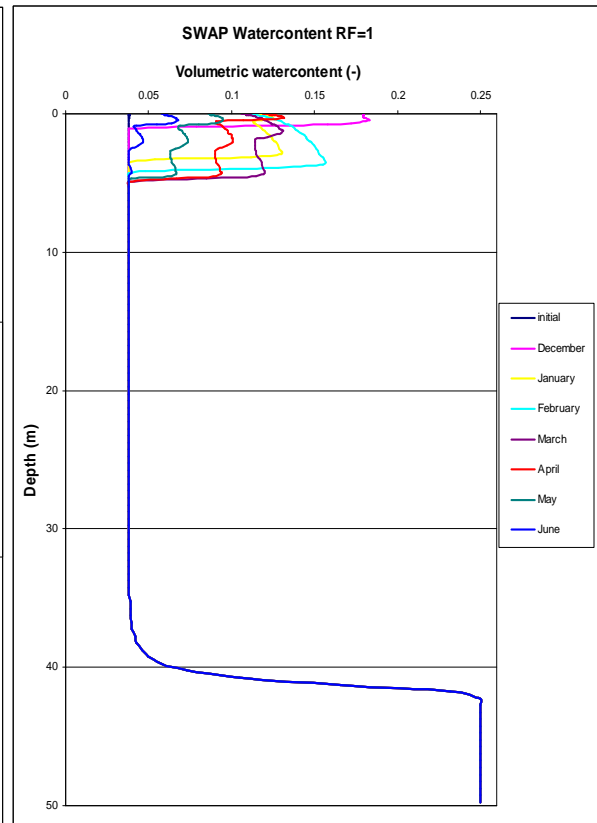


Figure 7.4 SWAP water content curve for RF = 1

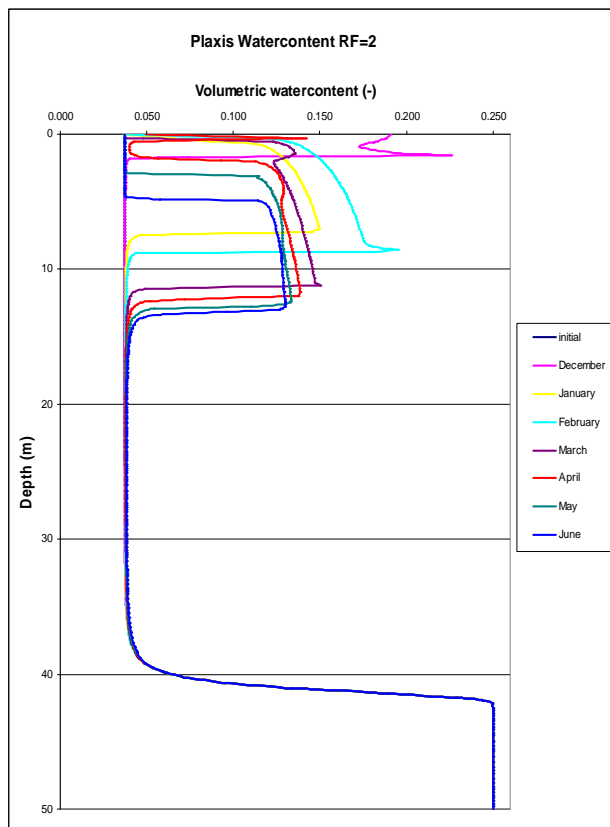


Figure 7.5 Plaxis water content curve for $RF = 2$

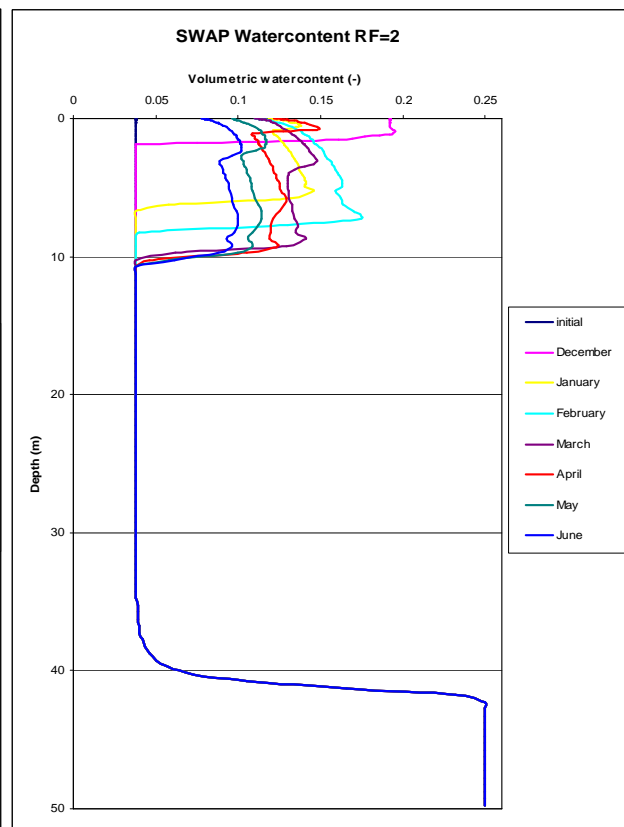


Figure 7.6 SWAP water content curve for $RF = 2$

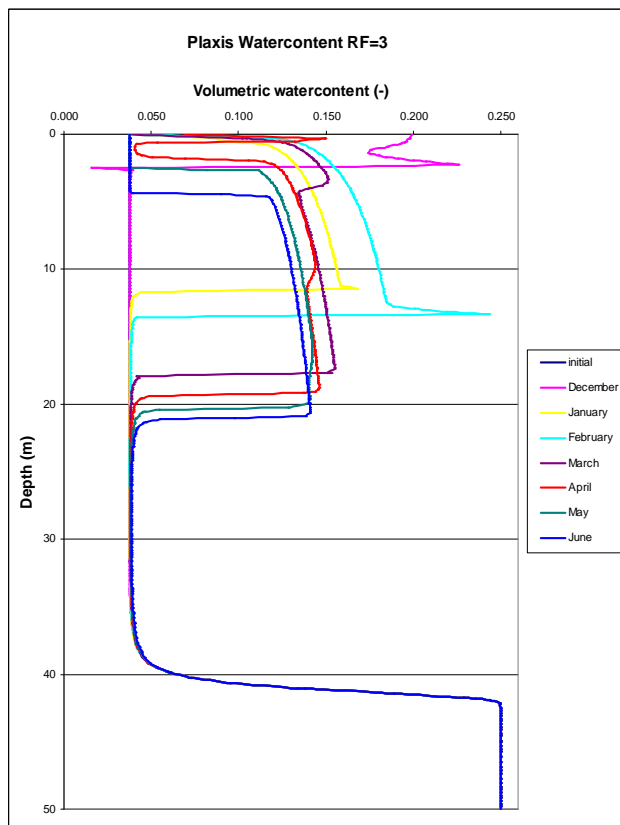


Figure 7.7 Plaxis water content curve for $RF = 3$

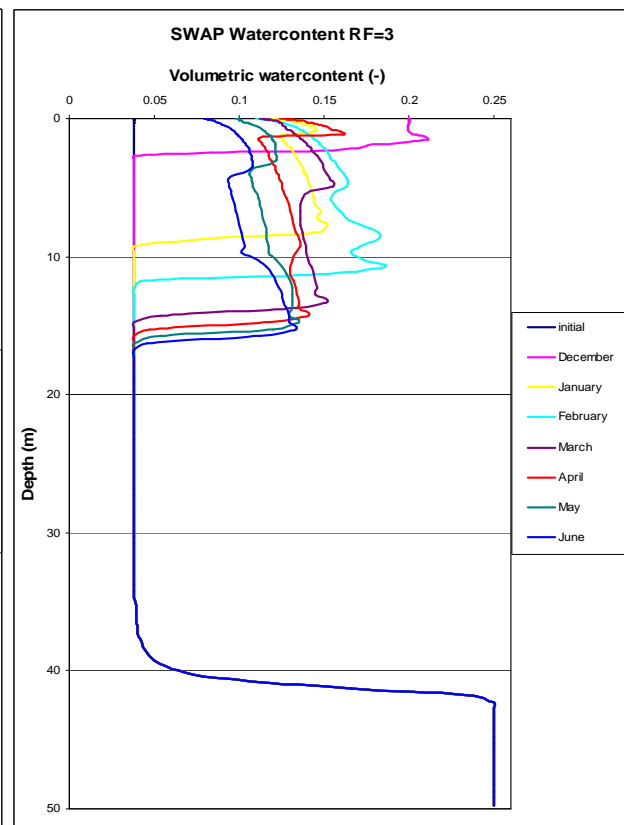


Figure 7.8 SWAP water content curve for $RF = 3$

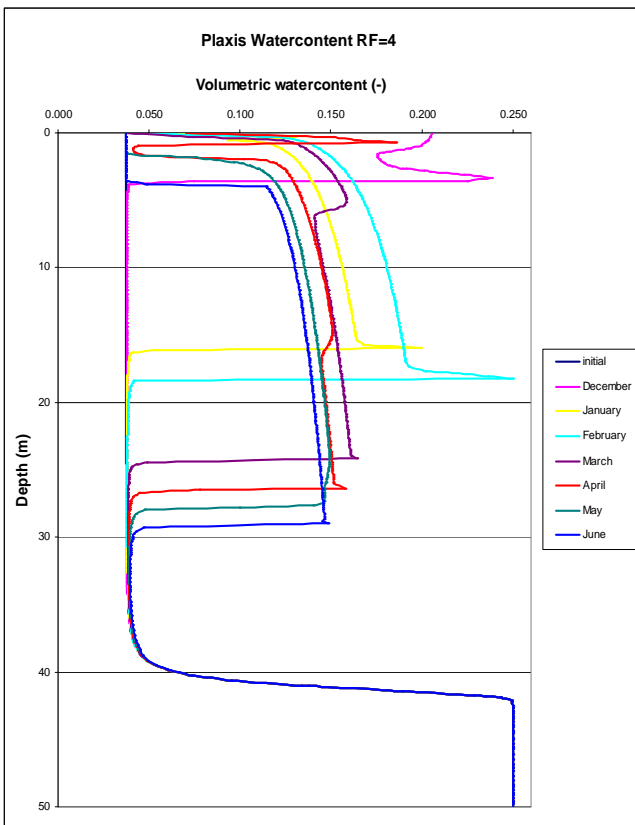


Figure 7.9 Plaxis water content curve for RF = 4

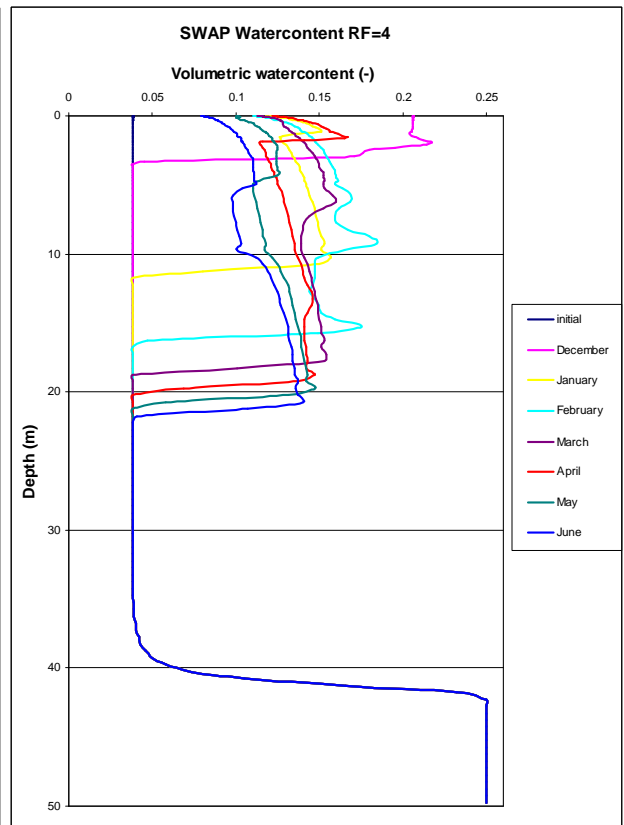


Figure 7.10 SWAP water content curve for RF =4

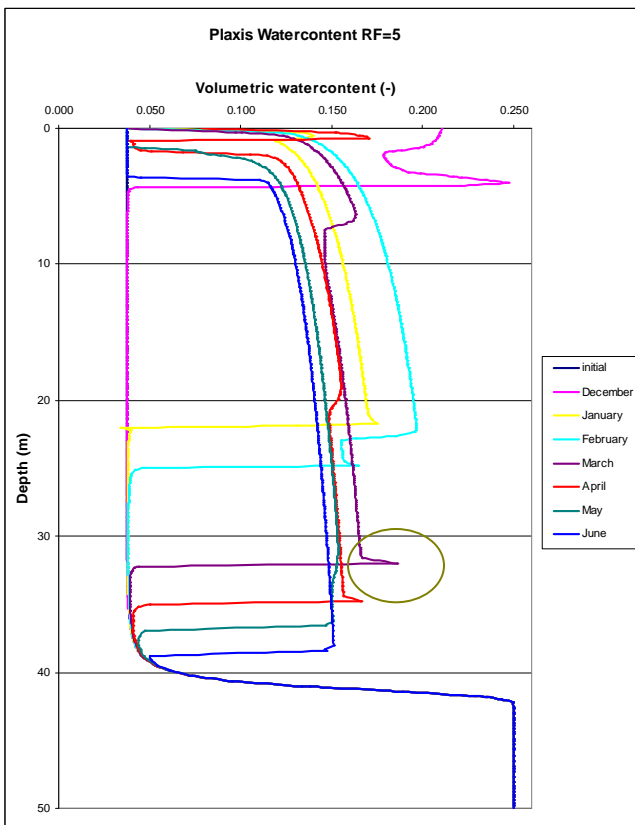


Figure 7.11 Plaxis water content curve for RF = 5

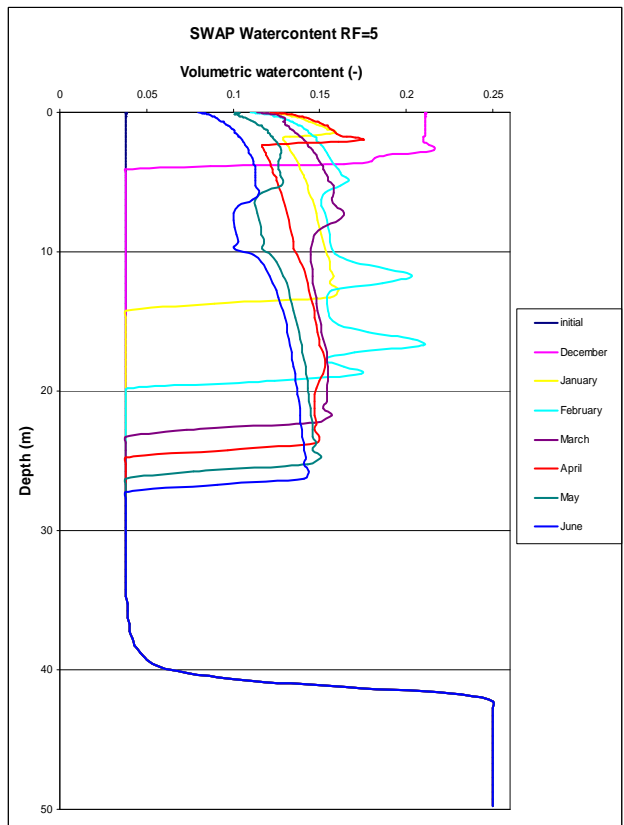


Figure 7.12 SWAP water content curve for RF =5

The propagation of the water pulse is the fastest in December to March when the rainfall is dominant; see Figures 7.3 and 7.4. Also the water pulse width is largest in these months, this holds in particularly for December. December records a few days of intense rainfall, especially at the end of the month, resulting in a wide water pulse with a short length. Then, in January, when rainfall continuous in the first two weeks, the water pulse continues to propagate. Next, in February the bulk of the rainfall occurs mainly in the second and third week, resulting in an even wider water pulse. The propagation of the water pulse slows down after March when the evapotranspiration increases and the rainfall is sporadic. In April there is one last day of large rainfall and a second water pulse can be observed at the top of the profile.

Comparing the general trend of water pulse propagation between those as calculated with Plaxis and SWAP, a difference of water pulse depth can be noticed. The difference between the water pulse depths can be explained with the limits of the residual relative hydraulic permeability (k_{res}) set by Plaxis and SWAP. In SWAP k_{res} is set to $0.9E-7$ m/d and in Plaxis k_{res} is set to $1.0E-4$ m/d. Applying a higher k_{res} results in a larger flow through the unsaturated zone.

The shape of the water content curve is more capricious in Plaxis then in SWAP. Note that the peaks in the water content curve of Plaxis, as indicated in Figure 7.11, are due to incorrect interpolation between nodes by the output program. The evapotraspiration was calculated in Plaxis as an out-flux at the top boundary and in SWAP the evapotraspiration was simulated by transpiration. Thus, in Plaxis the extraction of water happens by 'draining' the water pulse from the top. Whereas, in SWAP the extraction occurs uniformly across the length of the maximum root depth (10 m). However, if the roots do not reach the water pulse, then the water will be sucked by the roots and draining the water from above. When applying evapotranspiration and small rooted vegetation in such a fashion that 50% of the surface is covered with vegetation, the actual evapotranspiration is about 55% with respect to reference evapotraspiration.

Since the reference evapotranspiration is not completely reached in SWAP (see Section 7.1), a small difference can be observed with the water content of the unsaturated zone as calculated with Plaxis. This difference is illustrated best in Figures 7.3 and 7.4 where $RF=1$. In June the water pulse is practically drained according to Plaxis, whereas according to SWAP this small pulse remains.

The depth of the (bottom) water pulse at the end of June increases relatively linearly with RF , as shown in Figure 7.13. The difference between Plaxis and SWAP also increases with RF due to the amount of water infiltrating the profile. Further study showed that in Plaxis the water pulse reaches the groundwater level in April with a RF of 6, whereas in SWAP this occurs in May with a RF of 8.

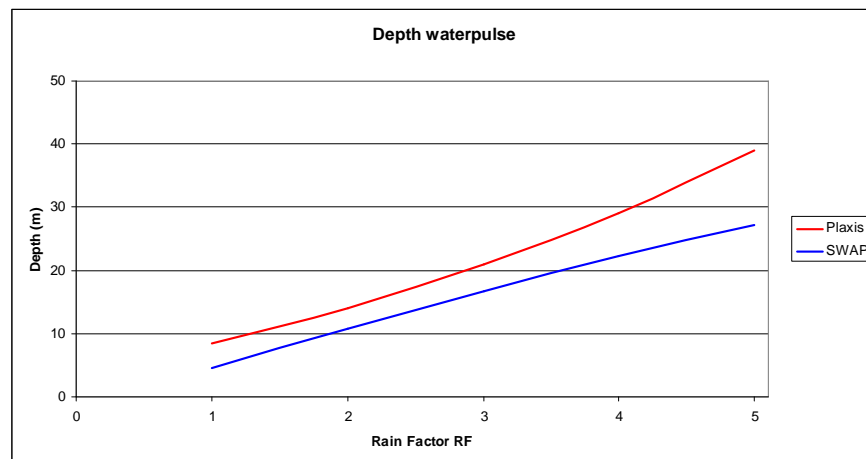


Figure 7.13 Depth of water pulse with increasing RF

Since SWAP is developed for agricultural applications, the environmental influences, such as vegetation and near surface evaporation, are described with more detail provided that the environmental and soil parameters are known. In SWAP the vegetation characteristic had to be altered to extreme values in order to facilitate the required evapotranspiration.

To discriminate between the results obtained by SWAP and Plaxis, validation with experimental data is necessary. However, such data is lacking for the BRM. The distribution of the water content is essential for the pressure in the unsaturated zone. Monitoring of the pressure with tension meters is therefore advised.

As mentioned in Section 6.4. other sources of inflow, such as irrigation and septic tanks, can locally contribute to the water pulse and thus the water pulse propagation. Furthermore reduction of the evapotranspiration decreases the draining of the water pulse causing it to be larger and to propagate further.

7.1.3. Pressure

The pressure curve for rainfall factor equal to 1 (RF=1) at the end of each month is displayed in Figures 7.14 and 7.15 for Plaxis and SWAP, respectively. As mentioned earlier the reference evapotranspiration is calculated in SWAP as transpiration and in Plaxis as an out-flux. Consequently, the pressure curves differ remarkably between Plaxis and SWAP. In SWAP the suction, which is considered as a negative pore water pressure, is largest just below the water pulse (see Figure 7.15), due to the roots of the vegetation sucking the water from below the pulse. Also in SWAP large suction occur in June, this can be attributed to numerical convergence error due to large gradients resulting from very low water contents. In Plaxis the suction increases at the top of the profile (see Figure 7.15), due the prescribed out-flow to drain the water.

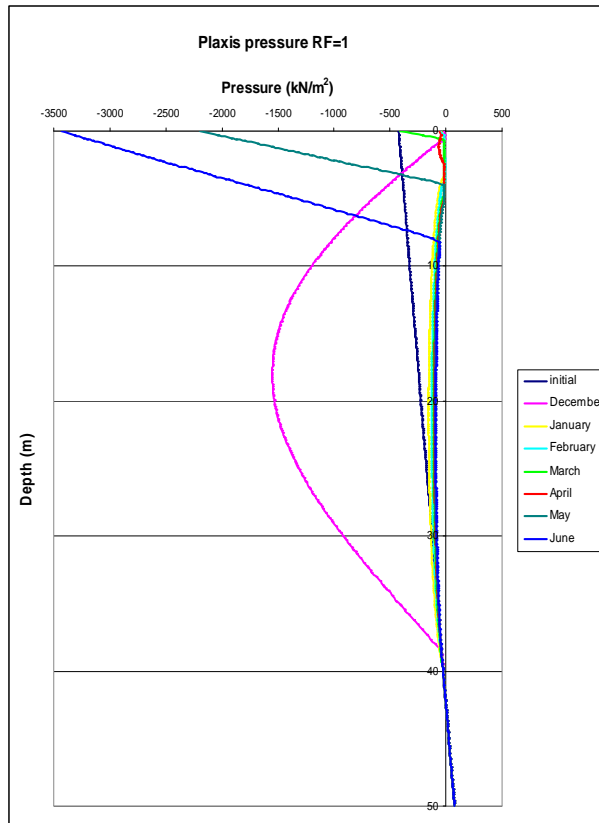


Figure 7.14 Plaxis pressure curve for RF = 1

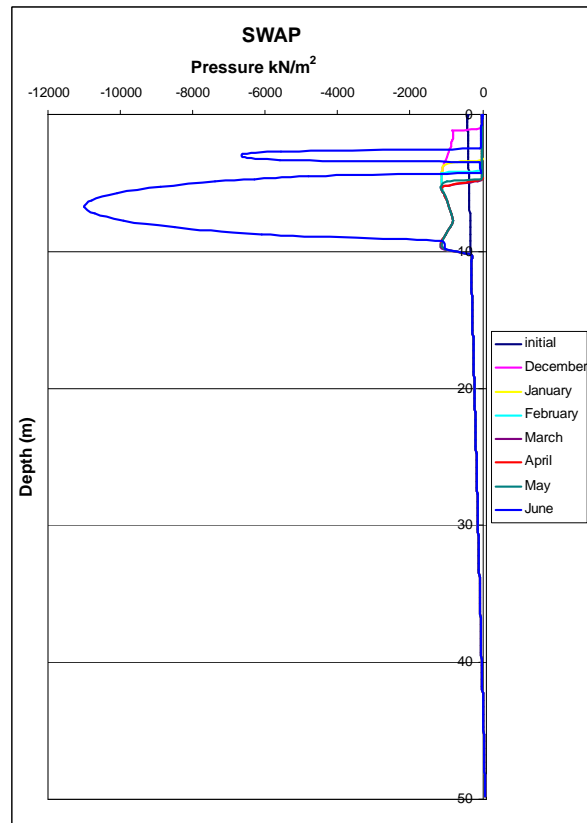


Figure 7.15 SWAP pressure curve for RF = 1

The pressure curves obtained by SWAP and Plaxis may be similar, if the out-flux at the top is the same. Then in SWAP the roots of the vegetation should drain above the water pulse and the reference evapotranspiration should be reached. However, this can not be realized (see Section 7.1). Almost the same out-flux could only be obtained by setting the root depth to its maximum value, i.e. 10 m.

Although SWAP is very useful to predict the rainfall soil interactions and allows accounting for various vegetations, in the following only the results obtained with Plaxis are used. This choice is motivated by the fact that Plaxis allows coupled analysis of deformations and groundwater flow.

The pressure curves generated by Plaxis for RF=1 in Figure 7.14 are largest at the end of the months May and June. In these two months the evapotranspiration is predominately active. In April also mainly evapotranspiration occurred, but due to a day of heavy rainfall at the end of April the suction at the top of the profile is small. The influence of the evapotranspiration is limited to the top height of the water pulse, which leads to more saturation and consequently the suction decreases. In December heavy rainfall only happened at the end of the month. Thus, in the beginning of this month the

evapotranspiration is active across the whole profile and not limited to the height of the water pulse. At the end of December, when water starts to infiltrate, the suction decreases.

A clear correlation between suction at the top and depth to the water pulse is found for the Plaxis results. In Figure 7.16 the suction at the top and depth to the water pulse for the end of the month June are displayed as a function of the rainfall factor RF. The largest difference between top boundary suction occurs between RF=1 and RF=2, which is due to the almost complete draining of the water pulse for RF=1. If more water enters the profile complete draining of the water pulse becomes harder, because the out-flux remains equal. With increasing RF more water infiltrates into the profile. However, the depth to the water pulse and the corresponding suction at the top only decreases slightly with increasing RF. From the analyses of the water content curves it follows that the width of the water pulse remains fairly equal, but the length of the pulse increases; see Section 7.1.2.

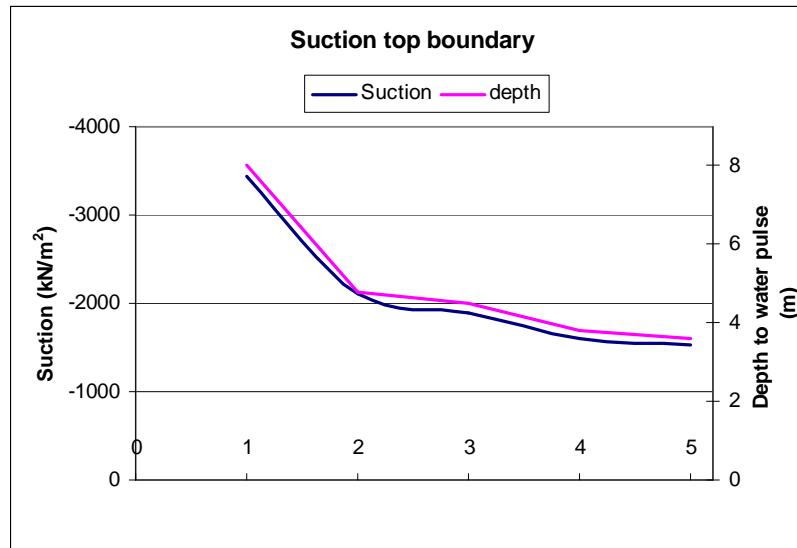


Figure 7.16 Pressure at the top of the profile with increasing RF

The pressure curve appears to be linear with depth till the water pulse in the months of May and June; see Figure 7.14. This is a result of the high suction at the top and limited depth to the water pulse. In Figure 7.17 the pressure curve is displayed of 4-December-2005 just before a small amount of water was infiltrated, showing a much more curved line. The evapotranspiration is active across the whole profile. However, as mention before, the evaporatranspiration is limited by near surface evaporation and maximum root suction. It is also likely that there is already a water pulse present in the unsaturated zone due the rainfall in the previous period. Other sources of infiltration such as local irrigation (although this role is probably small) and onsite waste disposal units may have contributed to the water pulse in the unsaturated zone. The pressure distribution in December (as displayed in Figure 7.17) is unrealistic and should therefore be ignored.

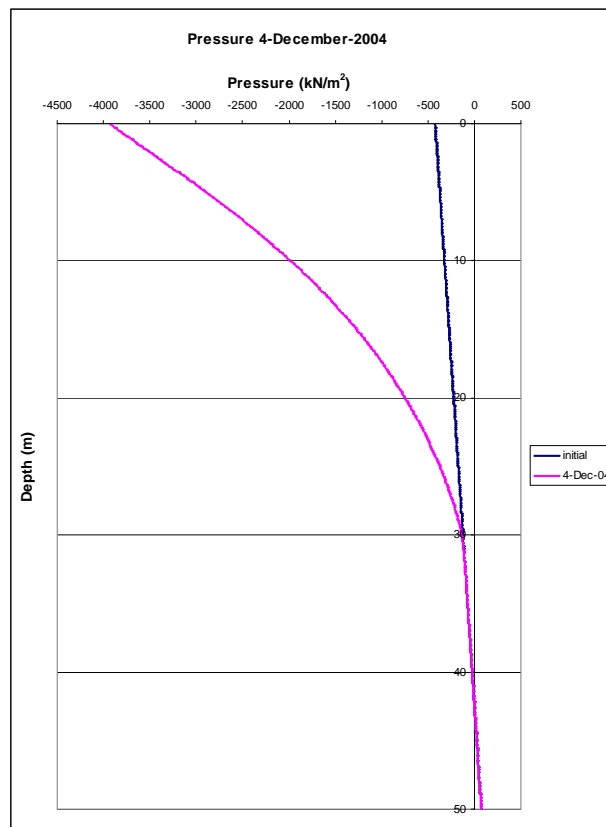


Figure 7.17 Pressure at 4 December 2004

The water content and pressure are related in the retention curve. If below the water pulse the residual water content would be present, the pressure curve should follow the initial curve. In Figure 7.14 this is not the case because the water has very slightly infiltrated further into the profile. The infiltration below the water pulse is very small but has relatively large influence due to the steepness of the retention curve. The area of the retention curve that governs this influence is indicated in with a red circle in Figure 7.18.

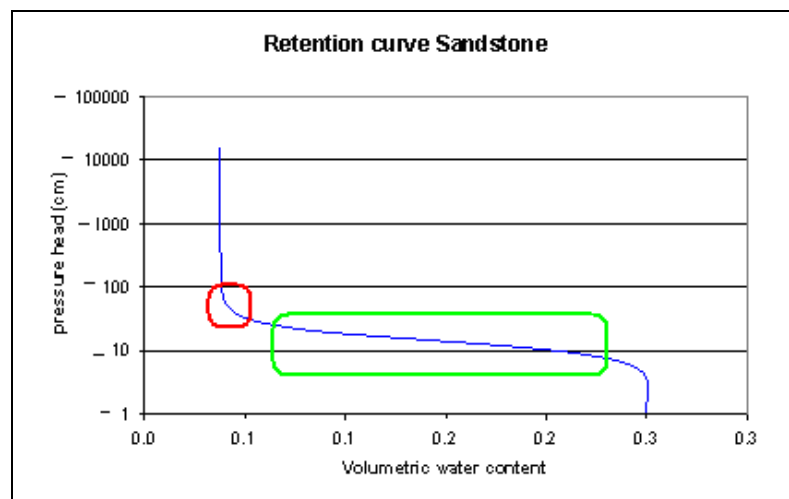


Figure 7.18 Retention curve (parameters table 7.1)

Figure 7.19 represents the pressure curves for different RF at the end of February. From these curves it is clear that over the length of the water pulse the suction is minimal. The amount of water content in the water pulse (i.e. the width of the pulse) varies little with increasing RF and also has little influence on the corresponding suction, see Figures 7.19 and 7.20. The variation in water content has a small effect on the suction (see Figures 7.3 and 7.14), due to the shallowness of the retention curve. This corresponds with the green rectangle in the retention curve; see Figure 7.18.

Infiltration of water into the profile reduces the suction as displayed in Figure 7.19 for the end of February. This decrease in suction weakens the soil. Consequently, the stability of a slide increases with evapotranspiration and decreases with water infiltration.

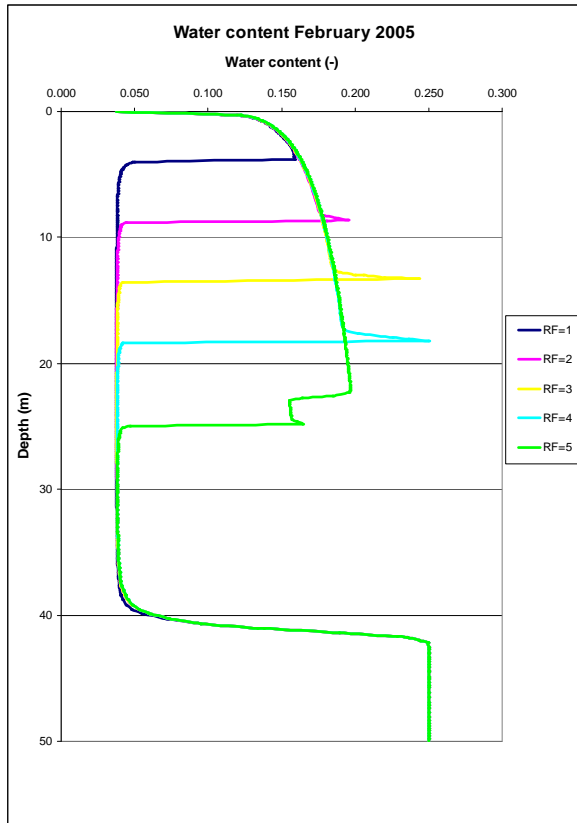


Figure 7.19 Water content at the end of February

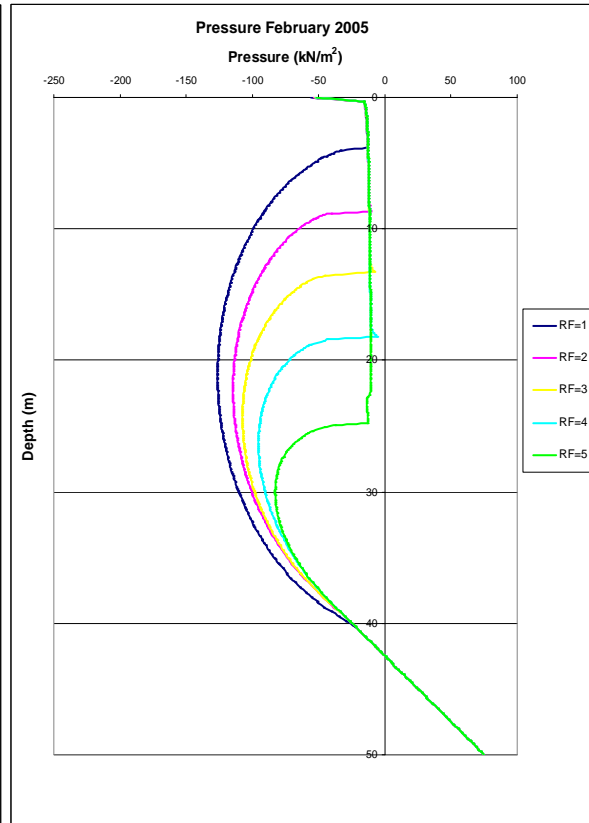


Figure 7.20 Pressure at the end of February

7.2. Retention curve parameters

The retention curve (pressure versus water content) is described with the ‘van Genuchten’ parameter, see Section 4.1. The parameters used in this study (see Table 7.1) are derived from literature and may differ from reality. In order to study the effect of these empirical parameters on the flow through the unsaturated zone, the parameters g_n , g_i , g_a and S_r are varied for the period of December 2004 – June 2005, for $RF = 1$. For this evaluation the water content and the pressure curves pertaining to the end of May was chosen.

Parameter g_n

The empirical parameter g_n has influence on both the retention curve and the relative permeability. Lowering g_n results in a steeper retention curve, as shown in Figure 7.21, and lower relative permeability values (k_{rel}) as illustrated in Figure 7.22. The values for g_n used are 2, 3 and 4 for which the corresponding water content and pressure curves at the end of May are illustrated in Figures 7.23 and 7.24, respectively.

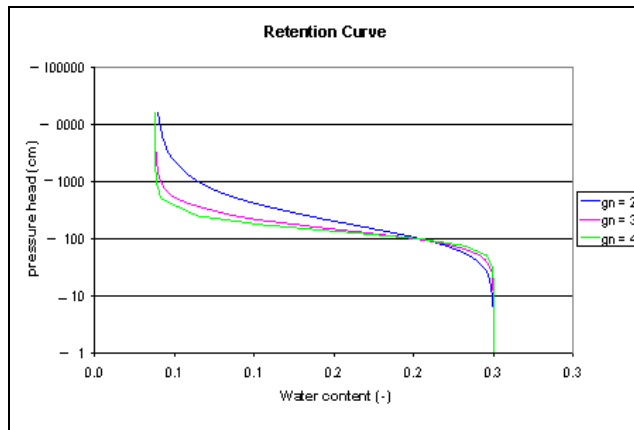


Figure 7.21 Retention curve $g_n = 2, 3$ and 4 .

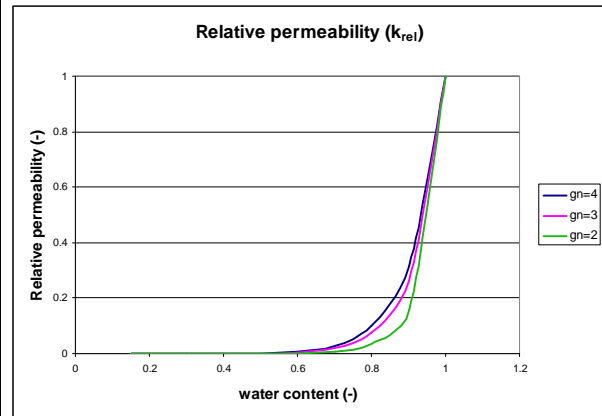


Figure 7.22 Relative permeability $g_n = 2, 3$ and 4 .

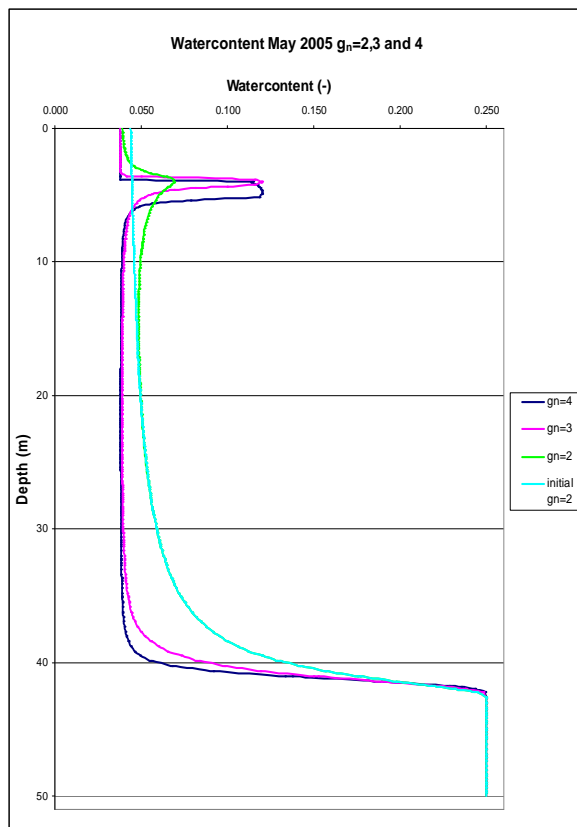


Figure 7.23 Water content curve $g_n=2, 3$ and 4

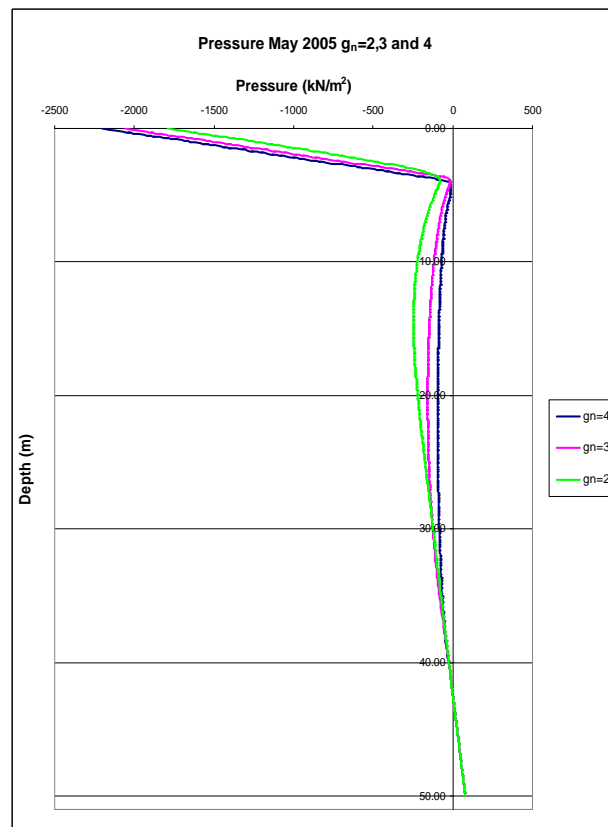


Figure 7.24 Pressure curve $g_n=2, 3$ and 4

Due to the steepness of the retention curve, the residual water content is not reached for $g_n=2$ at the initial stage, as shown in Figure 7.23. However, at the end of May, after a period of evaporation, the residual water content is reached. The water pulse depth as well as the suction at the top increases with raising g_n ; see Figures 7.23 and 7.24 respectively. Also the amount of water infiltrating the profile increases with raising the value of g_n , as can be seen in Figure 7.23. These effects are related to the higher values for the relative permeability k_{rel} .

Parameter g_i

The empirical parameter g_i has only influence on the relative permeability k_{rel} , but not on the retention curve; see Section 4.1, Equation 4.2. Lowering of the value for g_i results in higher k_{rel} values; see Figure 7.25. The corresponding curves for the water content and pressure are presented in Figures 7.26 and 7.27, respectively. If the permeability is high, the water drains faster by evaporation and the suction at the top of the profile also increases.

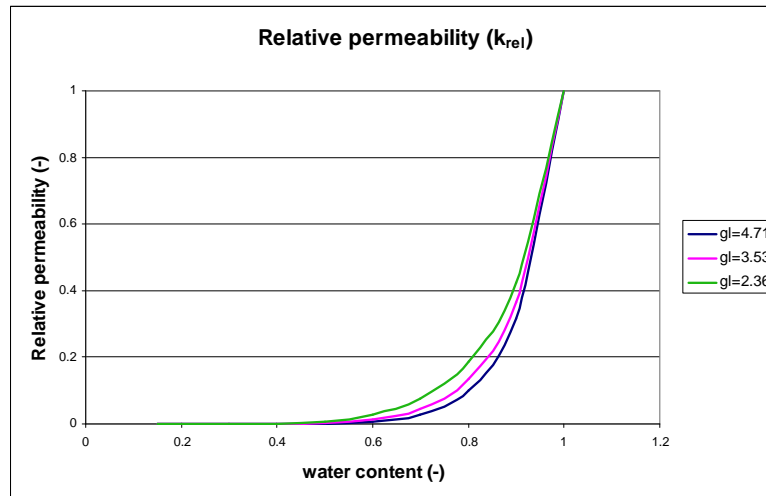


Figure 7.25 Relative permeability $g_i = 2.36, 3.53$ and 4.71 .

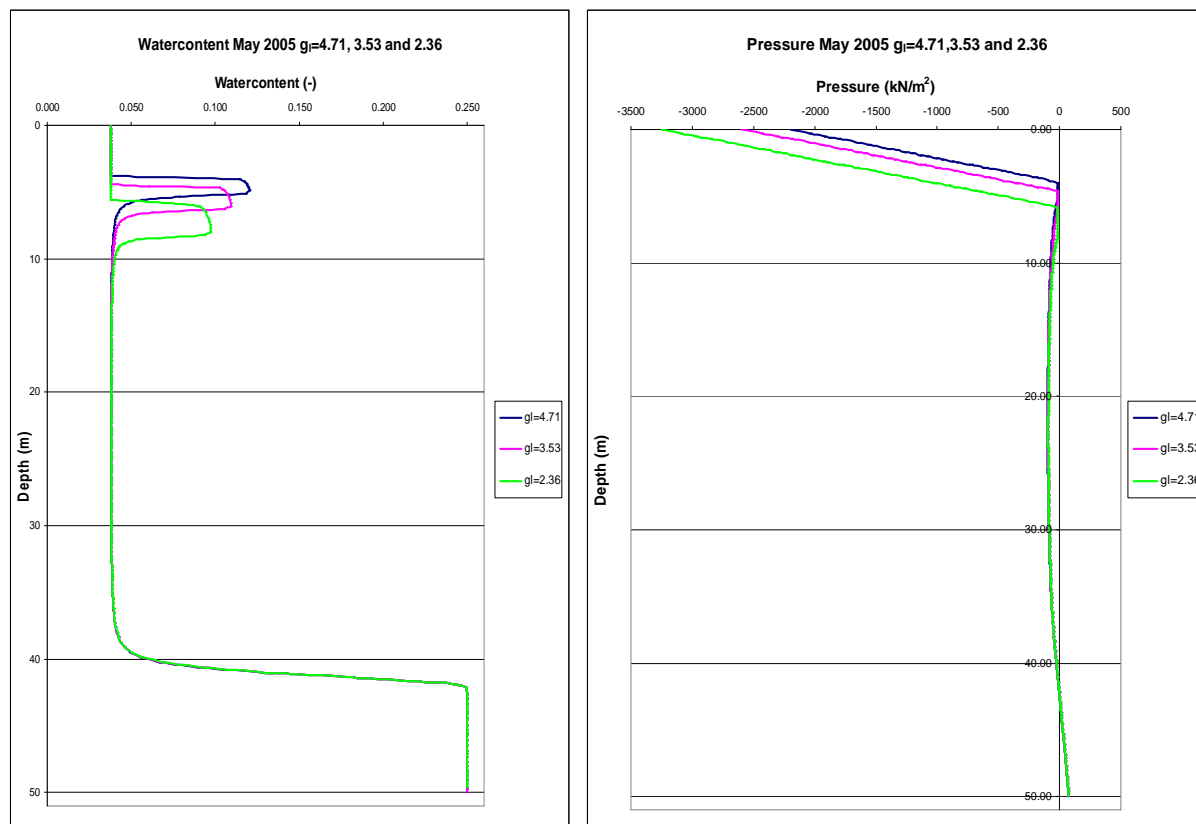


Figure 7.26 Water content curve $g_i = 2.37, 3.53$ and 4.71 . Figure 7.26 Pressure curve $g_i = 2.37, 3.53$ and 4.71 .

As expected, the water pulse depth increases with decreasing values for g_i . For $g_i=4.71$ the depth of the pulse is 8 m. This depth increases to 9 m for $g_i=3.53$ and 10.5 m for $g_i=2.36$.

Parameter g_a

The empirical parameter g_a only influences the retention curve, but has no effect on the relative permeability. Increasing the g_a from 0.79 to 1.6 and 2.4 (m^{-1}) lowers the position of the retention curve as shown in Figure 7.28. In Figures 7.29 and 7.30 the corresponding curves for the water content and pressure are displayed, respectively. As can be seen in these figures, changing the value for g_a hardly influence the shape water content and pressure profiles.

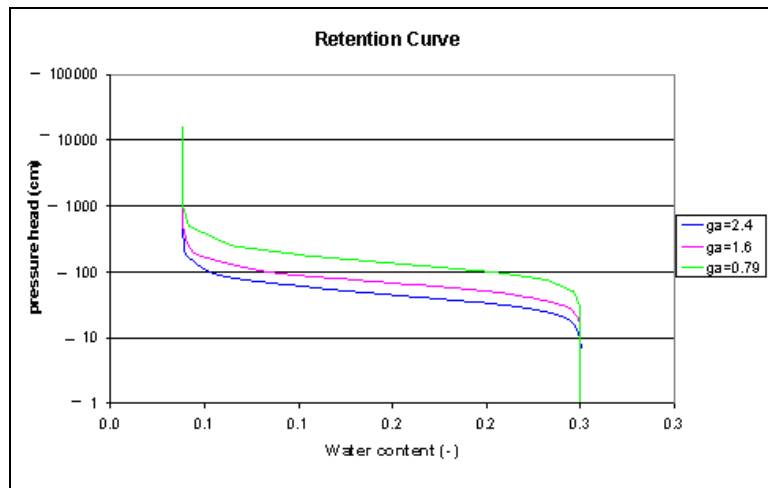


Figure 7.28 Retention curve $g_a = 0.79, 1.6$ and 2.4 (m^{-1}).

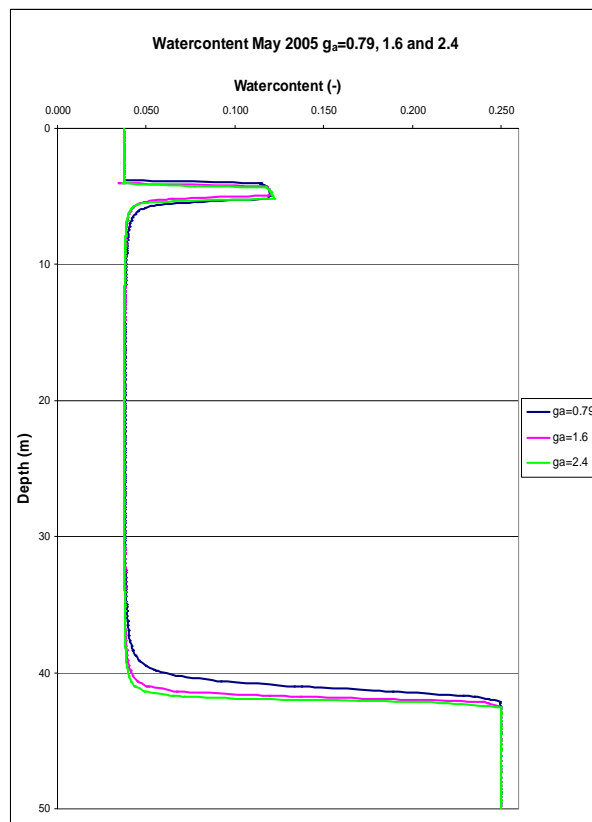


Figure 7.29 Water content curve $g_a = 0.79, 1.6$ and 2.4 (m^{-1}).

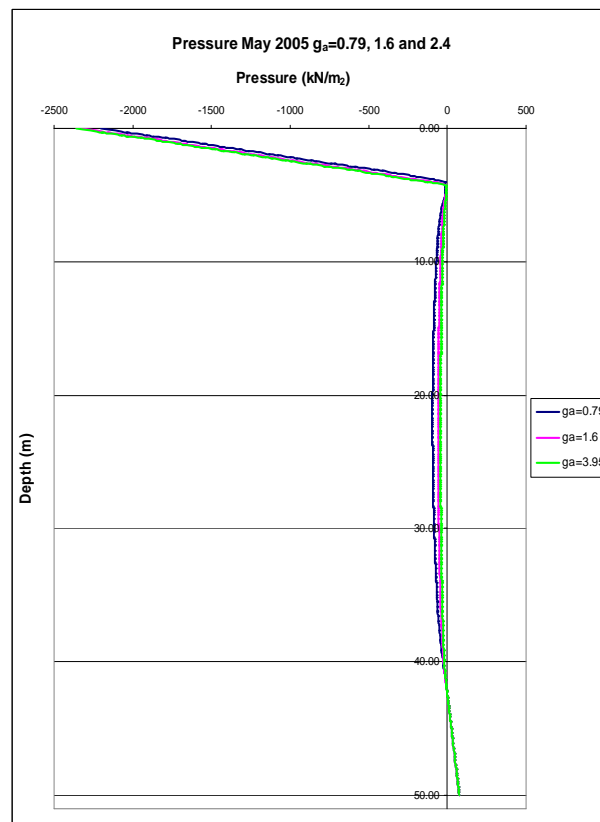


Figure 7.30 Pressure curve $g_a = 0.79, 1.6$ and 2.4 (m^{-1}).

Residual Saturation

The residual saturation S_r (i.e. the residual water content) determines the position of the outer limit of the retention curve. Increasing S_r decreases this limit, as shown in Figure 7.31. The effect of S_r on the relative permeability k_{rel} is very small, but it decreases slightly with increasing values for S_r , as can be seen in Figure 7.32. In Figures 7.33 and 7.34 the curves are displayed for the water content and pressure, respectively.

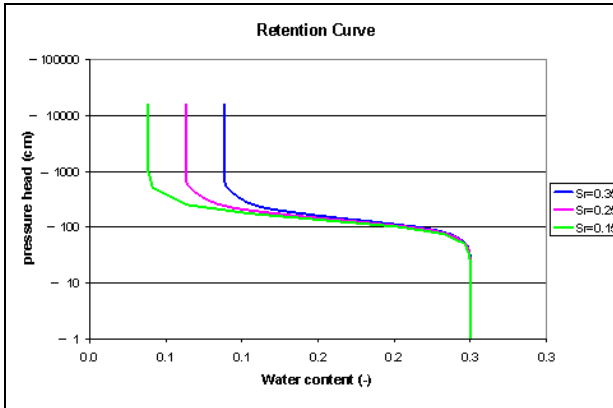


Figure 7.31 Retention curve $S_r = 0.15, 0.25$ and 0.35 .

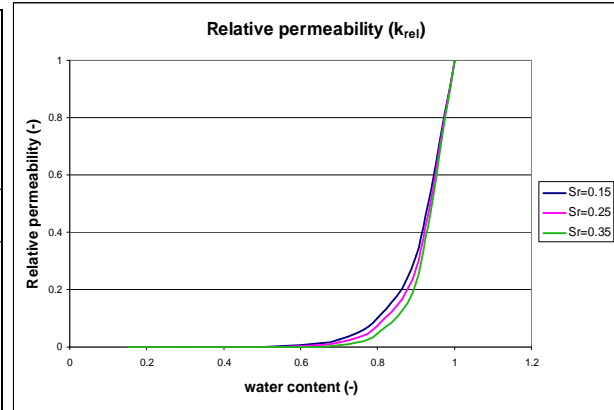


Figure 7.32 Relative permeability $S_r = 0.15, 0.25$ and 0.35 .

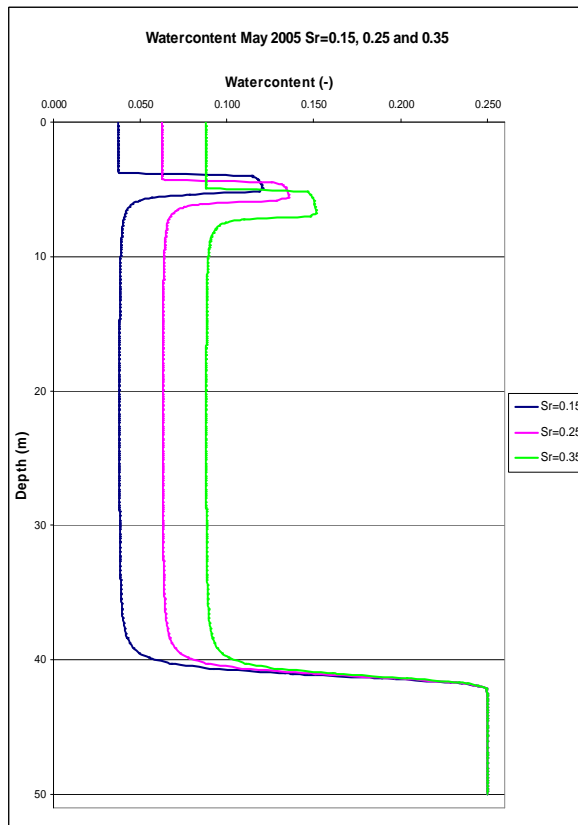


Figure 7.33 Water content curve $S_r = 0.15, 0.25$ and 0.35 .

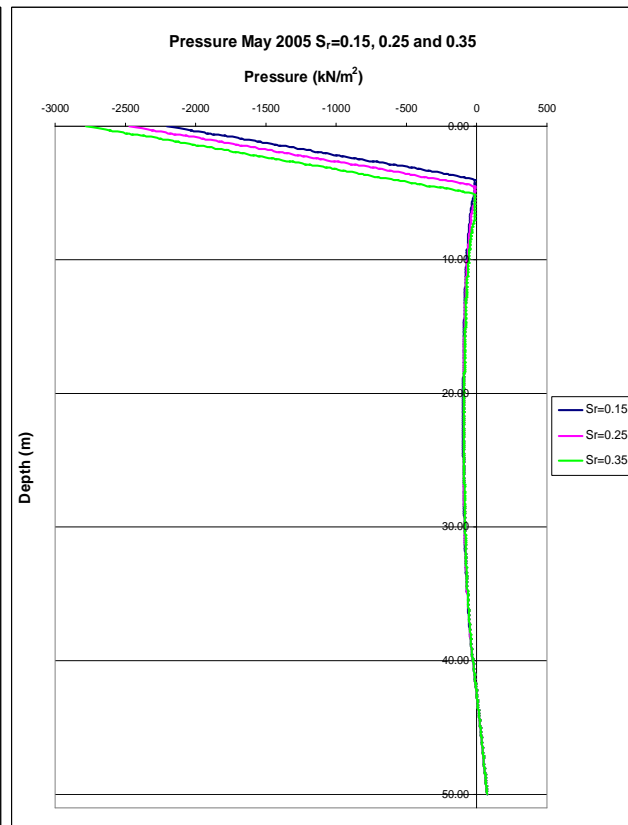


Figure 7.34 Pressure curve $S_r = 0.15, 0.25$ and 0.35 .

The water pulse depth increases with increasing residual saturation, due to the increase in maximum water content. Along with the increasing water pulse depth, the pulse top and corresponding suction also increase.

The van Genuchten parameter g_n has influence on the retention curve and relative permeability. Decreasing g_n results in slower flow in the unsaturated zone and thus decreasing the depth of the water pulse. When g_n is equal to 2 the residual water content is not reached at the top of the profile. This means that water is available at the top for evaporation.

Decreasing the van Genuchten parameter g_l results in higher values for k_{rel} and thus also faster propagation of the water pulse. Increasing the 'van Genuchten' parameter g_a (by a factor 2 and 3) has little influence on the water content distribution. Finally, increasing the residual saturation S_r results in higher maximum water content. Higher water content increases the relative permeability and thus the water pulse propagation.

7.3. BRM coupled analysis

In Section 7.1.1. the refinement of the mesh was determined to an element size of 0.20 m. However, due to size of the BRM, the minimally achievable average element height (EH) is 9 m, corresponding with 5E3 elements. Applying a mesh with EH 0.20 m increases the number of elements to about 1E7 and the number of nodes to about 1.5E8. It is not feasible with the currently available computing power to run the scenarios. A solution may be to enable Plaxis to run on a supercomputer or make parallel processing possible.

In order to analyse the effect of increasing inflow from other regions, the pressure head at the 'hill'-side of the BRM was increased with 5 and 10 m, see Figure 7.35. A steady state flow calculation was performed with the coupled analyses after which the safety factor is determined. The analyses were performed for active suction and no suction in the unsaturated zone. In Figure 7.36 the safety factor as a function of the increasing head is shown.

Note that there are some inaccuracies in the flow field as indicated in Figure 7.36 with a pink circle. Reduction of the element size is likely to eliminate these inaccuracies.

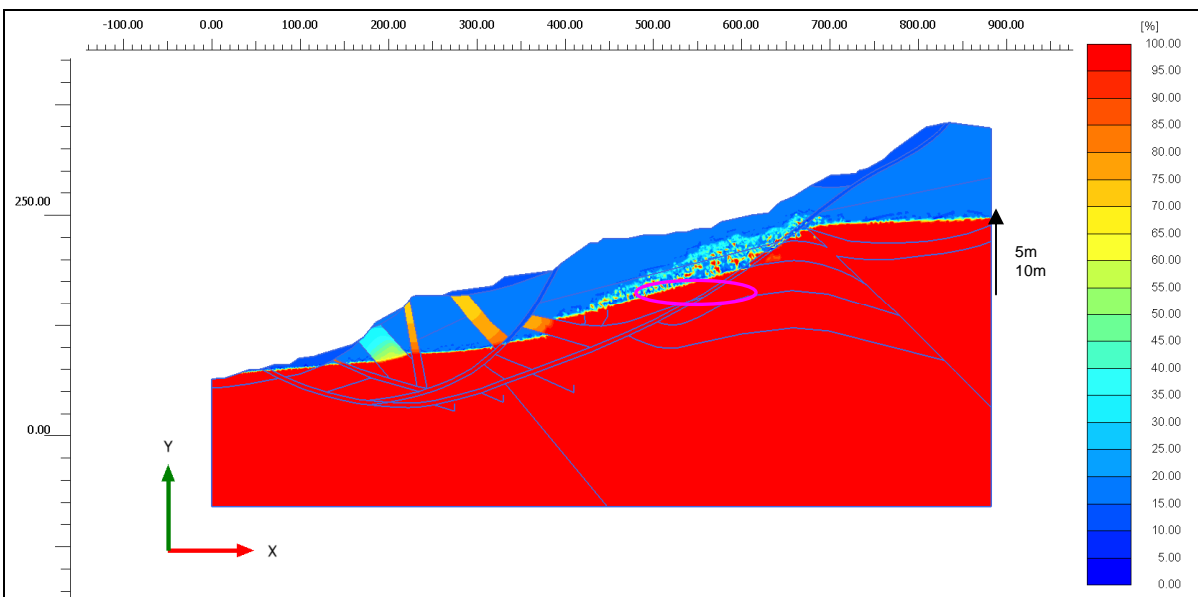


Figure 7.35 Saturation profile BRM for $h=0$

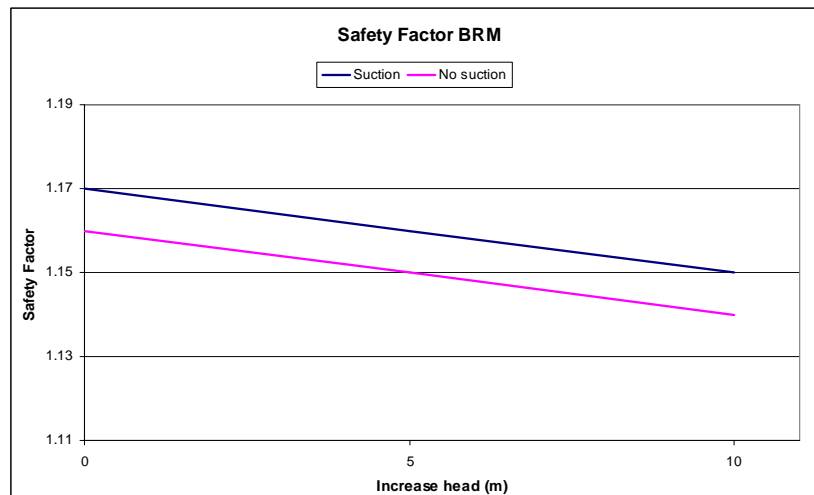


Figure 7.36 Safety factor BRM with increasing head.

As shown in Figure 7.35, the safety factor slightly decreases more when increasing the head from 5 to 10 m than from 0 to 5 m. The difference in safety factor between suction and no suction is roughly 0.01.

From the analyses of the unsaturated zone flow the suction in this zone decreases when water infiltrates. It can be assumed that the actual safety factor lies between the safety factor of suction and no suction.

The evaluation of the inclinometer data from the BRM, presented in Chapter 3 and 6, it was concluded that the displacement was minimal. From Figure 7.36 it may be derived that the stability decreases only slightly under increasing pressure head. This corresponds with the minimal displacement and thus the BRM can be considered as a stable slide for the conditions specified here.

In Figure 7.37 the saturation distribution of an increase of head with 10 m is shown. It can be observed that the main influence of this increase lies in the middle and upper part of the slide. The lower part experiences little to no influence.

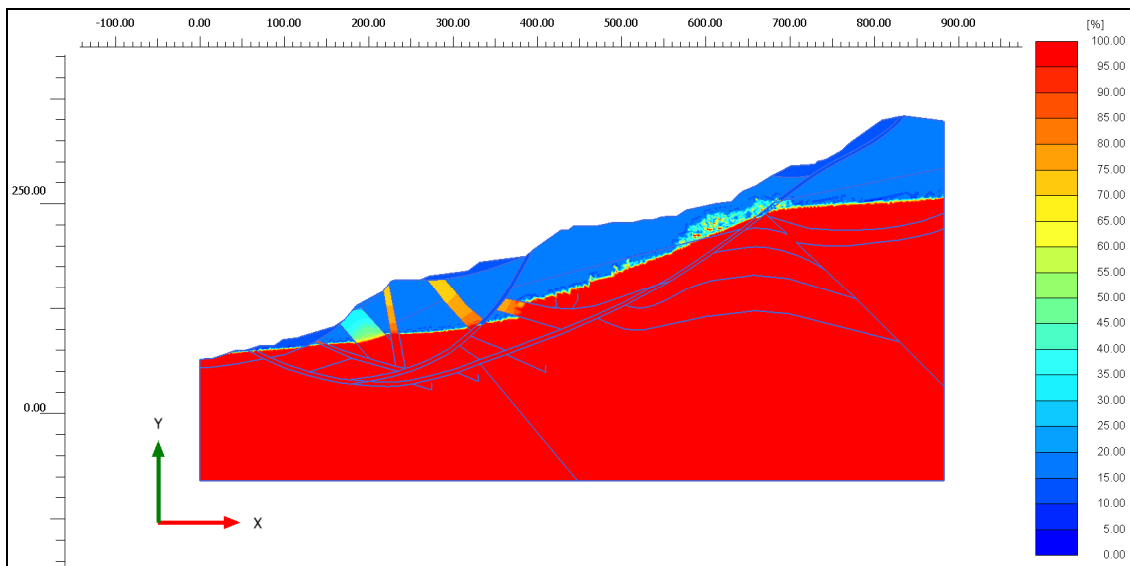


Figure 7.37 Saturation profile BRM for $h=10\text{m}$

7.4. Remedial measures

Infiltration of water has two consequences (i) increasing groundwater table and (ii) reduction of strength in the unsaturated zone. The second is only important for large distances between groundwater level and surface. In order to keep slopes stable it is important to reduce the infiltration of water. There are two methods that can be used to accomplish the lowering of water infiltration (i) constructing drainage and dewatering systems and (ii) increasing the evapotranspiration.

Drainage systems

The installation of wells that continuously pump is very costly. The BRM is a massive slide with an enormous amount of water. From the water balance presented in Section 6.4, it is clear that the current well is limited and only plays a minor role. The effect of the current hydraugers on the water balance is even smaller and a lot more would have to be installed in order for it to have a greater effect.

Another option is to use drainage systems such as filter systems. Filter systems are graded soil layers with coarse material on top placed as a cover on the surface of the slide. Besides graded filters a coarse layer on top of geotextile can be used. A system to drain rainwater that is already used, but can be extended, comprises of concrete slabs with a groove that are installed next to the roads.

Evapotranspiration

Evapotranspiration is the sum of evaporation and transpiration. Because the evaporation is influenced by factors outside human control, namely the weather, it is not possible to change this.

However, transpiration is the extraction of water by vegetation. More average vegetation, such as plants and grass, may limit the infiltration of rainwater to the depths of their roots. But this vegetation needs to be irrigated in dry periods. There are some trees that can drain water up to a depth of 20-30 m. In regions with large distance between groundwater level and surface these trees can drain water from the groundwater and also drain the infiltrated water over the whole thickness of the unsaturated zone. In dry periods they can also increase the suction and strengthen the soil.

8. Conclusions and recommendations

The stability of landslides is susceptible to rainfall and changes to the groundwater level. The corresponding pressure changes cause slopes to become unstable. In the case of slow moving landslides that are stable during dry periods and displace during wet periods the relation between rainfall and displacement is vital. Rainfall has two consequences for the subsurface: (i) reduction of the suction in the unsaturated zone and (ii) increasing groundwater level.

A study was performed for the case Big Rock Mesa (BRM), a massive slow moving landslide in California (USA). To evaluate the hydraulic flow a water balance was made for a critical and stable period. The characteristics of the different layers were analysed. The stability of the slide under influence of groundwater level rise was calculated. Finally, the flow through the thick unsaturated zone below the slope surface and the corresponding pressure distribution was evaluated.

In this Chapter the main conclusions for the evaluation of the BRM on the influence of infiltrating rainwater are presented. Next, recommendations are provided for further study in the field of slow moving landslides and for the BRM.

8.1. Conclusions

On the basis of data collected of the BRM a detailed description of its geometry and structure was obtained and the various soil layers were identified. The properties of each layer in terms of strength and permeability were determined using computational methods. The strength parameters were obtained with Roclab, a program that employs the Hoek and Brown criterion to derive the Mohr-Coulomb properties. The groundwater level was determined based on observational data with a statistical program called Surfer. The permeability's of the layers were derived from best fits to the groundwater level profile. It was shown that this groundwater level profile strongly depends on the permeability of the soil layers. The parameters for the retention curve (water pressure versus water content) according to 'van Genuchten' were estimated using literature data.

The water balance for the BRM was constructed for the period July 2004 – June 2005, which comprises the rainfall, evapotranspiration, storage change, run-off, dewatering and x-flow. The x-flow covers all the unknown inflow minus out flow. Rapid changes in the x-flow and the storage changes (groundwater level rise) suggest that the majority of the rainwater was stored in the unsaturated zone. This was confirmed by unsaturated flow analyses in a one-dimensional flow program called SWAP. In this analysis the rainwater remained in the unsaturated zone for the whole duration of the analyses. The water pulse in the unsaturated zone is slowly drained by the evapotranspiration. The x-flow is most likely water that flows to the BRM from adjacent areas.

The safety factor related to the Down slope slide and the Main slide, influenced by upper and lower groundwater levels and thickness of the shear zone, shows that the Main slide is the most critical. The safety factor decreases only little with rising groundwater level. To a lesser extent the safety factor depends slightly on the thickness of the shear zone.

Unsaturated zone flow

After rainfall a water pulse propagates downwards through the unsaturated zone. The average depth of the unsaturated zone in the BRM is 42.5 m. The water content at the top is equal to the residual water content in dry conditions, due to a steep retention curve. The water pulse propagates to a depth of 8 m for the simulated period December 2004 – June 2005. This propagation depth increases linearly with increasing rainfall. However, the water pulse doesn't reach the groundwater level.

Infiltration of water into the profile reduces the suction. This suction is smallest over the length of the infiltrating water pulse. The reduction of suction weakens the soil. Consequently, the stability of a slide increases with evapotranspiration and decreases with water infiltration.

The evapotranspiration was realized in the simulations with SWAP by adjusting the vegetation parameters. This suggests that in reality the parameters of the unsaturated zone or the evapotranspiration may be different. SWAP and Plaxis use different limits for the water extraction and relative permeability. However, SWAP accounts for transpiration by vegetation, evaporation and other environmental influences. Therefore, it is advised to use this program in studies of the unsaturated zone.

Analysis of effect of the parameters describing the retention curve according to 'van Genuchten' (see above), showed the following. Reduction of the 'van Genuchten' parameter g_n results in a decrease of water propagation. For a reduction of 2 the residual water content is not reached at the top of the profile. This means that water is available at the top for evaporation. If the 'van Genuchten' parameter g_i decreases the propagation of the water pulse increases. The 'van Genuchten' parameter g_a has the least influence on the propagation of the water pulse when increasing the parameter with a factor 2 and 3. Finally the residual saturation S_r not only increases the minimum water content but also increases the maximum water content of the downwards propagating with consequently increases the relative permeability and thus the water pulse propagation.

Coupled analyses

For the modelling of the unsaturated zone behaviour a Mesh with element sizes of 0.20 m is necessary. However, for the BRM with a width of 850 m and a height of 350 m it is not possible to apply such fine mesh in Plaxis at this stage of development. The average element height (EH) for the BRM is 9 m, where 0.20 m would be required and the number of elements is about $5E3$. Applying a mesh with EH 0.20 m increases the number of elements to about $1E7$ and the number of nodes to about $1.5E8$. It is not feasible with the currently available computing power at the Geo-Engineering section to run the scenarios. A solution may be to enable Plaxis to run on a supercomputer or make parallel processing possible.

For the conditions of steady state calculation with suction the BRM is stable with a safety factor of 1.17. The safety factor of the BRM decreases slightly with increasing head on the hill side of the geometry. Suction in the unsaturated zone increases the safety factor by only 0.01. This suction decreases when water infiltrates. The small influence of increasing groundwater table corresponds with inclinometer readings.

Since this study of the flow through the unsaturated zone showed that rainwater does not reach the groundwater level, the infiltrated water only influences the suction of the unsaturated zone. Reduction of suction results in a decrease of strength thereby lowering the stability of the slope.

The increase of the groundwater level is ascribed to an increase of the x-flow an inflow of groundwater from outside the investigated region. Investigation of the origin of this flow is strongly advised.

In order to limit the influence of rainwater on the properties of unsaturated zone, the infiltration of water into this zone should be reduced. As a remedial measures to reduce rainwater infiltrating the BRM, application a graded (high permeable soil on top of impermeable soil) top layer and increasing transpiration is advised.

8.2. Recommendations

The recommendations for further studies are divided in recommendations for further studies on slow moving landslides in general and studies on the BRM in particular.

Slow moving slides

Direct coupling of the groundwater changes and corresponding pressure distribution with calculations of the deformation is of essence for slow moving slides. Performing analyses with Plaxis on a smaller slow moving slide where the mesh requirements can be met is therefore advised.

A more detailed analysis of the soil profile is achieved with SWAP owing to the agricultural features that are included. Combining the capabilities of SWAP with those of Plaxis will be beneficial for the evaluation of slow moving slides. This possibility should be further explored.

The reduction of rainwater infiltration by transpiration can be enhanced. Research on the effects of this remedial measure is proposed.

BRM

The accuracy of the analysis of the BRM can be improved, if the strength of the soil, the hydraulic conductivity and the properties of the unsaturated zone are determined experimentally. To this end, also laboratory tests ought to be performed. Experimental data on time histories of the distributions of pore water pressure and suction in the unsaturated zone is lacking. These data can be obtained with tension meters.

The water balance is vital for understanding of the changes in groundwater conditions. The origin of the unknown factor in the water balance, namely the x-flow, should be further investigated. Probably for a realistic analysis of groundwater flow a larger geohydrologic geometrical model may be needed including the natural boundaries of groundwater shedding.

In this study the large main slide was evaluated, but there are various sub slides present. Analysis of these sub slides, with the same approach as used for the main slide, is recommended.

The BRM is located in a area which is prone to earthquakes. Therefore, future analysis on the stability of the BRM should include the effects of quakes.

Acknowledgements

I wish to thank my supervisors professor Frans Molenkamp, professor Michael Hicks and dr. ir. Ronald Brinkgreve for their stimulating discussions and excellent guidance of the MSc. thesis project. Dr. ir. N. Kringos for critical reading of the thesis and valuable suggestions.

I am grateful to dr. ir. Vahid Galavi from Plaxis who helped me with the computational work and for sharing his breath of knowledge with me. I also owe thanks to ir. Ed Hartman for this efforts to make the Plaxis version operational for me.

I am indebted to dr. ir. Jos van Dam from the University of Wageningen (The Netherlands) for his valuable suggestions and introduction into the program SWAP.

Special thanks goes to Lauren Doyel (PE) from Fugro West Inc., Malibu, California (USA), who introduced me into the secrets of the Big Rock Mesa landslide during my internship. Her help to provide me with invaluable data for this thesis project is much appreciated.

Finally, I would like to thank my friends and family for their support and keeping faith in me.

References

Articles

- E.E. Alonso, A. Gens, A. Josa, 1990, A constitutive model for partially saturated soils, *Geotechnique* 40, Nr. 3, pages 405-430.
- Th.W.J. van Asch, L.P.H. Van Beek, T.A. Bogaard, 2007. Problems in predicting the mobility of slow-moving landslides. *Engineering Geology*, Nr. 91, pages 46-55.
- N.S. Aulakh, 2008. Landslide Monitoring, A fiber optic interrogator based on optical time-domain reflectometry predicts and prevents geological hazards, *Photonics spectra*, 2008, Vol. 42, Nr. 8, pages 64-66.
- A.W. Bishop, G.E. Blight, 1963, Some aspects of effective stress in saturated and partly saturated soils, *Geotechnique*, Nr. 3, pages 177-197.
- G.E. Blight, 1961, Strength and consolidation characteristics of compacted soils, Ph.D. dissertation, Univ. of London, London, England.
- G.E. Blight, 1980, The mechanics of unsaturated soils, notes for a series of lectures delivered as part of Course 270C at Univ. of California, Berkeley, USA.
- T.A. Bogaard, T.W.J. Van Asch, 2002. The role of the soil moisture balance in the unsaturated zone on movement and stability of the Beline landslide, France. *Earth surface process landforms*, Nr 27, pages 1177-1188.
- G. Bolzon, B.A. Schrefler, O.C. Zienkiewics, 1996, Elasto-plastic soil constitutive laws generalised to partially saturated states, *Geotechnique* 46, Nr. 2, 279-289.
- D. Fabre, J. Gustkiewicz, 1997, Technical note. Poroelastic properties of limestones and sandstones under hydrostatic conditions. *Int. J. Rock Mech. Min. Sci.* 34, No. 1, pages 127-134.
- V. Galavi, 2009, *Plaxis Manual*, Groundwater flow and fully coupled flow deformation analyses in Plaxis 2D, Delft, The Netherlands.
- V. Galavi, R.B.J. Brinkgreve, P.G. Bonnier, N.A. Gonzalez, 2009, Fully coupled hydro-mechanical analysis of unsaturated soils, *Proceedings ComGeo 2009*, pages 486-495
- MTh. Van Genuchten, 1980. A closed-form equation for predicting the hydraulic conductivity of unsaturated soil, *Soil Science Society America Journal*, Nr. 44, pages 129-147.
- E. Hoek, P. Marinos, 2006 A brief history of the development of the Hoek-Brown failure criterion, *Roclab*.
- E. Hoek, C. Carranza-Torres, B. Corkum, 2002, Hoek-Brown failure criterion, *Roclab*.
- J. Krahn, D.G. Fredlund, 1972, On total matric and osmotic suction, *J. Soil Sci.*, Vol. 114, Nr. 5, pages 339-348.
- C. Lissak, O. Maquaire, J.P. Malet, 2009. Role of hydrological process in landslide occurrence: Villerville-Cricqueboeuf landslides (Normandy coast, France), *Conference Landslide Processes: from geomorphologic mapping to dynamic modelling*, Strasbourg, pages 175-180.
- F. Molenkamp, A.H. Nazemi, 2003. Interactions between two rough spheres, water bridge and water vapour, *Geotechnique* 53, Nr. 2, pages 255-264.

Y. Mualem, 1976, A new model for predicting the hydraulic conductivity of unsaturated porous media, Water Resource, Nr 12, pages 513-522.

B.G. Richards, 1966, The significance of moisture flow and equilibria in unsaturated soils in relation to the design of engineering structures built on shallow foundations in Australia, presented at the symposium: Permeability and capillary, Amer. Soc. Testing materials, Atlantic City, NJ, USA.

M.R. da Silva, C. Schroeder, J.C. Verbrugge, 2008, Unsaturated rock mechanics applied to a low-porosity shale, Engineering Geology Nr. 97, pages 42-52.

A. Thielen, S.M. Springman, 2008, Predicting the variation of stability with time for a slope in Switzerland, First European Conference On Unsaturated Soils 2008 (E-UNSAT), pages 941-946.

S.J. Wheeler, R.J. Sharma, M.S.R. Buisson, 2003, Coupling of hydraulic hysteresis and stress-strain behaviour in unsaturated soils, Geotechnique 53, Nr. 1, pages 41-54.

B.C. Yen, 1969. Stability of slopes undergoing creep deformation. Journal of Soil Mechanics and Foundation Engineering, Vol. 95, Nr. SM 4, pages 1075-1096.

Books

- J. Atkinson, 1993, The mechanics of soils and foundations, Taylor & Francis group, Oxon, UK
- R. Chowdhury, P. Flentje, G. Bhattacharya, 2010, Geotechnical slope analysis, CRC Press, Taylor & Francis group, London, UK.
- D.H. Cornforth, 2005. Landslides in practise remedial/preventative options in soils, John Wiley & sons, inc.. Hoboken, New Jersey, USA.
- D.G. Fredlund, H. Rahardjo, 1993, Soil mechanics for unsaturated soil, John Wiley & Sons, INC., New York, USA.
- C.R. Fitts, 2002, Groundwater Science, Academic Press, London, UK.
- R.E. Goodman, 1989, Introduction to Rock Mechanics, second edition, John Wiley & Sons, New York, USA.
- G.L. Guymon, 1994. Unsaturated zone hydrology, PTR Prentice Hall Englewood Cliffs, New Jersey, USA.
- W.K. Hamblin, E.H. Christiansen, 2001, Earth's dynamic systems tenth edition, Pearson Education. Inc., Upper Saddle River, New Jersey, USA.
- F. Molenkamp, 2008-2009, Reader continuum mechanics, CT 4353, TU Delft, Delft, The Netherlands.
- D. Muir Wood, 1990, Soil behaviour and critical state soil mechanics, Cambridge University Press, Cambridge, UK.
- D. Muir Wood, 2004, Geotechnical Modelling, Spon Press, Oxfordshire, UK.
- J.D. Nieuwenhuis, 1991. The lifetime of a landslide, A.A. Balkema, Rotterdam, The Netherlands.
- K. Sassa, H. Fukuoka, F. Wang, G. Wang, 2005, Landslides risk analysis and sustainable disaster management, Springer, Berlin Heidelberg, Germany.
- C.W.M. Sitters, 2006, Material models for soil and rock, Reader CT4360, TU Delft, Delft, The Netherlands.

Reports

- Annual report July 2003 through June 2004, Big Rock Mesa Landslide assessment district, Malibu, California, July 2004, repaired by Fugro West Inc. for the City of Malibu, California, USA.
- Annual report July 2004 through June 2005, Big Rock Mesa Landslide assessment district, Malibu, California, July 2005, repaired by Fugro West Inc. for the City of Malibu, California, USA.
- Annual report July 2005 through June 2006, Big Rock Mesa Landslide assessment district, Malibu, California, July 2006, repaired by Fugro West Inc. for the City of Malibu, California, USA.
- Annual report July 2006 through June 2007, Big Rock Mesa Landslide assessment district, Malibu, California, July 2007, repaired by Fugro West Inc. for the City of Malibu, California, USA.
- Golden Software, Surfer, manual.
- Plaxis manual, 2D Plaxis 9, Delft, The Netherlands.

SWAP, Manual Version 3.2. Theory description and user manual, J.G. Kroes, J.C. Van Dam, P. Groenendijk, R.F.A. Hendriks, C.M.J. Jacobs, 2008, Wageningen, The Netherlands.

Websites

<http://www.ipm.ucdavis.edu/calludt.cgi/WXDESCRIPTION?STN=STMONICA.A>.

<http://www.ci.malibu.ca.us/download/index.cfm/fuseaction/download/cid/4650/>

http://www.cccarto.com/cal_wildfire/oldtopanga/fire.html

http://www.malibucomplete.com/mc_hazards_fires.php

www.roclab.com

<http://www.finesoftware.eu/geotechnical-software/help/fem/modified-cam-clay-model-mcc/>

http://www.rocscience.com/downloads/phase2/WebHelp/pdf_files/theory/CamClay.pdf

<http://landslides-gib.blogspot.com/2009/02/landslide-monitoring-by-optical-fiber.html>

[\(http://www.thetech.org/exhibits_events/online/quakes/seismo/](http://www.thetech.org/exhibits_events/online/quakes/seismo/)